UNIVERSITY OF OKLAHOMA

GRADUATE COLLEGE

KINEMATICS, THERMODYNAMICS, AND MICROPHYSICS OF THE 25-26 JUNE 2015 KANSAS MCS DURING PECAN

A THESIS

SUBMITTED TO THE GRADUATE FACULTY

in partial fulfillment of the requirements for the

Degree of

MASTER OF SCIENCE IN METEOROLOGY

By

RACHEL LEIGH MILLER
Norman, Oklahoma
2018

KINEMATICS, THERMODYNAMICS, AND MICROPHYSICS OF THE 25-26 JUNE 2015 KANSAS MCS DURING PECAN

A THESIS APPROVED FOR THE
SCHOOL OF METEOROLOGY

BY

_____
Dr. Conrad Ziegler, Chair

_____
Dr. Michael Biggerstaff

_____
Dr. David Parsons

This thesis is dedicated to my Mommom, Shirley Jean Shanholtz. For Christmas 2000, she gave me my first weather book and instilled in me a life-long love of weather and science.

Acknowledgements

I would first like to thank my advisor, Conrad Ziegler, for giving me the opportunity to participate on the PECAN field campaign and conduct research on the data collected, and for all of his support and guidance throughout this process. I would also like to thank my committee members, Michael Biggerstaff and David Parsons, for their input and support.

This thesis work would not have been possible without the PECAN forecasters who provided excellent forecasts on the timing and placement of nocturnal convection, the PIs who coordinated successful missions during PECAN, and the mobile crews who stayed up into the late hours of the night collecting data.

I would like to thank my parents, Michael and Jill Miller, and my brothers, Joshua and Seth Miller for their continued support and encouragement. I would also like to thank Addison Alford for his emotional support and encouragement, and for all of his help installing and running Py-ART. Finally, I would like to thank all of my amazing friends, in particular Elizabeth DiGangi, for their encouragement.

This research was funded by NSF grant AGS-1359726.

Table of Contents

List of Tables

List of Figures

Abstract

This case study analyzes a nocturnal mesoscale convective system (MCS) that was observed in northeast Kansas as part of the Plains Elevated Convection at Night (PECAN) field experiment on 25-26 June 2015. Over the course of the observational period, a broken line of nocturnal convective cells initiated around 0230 UTC on the cool side of a stationary front and subsequently merged into a quasi-linear MCS that later matured and developed strong outflow and a trailing stratiform region. This study combines radar observations with mobile and fixed mesonet and sounding data taken during PECAN to analyze the dynamics, thermodynamics, and microphysics of the MCS from 0300 to 0630 UTC. This study is unique in that 38 consecutive multi-Doppler wind analyses were studied over the 3 and a half hour observation period allowing for a long-lived analysis of the evolution of the kinematics and microphysics of the nocturnal MCS.

Radar analyses indicated that the initial convective cells and linear MCS were elevated which is supported by the Hiawatha mesonet site which showed gradual cooling due to precipitation evaporation. During upscale growth, individual convective cells developed storm scale surface-based cold pools which were measured by MM1. By 0500 UTC, the linear MCS was surface-based and a bowing MCS developed which produced a wind report 20 minutes later. The mobile and Kansas mesonet sites recorded a large temperature drop when the convective lines passed over and a similar final theta-v value indicating the homogeneity of the cold pool over time.

Trajectory analysis using diabatic Lagrangian analysis confirms the conclusions from the observations showing that parcels from below 500 m were being ingested in

the convective line updrafts of the MCS indicating that the system was at least partially surface-based. The transition from elevated to surface based was due to the formation of a surface-based cold pool that was driven by diabatic cooling due to graupel melting and rain evaporation. In this environment, the elevated system became surface-based when the cold pool lifting was sufficient for surface-based parcels to overcome the CIN associated with the frontal inversion.

Chapter 1: Introduction

The Plains Elevated Convection at Night (PECAN) field program was designed to study nocturnal weather features, including mesoscale convective systems (MCSs), bores, convection initiation events, and the low level jet (LLJ). The comprehensive PECAN observing strategy included profiles from the AERI and Doppler wind lidars, as well as aircraft measurements and both mobile and fixed observations obtained by radars, sounding systems, PECAN integrated sounding array (PISA) systems, research aircraft, and mesonets (Geerts 2013). Nocturnal MCSs contribute to the well-established nocturnal precipitation maximum over the central United States during the summer months (Maddox 1980; Carbone and Tuttle 2008; Wallace 1975). Despite progress with observations and modeling of MCSs (as documented in the following discussion), the forecasting of nocturnal MCS formation, evolution and intensity continues to present a considerable challenge for forecasters (e.g., Ziegler 1999).

Many of the ideas contributing to the conceptual model of MCSs come from observational studies conducted on daytime storms. Smull and Houze (1985) utilized single Doppler analysis to observe a squall line's development from isolated rain showers to a convective line with an extensive stratiform region. They also observed that the front to rear (FTR) flow was driven by convection in the line and that rear to front (RTF) flow was associated with a reflectivity notch. This study was followed by a Dual-Doppler analysis on the same squall line which found that the FTR flow was not only strengthened in the convective line but extended back to the rear of the system which allowed it to transfer ice particles formed in the convective line to the stratiform rain region. Also noted were convective downdrafts contributing to the gust front and a

mesoscale updraft on top of a mesoscale downdraft in the stratiform and transition region (Smull and Houze 1987a). Rutledge and Houze (1987) followed with a modeling study which confirmed the previous study's theory that the most intense stratiform rain region formed due to hydrometeors advected in the FTR flow which then grew due to the persistent mesoscale updraft. Further observational studies such as Watson et al. (1988) have also given evidence for this mechanism. A single Doppler analysis of the 10-11 June 1985 MCS detailed observations of the FTR flow, mesoscale updraft and downdraft, as well as the rear inflow jet (RIJ) which was just below the mesoscale updraft and downdraft interface. This study attributed the cause of diabatic cooling to sublimation and evaporation which drove the mesoscale downdraft (Rutledge et al. 1988). Dual-Doppler analyses of this storm at its mature stage showed that the mesoscale updraft covered most of the area in the stratiform rain region while the mesoscale downdraft was associated with the most intense rainfall (Biggerstaff and Houze 1991). A classical conceptual model of a leading line, trailing stratiform (LL/TS) MCS developed by Houze et al. (1989) illustrates the various airflow branches based on previous observational studies of MCSs (Figure 1).

One of the important components of a MCS is the RTF flow or RIJ mentioned previously. Smull and Houze (1987b) hypothesized that the rear inflow was due to a rearward sloping negative perturbation pressure located behind the main convective updrafts which drew air in behind the line and then accelerated it downward. Another possible mechanism suggested was a midlevel low in the stratiform region formed by latent heating aloft and evaporative cooling below creating a horizontal pressure gradient force that would draw in air in the mid-levels. These two mechanisms could

work together to create steady rear inflow. Another observational study noticed that the rear inflow formed before there was a stratiform rain region implying that its development was convectively driven. The RIJ also became more sharply tilted after interacting with the convective line (Rutledge et al. 1988). In another observational case, Klimowski (1994) saw that the rear inflow began near the high-reflectivity cores in the line and that as the line matured, it intensified and expanded rearward. The rear inflow was also initially elevated and descended downward towards the surface in the areas where the line was more intense. Finally, a positive correlation between the strength of the FTR and RTF flow was observed and further supported by the strongest rear inflow being located behind the most intense convective regions. Grim et al. (2009) also observed that the descent of the RIJ was associated with the intensification of the convection in the line. Overall, the RIJ strengthened when the convective updrafts strengthened and weakened as the bow weakened. An intensification of the RIJ has also been shown to intensify the wake low and high (Nachamkin et al. 1994).

Although rear inflow is correlated to the strengthening of the FTR flow in an MCS, cold pools and their dynamics are also very influential on system development. Cold pools are defined as areas of downdraft air that have been diabatically cooled by rain evaporation and ice melting, subsequently spreading out horizontally beneath precipitating clouds (Engerer et al. 2008). Trier et al. (2011) found that latent cooling was responsible for the downdrafts in their simulation of a nocturnal MCS. Other studies have emphasized the importance of dry air at mid-levels because these elevated dry layers lead to elevated layers of strong negative buoyancy which can allow downdrafts to reach the surface to form a cold pool (Bryan et al. 2005; Corfidi 2003).

Bryan and Weisman (2006) noted that elevated near-neutral layers could also help produce deep cold pools. Davis et al. (2004) found that the cold pool strength was dependent on the RIJ and stratiform microphysics. Davis et al. (2004) suggested that while elevated layers were important for establishing the cold pool, the formation of stratiform precipitation and rear inflow was important for strengthening the cold pool.

Cold pools have been hypothesized to sustain squall lines by lifting air along the leading edge of the gust front, as supported by the MCS simulations of Billings and Parker (2012). Rotunno et al. (1988) theorized based on modeling studies that the key to long-lived squall lines was a balance between low-level shear and cold pool propagation so that updrafts would be upright and in their optimal state. However in their simulations, cold pools were generally 2-3 km deep whereas many observational studies have found cold pools as deep or deeper than 4 km (Roux 1988; Bryan et al. 2005; Bryan and Parker 2010). The mesoscale pressure gradient of cold pools can cause severe winds without downdrafts (Bryan and Weisman 2006). Hence, mesoscale nocturnal MCS cold pools are important both for squall line propagation and also for the generation of damaging, severe straight-line winds which is important for forecasters.

One of the main objectives of PECAN was to determine whether nocturnal MCSs are elevated or surface-based and how these systems sustain themselves after sunset (Geerts 2013). Corfidi et al. (2008) defined elevated convection as convection that draws in air from a layer above the planetary boundary layer (PBL). Due to the fact that radiative cooling at the surface typically produces a nocturnal stable layer, it has previously been hypothesized that nocturnal convection is typically elevated. For

example, it has been assumed that a MCS that develops on the north side of a cold front is elevated and therefore decoupled from the surface (Gale et al. 2002). Other studies showed that systems on the north side of a front may be sustained by the LLJ instead of surface based instability, implying that elevated instability sustains these systems (Trier and Parsons 1993). Via a dual-Doppler analysis of a nocturnal squall line in West Africa, Roux (1988) noted the existence of a substantial layer of weakly or negatively buoyant air at low levels, which in turn would imply that an external process was necessary to lift air to its level of free convection (LFC). Grim et al. (2009) also noted the existence of a very stable layer in the lowest 60 hPa in the environment where a nocturnal bowing MCS develops. Another nocturnal MCS study by Carbone et al. (1990) showed that elevated convection initiated along areas of PBL convergence. Due to the stability in the nocturnal boundary layer, Carbone et al. (1990) hypothesized that these systems would propagate via gravity currents, undular bores, turbulent bores, and solitary waves. The latter elevated convective systems did not rely on RTF flow to sustain the MCS. Schmidt and Cotton (1990) also noted how important wave dynamics are to the maintenance of nocturnal MCSs. For illustration, Schmidt and Cotton (1990) analyzed a case where a high amplitude internal gravity wave developed in the nocturnal stable layer and became the driver of an MCS. Schmidt and Cotton (1990) further argued that their analyzed MCS propagated at the same speed as the gravity wave, thereby providing an important forcing mechanism to lift low-level inflow air into the convective line. It has also been shown that elevated shear is important to nocturnal systems because it allows the MCS to maintain convection along the cold pool (Coniglio et al. 2010). More recently, some studies have suggested that while

nocturnal storms have conventionally been assumed to be elevated, they may in fact be at least partially surface-based.

Corfidi et al. (2008) argued against classifying systems as either purely surface-based or purely elevated, and instead hypothesized that a continuum of storm inflow modes exists between the surface-based and elevated storm types. Corfidi et al. (2008) also found that convective systems may become more or less elevated due to changes in the environment and emphasized the importance of realizing that there is no distinct line between surface based and elevated storms. Parker (2008) used a simple model with homogenous horizontal initial conditions to simulate how a surface-based MCS would respond to low level cooling similar to the cooling of either the nocturnal stable layer or crossing a front or boundary. In the simulations it was noted that even with 10 K of low-level cooling, the squall line's cold pool was still able to lift boundary layer parcels to their LFC despite larger values of convective inhibition (CIN). The systems did eventually become elevated with additional cooling, but the convective available potential energy (CAPE) of the boundary layer parcels went to zero before the transition to elevated convection occurred. Once the system became elevated, it propagated due to a bore on top of the stable layer. The two main things that sustained an MCS in an environment with low-level cooling were CAPE and a dome in the isentropes which was due to either a cold pool or a bore on top of the stable layer. This work suggested that systems assumed to be elevated since they occurred in an environment with a nocturnal stable layer may in fact have been surface based.

Billings and Parker (2012) employed observations and simulations to study nocturnal convection during BAMEX. In their study, both supercells and a squall line

developed in the evening hours and persisted through the night. These simulations showed that even with a stable nocturnal layer, the squall line and supercells were able to remain surface-based through two different mechanisms: the squall line was sustained by deep cold pool lifting and the supercells were sustained by an enhanced vertical perturbation pressure gradient acceleration. Billings and Parker (2012) recommended that forecasters be aware that many nocturnal convective events are not entirely elevated. Schumacher (2015) performed multiple experiments with a simulated MCS by varying moisture in the near-surface stable layer. Even though the near-surface layer parcels had large values of CIN, Schumacher found that the near-surface air parcels were still contributing to convective updrafts and thus changes in the low level moisture did impact the overall MCS evolution. Air within the stable layer was important as long as it had sufficient CAPE to support updrafts regardless of the CIN. Schumacher also suggested that systems previously thought to be elevated were in fact drawing in air from the near-surface layer. Marsham et al. (2011) documented the first case study of elevated convection transitioning to surface-based convection. The system studied by Marsham et al. (2011) began as elevated convective cells that initiated in an area of enhanced elevated convergence near the terminus of the LLJ. As the convective cells organized into a line, the system was subsequently able to establish a surface based cold pool that efficiently lifted parcels from the nocturnal stable layer. An increase in reflectivity appeared to be associated with the transition from elevated to surface-based. The study by Marsham et al. (2011) argued for more case studies on nocturnal convection to determine whether the transition from elevated to surface-based is more generally important in the longevity of long-lived nocturnal MCSs.

The following case study of the 25-26 June 2015 MCS will analyze whether the system is elevated, surface-based, or some combination of these two modes. This study of the 25-26 June nocturnal MCS combines radar observations of the MCS with mobile and fixed mesonet and sounding observations taken during PECAN. A diabatic Lagrangian analysis (DLA) integrates the time-dependent 3-D wind syntheses with selected soundings, thereby facilitating retrieval of the thermodynamical and microphysical MCS structure and the derivation of several dominant sources of diabatic heating and cooling that act to drive the updraft, downdrafts, and maintain the mesoscale cold pool.

Chapter 2: Data and Analysis Methods

a. Mobile and Fixed Ground-based Radars

Six mobile radars collected data for the 25-26 June 2015 MCS. The mobile radars included Smart-R1 (SR1), Smart-R2 (SR2), the NOAA/NSSL X-POL (NOXP), Dow 6, Dow 7, and Dow 8 (Biggerstaff et al. 2005; Wurman et al. 1997). Two of the radars were 5-cm wavelength (C-band) Doppler radars (SR1 and SR2), while the other four Doppler radars were 3-cm wavelength (X-band). All mobile radars were dual-polarimetric with the exception of SR1 and Dow 8. The baselines varied between the radars since the deployment strategy positioned the radars in triangles. The mobile radar array consisted of a large triangle to the north involving SR1, SR2, and NOXP, combined with a smaller triangle to the south involving Dow 6, Dow 7, and Dow 8. The baseline lengths between the various radar pairs were as follows: SR1-SR2 (30 km), SR2-NOXP (27 km), SR1-NOXP (40 km), SR1-DOW7 (37 km), NOXP-DOW7 (41 km), DOW7-DOW8 (21 km), DOW7-DOW6 (21 km), and DOW6-DOW8 (29 km).

SR1 collected volume scans every five minutes from 0300 to 0630 UTC. SR2 collected volume scans every ten minutes from 0300 to 0340 UTC and subsequently every five minutes from 0340 to 0630 UTC. NOXP collected volume scans every ten minutes from 0300 to 0330 UTC and every five minutes from 0330 to 0630 UTC. DOW7 collected volume scans every ten minutes from 0300 to 0440 UTC and every five minutes from 0440 to 0625 UTC. Although DOW6 and DOW8 were scanning prior to 0500 UTC, their volumes were not incorporated into the multi-Doppler analysis before 0500 UTC since the squall line was too far away. DOW8 collected five minute volume scans from 0500 to 0520 UTC, while DOW6 collected five minute volume

scans from 0500 to 0625 UTC. Owing to the different scanning strategies of the radars, the number of mobile radars contributing to an analysis period varied. However, there was a minimum of three mobile radars contributing to each wind synthesis.

Data collected from the National Weather Service (NWS) Topeka WSR-88D radar (KTWX) was also used in the multi-Doppler analyses. The WSR-88Ds are 10-cm wavelength (S-band) Doppler radars and are also dual-polarimetric. The WSR-88D contributed to every five minute interval analysis via time-to-space conversion to match its low level scans to the chosen nominal analysis time.

b. Fixed and Mobile Soundings

The PECAN sounding array consisted of three mobile sounding units, two from the National Severe Storms Laboratory (NSSL) and one from Colorado State University (CSU). These mobile units allowed for soundings to be launched in various locations within the MCS environment. The NSSL sounding units MG1 and MG2 were collocated with DOW7 and were able to provide sequential soundings before, during, and after MCS passage. A total of seven soundings were launched by the MG1-MG2 pair between 0215 and 0701 UTC. The CSU sounding unit MG3 was located farther south and was outside of the mobile radar array and analysis domain. All four mobile PECAN Integrated Sounding Array (PISA) platforms were arranged along a fixed north-south linear array, and launched multiple soundings during the IOP.

c. Mobile Mesonets and Kansas Mesonet

Two NSSL mobile mesonets (MM), the NOXP scout vehicle, and all three mobile sounding units were equipped with rooftop, rack-mounted MM instruments to measure temperature, relative humidity, pressure, and wind direction and speed. All

MM-equipped vehicles also recorded latitude and longitude, enabling both measured and derived variables to be analyzed in space and time (Straka et al. 1996; Ziegler et al. 2004). Although MM instruments obtained measurements at a frequency of 1 Hz, a five minute running average was computed to smooth the time series and enable comparison with the Kansas mesonet observations.

Data from two Kansas mesonet sites, Hiawatha and Manhattan, were located within the mobile radar array and analysis domain, thus contributing to the analysis of in situ measurements. Kansas Mesonet variables such as temperature, relative humidity, and wind speed were archived as a five minute running average in contrast to the 1 Hz MM data rate.

d. Radar Analysis Method

All radar data have been initially dealiased using a customized Py-ART script developed by the Biggerstaff research group at the University of Oklahoma (OU) School of Meteorology (Daniel Betten and A. Addison Alford, personal communication, 2017). The customized OU Py-ART radar editing script employs a region-based method to identify the zero isodop and unfold the velocities to lower the standard deviation of radial velocity within that objectively identified region. The same script also corrects dual-PRF processor errors in a similar region-based method to lower the standard deviation of radial velocity (A. Addison Alford, personal communication, 2017). A statistical clutter detection method developed by Curtis Alexander (Curtis Alexander, personal communication, 2017) has been used to identify and remove potential clutter targets based on user-selected input criteria via the creation of a clutter map based on the identified clutter criteria. This clutter map is then applied to the data

to remove velocity and reflectivity at suspected clutter points. All radar observations have undergone further manual editing using Soloii to eradicate second trip, areas with low signal to noise ratio, and various other artifacts.

A spatial single-radar analysis based on a 1-pass application of Barnes interpolation (Ziegler 2013b) has been employed to map all single-radar data to the MCS grid. The single-radar fields are interpolated to a 160 x 170 km x 15 km domain located in northeastern Kansas. An over-determined dual-Doppler radar synthesis algorithm is then applied with gridded, single-radar analyses from up to six mobile radars and KTWX (Ray et al. 1980; Kessinger et al. 1987; Ziegler 2013b), followed by application of a variational integral constraint to simultaneously impose anelastic mass continuity and kinematic lower and upper boundary conditions (Ray et al. 1980; Ziegler et al. 1983). Additional smoothing is subsequently applied to eliminate any rare, poorly resolved localized velocities. Specific prescribed dual- and triple-Doppler pairs are excluded from the analysis if any such pair is judged to have a bad geometry in an a priori sense (e.g., three radars in a straight line, or two radars with either too large or too small of a baseline). The exclusion of radar combinations having bad geometry ensures that the radars contributing to a wind vector at any given point have an optimal geometry, thereby excluding any potentially biased radial velocity values from the over-determined analysis.

It is noteworthy that this is the first study to utilize up to seven radars in a radar synthesis to analyze MCS kinematics, microphysics, and dynamics. Previous studies have employed mainly dual-Doppler analyses to analyze MCS structure (Bernstein and Johnson 1994; Biggerstaff and Houze 1991, 1993; Carbone et al. 1990; Klimowski

1994; Lin et al. 1992; McAnelly et al. 1997; Nachamkin et al. 1994, 2000; Rasmussen and Rutledge 1993; Roux 1988; Scott and Rutledge 1995; Smull and Augustine 1993; Smull and Houze 1987a; Wang and Carey 2005; Wang et al. 1990). A few studies have employed either triple-Doppler analyses (Grady and Verlinde 1997) or quad-Doppler analyses (Kessinger et al. 1987; Schmidt and Cotton 1989). Other studies have used airborne radar for radar analyses of MCSs. The main disadvantages of airborne radar analysis are somewhat degraded detection of storm structure in the lowest several hundreds of meters above ground, combined with slightly coarser time resolution between successive radar volumes relative to ground-based radar analyses (Davis et al. 2004; Grim et al. 2009; Hildebrand et al. 1996; Jorgensen et al. 1997; Jorgensen and Smull 1993; Lewis et al. 1998; Protat and Lemaitre 2001; Schuur and Rutledge 2000; Storm et al. 2007; Wakimoto et al. 2006a,b; Yu et al. 1999). Another unique aspect of the present study compared to previous studies is that the present radar analysis documents MCS structure every ten minutes from 0300 to 0340 UTC and every five minutes from 0340 to 0630 UTC. Details of the number and names of radars contributing to a particular analysis time are located in Table 1. Accordingly, the present study features an unprecedented three and one-half hours of continuous wind field analyses extending from the initiation through the developing to mature stages of the 25-26 June 2015 MCS.

e. Sounding Analysis

The first sounding analysis step is to vertically smooth each input sounding. The purpose of the initial smoothing of the soundings is to help ensure that incompatible spatial finescale stratifications are not extrapolated horizontally in the

subsequent two-dimensional analysis via horizontal interpolation. Each sounding's 1 Hz (~ 5 m vertical data spacing) horizontal wind components are hole-filled via piecewise linear interpolation, then smoothed with a 15-pass application of a two-sided triangular filter function with a half-width of 150 m. The next step is to horizontally interpolate the smoothed soundings to the grid via weighted averaging employing a one-pass application of the Barnes weighting function of the form

$$w = exp[-(x - x_s)^2/\kappa],$$

where w is a datum weight, x is the grid x-coordinate (km), x_s is the sounding datum x-coordinate (km), and the Barnes smoothing parameter κ is defined as

$$\kappa = (1.3333 \times D_h)^2.$$

Here D_h is the smoothing length scale (km). The final step is to calculate vertical velocity using Boussinesq mass continuity with vertical velocity equal to zero as the upper and lower kinematic boundary conditions via a simple O'Brien variational adjustment (O'Brien 1970). Both the vertical prefiltering and the Barnes weighting function should smooth out most features, so that the resulting analyses reflect the mesoscale environment without any poorly resolved or otherwise aliased finescale structure. The grid spacing is 1 km in the horizontal and 0.1 km in the vertical. The horizontal wind vectors are the objectively analyzed horizontal wind component in the plane from the soundings. The horizontal wind component normal to the vertical cross-section is also objectively analyzed.

Two types of sounding analyses are performed based on the location and timing of the balloon launches. For the first analysis ("Y-Z"), four serially released soundings are launched at 0300 UTC in a south-to-north oriented cross-section, which samples the

environment ahead of the MCS including the stationary front to the south. For the second analysis ("H-Z"), seven soundings from the colocated MG1-MG2 sounding vehicles are used to construct an analysis of the mesoscale features of the MCS and its inflow environment as it passes over the fixed sounding location. Here the smoothing length scale D_h = 10 km for the H-Z analysis, while D_h = 30 km for the Y-Z analysis. The resulting values of the Barnes smoothing parameter κ are about 178 km^2 for the H-Z analysis and about 1600.0 km^2 for the Y-Z analysis. An assumed MCS speed of 5 m s^{-1} has been used to convert the time axis to a distance axis similar to the approach of Bryan and Parker (2010). The present Y-Z analysis also assumes a rotated coordinate system of -55° from east, so that the analysis is perpendicular to the convective line orientation and the system motion.

f. Diabatic Lagrangian Analysis

Diabatic Lagrangian Analysis (DLA) is a kinematic thermal-microphysical continuity retrieval of heat and water substance based on integration along Lagrangian trajectories that proceeds from a series of input time-varying 3-D wind-reflectivity analyses (Ziegler 2013a,b). The present DLA method represents a new generation of storm retrieval that builds upon an earlier thermal-microphysical continuity retrieval method based on solution of a parabolic system of conservation equations for heat and water substance (e.g., Ziegler 1985; Ziegler 1988). Output fields include predicted potential temperature, water vapor mixing ratio, cloud water, and cloud ice, as well as derived temperature, virtual potential temperature, and other variables. Diagnosed output fields include the mixing ratios of rain, graupel/hail, and snow.

A DLA grid domain is nested within the portion of the radar analysis domain containing the best overall multi-Doppler radar coverage. Backward 3-D trajectories are then computed with a 20 s time step from all DLA gridpoints into the MCS inflow environment, and all such inflow-environmental Lagrangian point values of pressure, temperature, and relative humidity are initialized from a suitable environmental sounding. Due to the large number of soundings launched during the IOP, there are separate soundings to represent the environments both ahead of and behind the developing MCS. The sounding representing the inflow environment is actually a smoothed composite that combines a MG1 pre-MCS sounding in the surface-based nocturnal boundary layer, a frontally-lifted MG3 inflow sounding in lower-middle levels, and an MG3 stratiform region sounding in upper levels,

Following trajectory initialization, a system of heat and water substance conserving ordinary differential equations is integrated forward in time along each trajectory path. Bulk parameterized microphysical terms expressing incremental changes of heat and cloud water substance provide the increments in each Lagrangian time step. Using airflow and dBZ values, these calculations diagnose snow, graupel/hail, and rain mixing ratios as well as parameterized rates of collection/riming, freezing/melting, and deposition/sublimation at every Lagrangian point along the DLA trajectories. Forward integration along all trajectories back to their gridpoints of origin, combined with a final gathering operation, yields the 3-D analysis fields at a particular analysis time.

Other studies have utilized a DLA-related class of retrieval methods known generally as “kinematic thermal-microphysical continuity retrieval”. These earlier

methods are based on solutions of a parabolic system of partial differential equations for heat and water substance using radar-derived vector wind fields to help evaluate the kinematic models' transport and mixing terms. Although parabolic systems of governing equations require both multi-dimensional initial and time-dependent lateral boundary conditions, the earliest microphysical retrievals examined a class of storm systems whose airflow fields were in approximate steady state (thus removing the requirement of prescribed initial fields). Ziegler (1985, 1988) developed and employed a generalized 3-D microphysical retrieval and applied the steady state approximation to retrieve potential temperature and mixing ratios of water vapor, cloud, and precipitation in strong, long lived supercell and multicell storms. Rutledge and Hobbs (1983, 1984) applied the steady state approximation and radar-derived wind fields in a line-averaged vertical cross-section to retrieve 2-D thermodynamic and hydrometeor mixing ratio fields in both warm and cold-frontal Pacific Northwest rainbands. Ziegler et al. (1991) extended the Ziegler (1985, 1988) studies to add full time dependence to the 3-D microphysical retrievals and also expanded the kinematic model to include storm electrification mechanisms, retrieving the detailed 4-D evolution of a New Mexican mountain thunderstorm as observed with four fixed Doppler radars. There was close agreement in the Ziegler et al. (1991) study between the evolving, retrieved 3-D model-output fields and independent in situ measurements obtained from two storm-penetrating aircraft, thus closely validating the basic time-dependent microphysical retrieval method. The current study employing the DLA is most like the earlier time-dependent, 3-D microphysical retrieval (Ziegler et al. 1991), since the DLA's time-varying input 3-D wind-reflectivity analyses are used to calculate the backward air

trajectories. The main differences of the DLA are twofold: (a) to formally replace the parabolic system with a system of fully predictive ordinary differential equations whose initial conditions are prescribed from inflow soundings in the MCS environment; and (b) to diagnose the precipitation fields from the reflectivity and updraft history along trajectories. By not assuming steady state, the present study can analyze the evolution of hydrometeor mixing ratios and thermodynamics due to the changing kinematics of the system over the multi-hour analysis period. Since both the DLA and the earlier microphysical retrievals are kinematic, they do not require the calculation of non-hydrostatic perturbation pressure forces. However, these microphysical retrievals all neglect the small perturbation pressure contribution to total pressure in calculating thermodynamic and microphysical tendency terms (e.g., Klemp and Wilhelmson 1978; Ziegler 1985). The DLA domain used in this study is 90 km x 90 km by 15 km, with 500 m grid spacing. Although the DLA domain is periodically relocated inside the radar analysis domain to follow the location of the convective line, the DLA gridpoints coincide with radar analysis gridpoints and thus share the fixed radar analysis origin. Given the DLA domain size in the present study, the DLA is implemented via approximately 1.2 million trajectories. The time period from 0400 to 0600 UTC will be the main focus of the DLA portion of this study, since the latter time period captures the MCS's upscale growth, intensification, and maturity and since the convective line is continuously located inside the DLA domain.

Chapter 3: Case Overview

The 25-26 June PECAN deployment (IOP 16) was declared a bore mission due to the forecasted values of nocturnal low level stability and associated favorable Scorer parameter values. The forecasted bore probabilities provided by the PECAN forecast team subsequently verified, with multiple bores propagating across the state of Kansas ahead of nocturnal convection. A 500 mb ridge was located over the central plains, and analysis at 850 mb revealed no evidence of a nocturnal LLJ that could contribute to the forcing for this MCS. Although low level winds were slightly below LLJ strength, it will be shown that meridional transport of warm, moist nocturnal boundary layer air assisted the formation and growth of the studied 25-26 June MCS. The radar array consisted of two triangles oriented in a north-south line rather than the typical hexagonal shape of a MCS mission because the radar array was configured to help support the bore mission. The radar array was also situated just north of an E-W oriented stationary front.

The north side of an E-W oriented stationary front has often been the location of elevated nocturnal convection initiation (CI). Many studies have noted that these fronts are areas of mesoscale confluence usually associated with lifting of the LLJ (Johns and Hirt 1987; Maddox 1980; Trier and Parsons 1993; Wetzel et al. 1983; Gale et al. 2002; Jirak and Cotton 2007; Watson et al. 1988; Zheng et al. 1995). Although the LLJ per se was not acting to enhance confluence on 25-26 June, frontal convergence was nevertheless supportive of lifting the moist southerly flow. Elevated, isolated convective cells began to form at 0230 UTC on the north side of the front to the northwest of the radar array. The reflectivity from KTWX at 0300 UTC overlaid with SAOs and MM

observations shows weak, isolated convective cells in the northwestern corner of the domain which are part of a line of CI. The surface observations show that these cells are initiating on the cool side of the stationary front with surface temperature between 22 and 23° C (Figure 2). The GOES-IR at 0245 UTC with the same overlays as Figure 2 shows cool cloud tops from some of the stronger cells with the majority of the cells to the northwest of the radar domain since the IR image was taken fifteen minutes prior (Figure 3). Only the center of these cells have cloud tops cooler than -50° C, which is much warmer in comparison to the surrounding anvils from other convection. The surface observations reveal northeasterlies in the cooler, more moist environment as characterized by dewpoint depressions of about 2-3 degrees to the north of the stationary front. In contrast, southerlies in a slightly warmer environment are noted to the south of the stationary front.

The dashed vertical line (Figure 2 and Figure 3) locates the south-north oriented Y-Z sounding analysis cross section (Figure 4). One of the main things to note is that south of the stationary front, the lowest levels of the atmosphere are moist (Fig. 4a) and warm (Fig. 4b), but despite weak lifting along the front interface, the highest moisture values are not being lifted over the front. The warm, moist air appears to pool around the edge of the front with mixing ratios over 17 g kg^{-1} staying south of the front (Fig. 4a). However, mixing ratio values from 9 to 15 g kg^{-1} deepen and lift about a half a kilometer in height to the north of the front. Hence, there is more elevated moisture, especially the layer of values between 12 and 13 g kg^{-1}. The field of perturbation theta-v values relative to the MG3 sounding reveals that theta-v' is approximately conserved following the frontal lifting motion (Figure 4b). Most of the changes in theta-e (Fig. 4c)

and theta-w (Fig. 4d) occur in the lowest 2 km, with cooler values below about 1 kilometer north of the front indicating that a low-level stable layer is present. The stable layer is present in most soundings except for MP1, which was the farthest south mobile PISA and much deeper in the warm sector. While the stable layer is stronger to the north of the front, the warm nose cools via lifting as the air advects over the frontal boundary. This process of lifting and cooling leads to an elevated residual layer from about 750 m to almost 2 km. This elevated layer is extremely important in the pre-MCS environment, since it represents air that has cooled while conserving water vapor mixing ratio and thus increases the layer's relative humidity. In summary, weak frontal lifting on the order of 0.1 m s^{-1} allows air from south of the stationary front to go through a conserved lifting process (i.e., "isentropic upglide") which in turn primes the environment for the MCS.

Multi-Doppler data collection of the initial convective cells began at 0300 UTC. Between 0300 and 0400 UTC, these isolated cells merged into a convective line oriented WSW to ENE. In the next hour, rapid upscale growth was observed with the MCS until about 0500 UTC when a bowing MCS segment formed along the farthest southwestern portion of the linear MCS. The linear MCS is evident to the northeast of a sharp bend of the convective line in reflectivity from KTWX at 0500 UTC (Figure 5). The GOES-IR image at 0500 UTC illustrates the coldest temperatures associated with the convective line and the top of the anvil extending behind the line (Figure 6). The linear MCS remains to the north of the stationary front while the bowing MCS straddles the front (Figure 5 and Figure 6). Thus, the convective cells in the linear MCS ingest air from the elevated residual layer, while convection in the southern bowing MCS

segment is drawing air from the surface-based layer in the warm sector to the south of the front. Behind the main line, temperatures are cooler than at 0300 UTC in accord with mesoscale cold pool passage. Both the linear and bowing MCS segments went on to produce severe wind reports in northeast KS and western MO (Figure 7). The first severe wind report at 0521 UTC was located near Topeka, KS, while later reports clustered around Kansas City. Multi-Doppler data collection continued until 0630 UTC when the convective line moved out of range of most of the mobile radars.

Chapter 4: Radar Analysis

a. 0300 UTC

The 0.5 km level of the 0300 UTC radar analysis shows isolated convective cells to the northwest of the radar domain (Figure 8). Wind vectors do not indicate areas of strong convergence or outflow near the surface beneath convective cells that would be expected if the convection was surface-based. Thus, it is hypothesized that these early cells are elevated and drawing in buoyant air from the elevated residual layer. Surface winds are also quite weak, which would be expected in the stable nocturnal boundary layer at 0.5 km. The 5 km level shows weak updrafts (small pockets of 10 m s^{-1}) associated with convective cells with weak downdrafts on the periphery of these cells (Figure 9). While these cells are initially isolated as indicated by the small reflectivity and updraft cores, reflectivity values of up to 30 dBZ between cells suggest that these cells are in the process of merging to form a convective line. A sounding launched from MG1 reveals the strongly stratified environment in which these initial convective cells are developing (Figure 10). The strong inversion around 900 mb contributes about 140 J kg^{-1} of CIN, thus likely restricting air from the surface to 900 mb layer from ascending into the convective cells in the absence of a front or other strong lifting mechanism. Unlike environmental soundings shown in Marsham et al. (2011) which have the inversion beginning at the surface in a stable nocturnal boundary layer, the frontal inversion layer in this study is confined to the 900 mb level indicating that this environment is not characterized by a surface nocturnal inversion layer typical of other cases. Despite large values of CIN in the lowest levels, abundant elevated CAPE is available for parcels lifted above 800 mb. The strongly veering wind profile in the

lowest levels of the atmosphere contributes to large values of storm relative helicity (SRH). The combination of veering winds and the strong stability above the surface is most likely associated with the stationary front just to the south of the sounding location.

b. 0400 UTC

The isolated convective cells have merged into a linear system via upscale growth by 0400 UTC (Figure 11). Southeasterly to southerly inflow is seen in the clear air ahead of the line, with northeasterly outflow evident within the most intense portion of the convective line near SR1 and SR2. This flow pattern leads to enhanced convergence at low levels near the leading edge of the line to provide further lift for convection. Updrafts at 5 km are associated with convective cores within the line and also with the isolated cell in the inflow located above SR1 (Figure 12). The enhanced area of convergence mentioned earlier is now located within larger reflectivity values in the center of the line rather than along the leading edge, indicating that this convergence area slopes rearward with height. In the lower reflectivity values (< 30 dBZ) behind the main convective line, northwesterly RTF flow is evident behind the most intense portion of the line. This is similar to the findings in Klimowski (1994) which found that RTF flow first developed behind convective cores and expanded rearward as the line matured.

A vertical cross section through the convective line (i.e., as indicated by the dashed black line in Figs. 11-12) further supports the hypothesis that the strongest rear inflow is located directly upstream from the highest reflectivity core in the 3-5 km layer (Figure 13). The rear inflow is much weaker towards the rear of the system and is only

noticeable in areas with reflectivity values above 30 dBZ. The rear inflow also does not appear to be penetrating down to the surface layer, likely due to low-level stability. The cross-section shows that the main 15 m s^{-1} updraft core is embedded within a larger region of ascent that feeds inflow to the leading-line cell. These updrafts appear elevated with the lowest portion of the 5 m s^{-1} contour starting around 4 km and the strongest core located up around 10 km.

c. 0430 UTC

The linear MCS segment at 0.5 km at 0430 UTC has intensified since 0400 UTC, with higher reflectivity values (> 60 dBZ) in the convective cores (Figure 14). There is also an area to the east-northeast of NOXP where multiple CI events are occurring in the inflow region of the MCS. Some areas of rear inflow are noticeable at this level behind the main convective line, indicating that the RTF flow has descended towards the surface. The area of convergence along the leading line now extends further along the line than at 0400 UTC. The 5 km analysis shows a large area of westerly RTF flow along the entire length of the convective line in the analysis domain (Figure 15). Even though the line is intensifying, the updraft distribution and reflectivity structure at the 5 km level remains predominantly cellular with only some areas of continuous coverage of 5 m s^{-1} updrafts between SR1 and SR2. These updrafts also appear to be in the inflow area close to the mid-level convergence zone.

The vertical cross section goes through the strongest reflectivity core which is below a 15 m s^{-1} maximum updraft (Figure 16). The inflow feeding these updrafts is a continuous area of ascending FTR flow. This cross-section also highlights one of the CI events in the inflow region of the MCS. While the highest values of reflectivity are

elevated (~7 km), the airflow entering the main updraft appears to be coming from the lowest 2-3 km. This cell is also located just ahead of the convergence between the inflow and outflow located around x = 48 km. This cross-section is the first to show the RTF flow extending all the way down to the surface and rearward into lower reflectivity values. The base of the 5 m s^{-1} updraft contour also ascends with the ascending FTR flow, with the lower level updrafts being closer to the leading edge of the line and the higher level updrafts further rearward. All updraft areas appear to be associated with different cells, with newer cells along the leading edge and older cells ascending in the FTR flow similar to MCS morphology revealed by previous studies.

d. 0500 UTC

The 0500 UTC radar analysis is the first to combine observations from all seven radars. A north-south oriented bowing MCS segment is evident at 0.5 km at the southwestern terminus of the linear MCS (Figure 17). Associated with this bowing MCS is a surge of outflow located about 10 km west of Dow8. This outflow appears to be channeled by an anti-cyclonic circulation to the west and a weaker cyclonic circulation to the east. This feature is evident from 0440 to 0525 UTC and will be analyzed in further detail at 0520 UTC in association with a severe wind report. As a result of the stronger outflow from the maturing system, the convergence along the leading edge of the MCS has been enhanced compared to earlier analyses. Another important feature in this analysis is the convection popping up on the backside of the linear MCS that appears to be fed by southwesterly flow riding over the cold pool and lifting to its LFC in the “bow and arrow” style mechanism described by Keene and

Schumacher (2013). While the convection isn't perpendicular to the convective line like the classic bow and arrow MCS, the lifting mechanism is likely similar.

The 5 km analysis shows a much more extensive region of rear inflow from the west that becomes more northwesterly as it approaches the back of the convective line (Figure 18). This observation agrees well with past studies that have found that as the system matures, the RTF flow strengthens and expands rearward (Grim et al. 2009; Klimowski 1994). Also note that the number of convective echoes associated with the bow and arrow convection has decreased indicating that this convection is much shallower compared to the convective line.

A vertical cross section of the linear MCS shows that the RTF flow has strengthened, descended to the surface, and deepened compared to the last analysis (Figure 19). With this strengthening of RTF flow, we also see that the FTR flow has strengthened and extends back into the beginnings of what will be the stratiform precipitation region. Based on kinematics alone, we can say that the descent of the rear inflow indicates that the linear MCS has a surface based cold pool, and following trajectories from the inflow it appears that air from the lowest kilometer is ascending in the FTR flow. Both of these features would indicate that the MCS is surface based if this study defines surface based as a storm that ingests air from below the nocturnal inversion. However it is important to note that the FTR flow is fed by parcels originating from multiple levels in the atmosphere so it may be best to refer to this MCS as a system ingesting parcels from both surface and elevated layers rather than trying to force the MCS into a surface based or elevated dichotomy. This is similar to the continuum idea presented in Corfidi et al. (2008).

e. Severe Wind Report at 0521 UTC

At 0521 UTC, the Storm Prediction Center (SPC) noted the first severe wind report associated with the June 25-26 Kansas MCS. The location of the severe wind report is plotted as "W" in all 0520 UTC figures. The 0.5 km radar analysis shows the wind report at the southern edge of the outflow surge mentioned in the 0500 UTC analysis (Figure 20). This outflow surge is at the end of the most intense portion of convection associated with the bowing MCS and is visible along the entire leading edge of the bowing segment. The anti-cyclonic circulation to the west seems to be dominant over the cyclonic circulation to the east with much stronger winds and a lower reflectivity hole in the center (reflectivity values drop to 15 dBZ in some spots). Winds in the RTF flow in the bowing MCS shift from westerly to north-northwesterly as they encounter this anti-cyclonic circulation.

At the 5 km level the most noticeable feature associated with the wind report is a 20 m s^{-1} updraft core located just to the west of the wind report (Figure 21). On either side of this updraft, there are weak downdrafts (-5 m s^{-1}). This indicates that this wind report is caused by surging outflow and is not due to a strong downdraft or microburst. A north-south vertical cross section through the wind report shows that the severe wind report is on the southern end of an outflow surge with an associated streak in reflectivity following the flow (Figure 22). This outflow surge is located beneath a large area of extensive updrafts which increase in strength with increases in height. In the EW vertical cross section the strong updrafts are located in a narrow region just to the west of the severe wind report with an area of weak downdrafts to the west of that (Figure 23). This updraft/downdraft paring correlates well with the anti-cyclonic circulation to

the west and cyclonic circulation to the east leading to intense updrafts associated with the cyclonic circulation. This indicates that the wind report is likely associated with a mesovortex embedded in the line due to strong shear which helped accelerate winds at the surface.

f. 0530 UTC

At the 0.5 km level, the MCS has higher reflectivity values than at 0500 UTC with larger areas of greater than 55 dBZ reflectivity in both the linear and bowing segments (Figure 24). The bow and arrow convection on the backside of the line is not only stronger but the number of convective cells has increased to create a large area of continuous convection. A small region of stratiform precipitation has finally begun to develop behind the bowing MCS segment even though this portion of the line was the last to form. It is hypothesized that even in a short amount of time, the bowing MCS lofted more particles rearward so that a stratiform region formed behind it before the linear MCS could develop a stratiform region. Since the bowing MCS is further south, it has a better chance of ingesting inflow from the warm, buoyant airmass south of the stationary boundary. Another contributing factor is likely the convection that popped up on the backside of the linear MCS which may have inhibited a stratiform precipitation region from forming because of forced ascent over the cold pool. A stratiform region is characterized by a mesoscale updraft above the melting layer and mesoscale downdraft below the melting layer, so ascent below the melting level would lead to convective like precipitation instead of stratiform. This illustrates the importance of not conceptualizing this MCS as simply a 2-D slab since it is the 3-D components that impact the structure and formation of the system.

The 5 km level of the system shows much stronger updrafts along both the linear and bowing MCS convective lines and higher reflectivity values aloft (Figure 25). Both of these support the idea that the line is continuing to intensify and is able to lift larger particles such as graupel higher up. The RTF flow is covering a much larger area behind the MCS. The vertical cross section shows stair-stepping updrafts ascending as they go further rearward in the FTR flow with a new cell being fed by air from the lowest levels of the nocturnal boundary layer (Figure 26). An interesting feature is small rotors located between the RTF and FTR flow in areas of higher shear with one rotor located between 30 km and 35 km and another between 10 km and 15 km. These rotors allow air from the RTF flow to ascend into the more elevated updrafts in the FTR flow and are observed in other cross sections not shown.

g. 0600 UTC

The radar analysis at 0600 UTC is one of the last analyses to contain the convective line before it leaves the radar array coverage. The 0.5 km analysis shows strong RTF flow throughout the system including beneath the convective line indicating strong rear inflow feeding the outflow (Figure 27). The stratiform region behind the bowing system has grown in areal extent and reduced the southwesterly flow streaming up behind the back of the MCS. As a result, the area of convection behind the line has weakened and many of the cells have begun to merge. This will eventually form the stratiform region behind the linear MCS.

The 5 km radar analysis shows that the convective line updrafts now are advecting particles with reflectivity values over 60 dBZ to the 5 km level (Figure 28). The updrafts associated with the bowing MCS appear to be stronger and cover more

area than the updrafts in the linear MCS. It also shows that the stratiform region is spreading northward into the area behind the linear MCS with large areas of reflectivity values of 35 dBZ. A vertical cross section through the line shows a strong updraft on the leading edge of the cold pool and a deeper layer of rear inflow descending once it reaches the front of the line (Figure 29). The lowest 5 m s^{-1} contour is at about a kilometer in height and is clearly ingesting air from the lowest couple kilometers including the near surface layer. The areal extent of updraft in the FTR flow has increased with pockets of 15 m s^{-1} updraft at the edge of the cross section. Not only is there a rotor present as mentioned previously, but again it is clear that air from the RTF flow is being ingested by the updrafts, especially in the elevated updrafts behind the main convective line. The rear inflow seems much more uniform in speed and depth throughout the cross section with the exception of the flow near the convective line. The rear inflow descent near the front of the convective line leads to strong convergence at the surface and enhanced lifting.

h. 0625 UTC

The 0625 UTC analysis was the final radar analysis time for the IOP since the linear MCS's convective line was mostly out of the domain and the bowing MCS was out of range (Figure 30). Most of the previous convection on the backside of the line has been replaced with stratiform precipitation with some convection popping up much farther behind the MCS. While the rear inflow to the system seems very weak in the stratiform region, it accelerates once it gets closer to the convective line (in regions with reflectivity values >35 dBZ) highlighting the importance of the convective line in maintaining rear inflow.

One interesting feature is that there are two separate areas of stratiform precipitation instead of one large area which is consistent both at the 0.5 km level and the 5 km level (Figure 31). Despite having two separate regions of stratiform precipitation, the stratiform regions are fairly homogeneous as expected. We also see in the 5 km analysis that the rear inflow begins as westerly behind the bowing MCS, veers northwesterly behind the linear MCS, and accelerates farther northeast along the line. Since the whole convective line is not within the radar domain, the vertical cross section was plotted parallel rather than perpendicular to the convective line (Figure 32). This illustrates an updraft/downdraft alternating pattern within the convective cells of the line which is hypothesized to be the reason that multicellular MCSs prefer to organize the convective cells into "convective fingers". This feature has appeared in other MCSs during PECAN and in most cases they orient themselves parallel to the motion of the line. An updraft/downdraft pattern leads to cell growth within the updraft regions and weaker convection within the downdraft regions. This pattern could be caused by some wave like feature such as a gravity wave triggered by convection.

i. Convective Line and Stratiform Region Analysis

A time series of the convective line between 0500 and 0600 UTC was constructed using the same vertical cross sections previously discussed. One of the first things to note is that the horizontal extent of the main convective line becomes larger at each subsequent time (Figure 35). This is likely due to a more mature MCS having more convective cells in various stages of their life cycle with a stronger FTR flow. Overall, the FTR flow increases in areal coverage and strength with time as do the updrafts supporting the main line. Another main feature is the slope of the RTF flow at

0500 UTC, which slowly increases in depth with increasing distance rearward from the convective line. By 0530 UTC, convective cells are initiating over a slightly steeper leading edge of the outflow boundary, and by 0600 UTC the leading edge is about 2.5 km deep which is sufficient for lifting a surface based parcel to its LFC. While the slope of the leading edge becomes steeper with time, the approximate height of the rear inflow in the rear of the system is about the same throughout the hour period.

Vertical cross sections are also constructed through the stratiform precipitation region from 0530 to 0625 UTC. The top panel shows the small stratiform region behind the bowing MCS with rear inflow descending in height when it encounters reflectivity values higher than 35 dBZ (Figure 34). The main area of weak ascent is closest to the edge of the convective line. By 0600 UTC, the stratiform region has grown in horizontal extent with some weak updrafts located above the melting level. The rear inflow continues to descend as it encounters the stratiform region. In the 0625 UTC analysis, which is a cross section through the linear MCS's stratiform region, the stratiform region has grown much larger with a broad area of reflectivity values greater than 40 dBZ. There is consistent rear inflow from the surface to 6.5 km for the entire length of the stratiform region. The main feature in the last analysis is the broad area of weak ascent located above the melting level, which is indicative of a mature stratiform precipitation region.

j. Time-height Analyses of Radar Quantities

Time-height analysis of maximum reflectivity, maximum W value, updraft volume, and updraft volume flux were computed for the 0300 to 0600 UTC time period (Figure 35). Looking at panel (a), one of the first things to note is the 4 vertical peaks

about 45 minutes apart in reflectivity located around 0330, 0415, 0500, and 0545 UTC which aren't co-located with maxima in updraft speed. Perhaps there's another process in the MCS development that leads to these period peaks in reflectivity. Before 0500 UTC, the largest reflectivity values are generally near the surface with the 55-60 dBZ level reaching up to about 7 km in height. After 0500 UTC, this layer increases in height to 10 km by the end of the period. This lifting of higher reflectivity values is coincident with stronger updraft cores as well as larger values of updraft volume and updraft mass flux.

Panel (b) shows updraft volume (UDVOL) rapidly increasing for the first hour as the MCS develops from isolated convection into a line. After 0400, two small peaks in UDVOL are evident, but at 0440 UTC, the same time that the surging outflow feature appears, UDVOL values of above 1820 km^3 first appear and are maintained for the rest of the time series. The next two peaks occur at 0500, which is when the bowing MCS develops, and at 0530 UTC. Both appear to have a double maximum structure. This double maximum has been previously observed by Jorgensen et al. (1997) with a lower maximum in the cells developing on the leading edge and a second maximum in upper troposphere. In this case, a maximum is located in the mid-levels and upper levels associated with mature cells and ice processes respectively.

Panel (c) shows updraft mass flux (UDMFLX), which similarly to UDVOL, increases rapidly for the first hour as the cells congeal into a line. UDMFLX has similar trends to UDVOL except the double maximum structure is not evident in UDMFLX. UDMFLX instead indicates that the mid-level updrafts are stronger than the upper level since UDMFLX is weighted for the W value. Along with peaks in the same location,

both UDVOL and UDMFLX show a slight decrease around the time of the severe wind report. Perhaps the updrafts temporarily weaken while surface base outflow increases in strength. The final thing to note is that the MCS was moving out of the domain towards the end of this time period so decreases in UDVOL and UDMFLX after 0530 UTC are not necessarily indicative of a weaker MCS, but that stronger updraft cores could have been moving out of the analysis domain. This analysis did not go past 0600 UTC because of the MCS moving outside of the domain and from 0600 to 0625 UTC stratiform precipitation covered most of the radar analysis domain.

Chapter 5: In situ Measurements

a. Kansas Mesonets

The Hiawatha, KS Mesonet, located to the northeast of NOXP (Figure 2), interacts with convection around the same time as NOXP due to the southwest to northeast orientation of the line. However, the convection located over Hiawatha is much weaker due to multiple convective cells developing in the MCS inflow around 0430 UTC (Figure 14), which caused the temperature at the Hiawatha station to slowly decrease around 0440 UTC when the convective line passes over (Figure 36). The dewpoint decreases at an even slower rate. This slow temperature decrease over an hour period is indicative of cooling due to precipitation evaporating for an extended period of time rather than passage of a cold pool beneath a convective cell. This is also supported by the fact that the dewpoint does not change much indicating that the low levels of the atmosphere were slowly cooling and moistening as the precipitation evaporates. The wind speed and direction do not vary greatly as the line passes with wind speeds less than 3 m s^{-1} and a slight change in the wind from northeasterly to northwesterly with line passage (Figure 37). Furthermore, the Hiawatha station did not experience an increase in wind speed, which is typically associated with cold pool passage, with a peak wind speed of 3.77 m s^{-1} observed at 0520 UTC, thirty minutes after the leading edge of the convective line passes over.

A Kansas mesonet station located in Manhattan, KS which is located southwest of DOW8 and northwest of KTWX shows a large temperature drop around 0500 UTC and a gradual decrease in dewpoint (Figure 38). A cooling of about 3.5° C was observed over a thirty minute period with the sharpest decrease noted in the first five minutes,

which indicates that a surface based cold pool passed over Manhattan around 0500 UTC. At 0500 UTC, the leading edge of the bowing convective line is located over the Manhattan site providing evidence for a surface based cold pool (Figure 17). The Manhattan site also records an increase in wind speed in the twenty-five minutes before the cold pool passage as well as a peak wind speed of ~8 m s^{-1}about twenty-five minutes after cold pool passage with sustained winds from 6-8 m s^{-1} in between (Figure 39). Wind direction is initially northeasterly and backs to northwesterly as the cold pool passed over. After 0530 UTC, the wind direction varies from northeasterly to northwesterly with temperature decreasing during northwesterly wind and remaining about constant with northeasterly winds.

b. Mobile Mesonets

Two mobile mesonets were driving through the MCS environment for the three and one half hour deployment. Looking at the first hour, temperature drops as MM1 heads north (Leg 1) due to cooling associated with going further north into the cool side of the stationary front (Figure 40). When MM1 turns west, it enters the weak linear MCS. For the next half hour, we see more temperature variation due to MM1 driving in and out of convective cores within the line with temperature dropping beneath convective cores and rebounding once MM1 exits those cores. MM1 samples storm scale cold pools rather than a mesoscale cold pool that would normally be associated with MCSs since the convective line is developing a coherent cold pool at this time. There is a three degree temperature difference between the pre-MCS environmental temperature, 22.5° C, and the lowest temperature observed in the storm scale cold pool, 19.5° C which is close to the 3.5° C temperature drop observed at the Manhattan

mesonet site. Once MM1 starts driving south around 0500 UTC, two more temperature drops occur before temperature variation decreases after 0530 UTC. At this point, MM1 is sampling the environment behind the MCS including areas cooled by the storm scale cold pools so not as much variability is observed compared to the 0400 to 0430 UTC time frame.

The other mobile mesonet, MM2, drove along a north-south road throughout the deployment and captured not only the pre-MCS environment, but also the temperature drop associated with the cold pool. The temperature rises for the first forty minutes as MM2 heads south towards the stationary boundary and then decreases as it turns back north into the cooler air with the temperature profile being a mirror image around the peak at 0340 UTC (Figure 42). After the peak, temperature gradually decreases until a much sharper decrease is noted around 0425 UTC with a peak in wind speed (Figure 43). Looking at the location of MM2 and the convective line, this temperature drop is associated with MM2 driving into the convective line (Figure 44). At 0430 UTC, MM2 is in an area of rear inflow that has descended to the surface and surged ahead of the line indicating that this temperature drop is the first observation of the surface-based cold pool for the linear MCS. This is supported by previous kinematic analysis inferring a surface based cold pool starting at 0430 UTC (Figure 16). The cold pool is about 3° Celsius colder than the pre-MCS environment according to MM2's measurements, which agrees with the temperature drop recorded by MM1 in the various convective cores.

The NOXP Scout vehicle was mobile at the beginning of the deployment, evident in the odd variations in temperature and wind direction before 0400 UTC, but is

stationary at the NOXP radar site after 4 UTC and remains there for the rest of the deployment (Figure 45 and Figure 46 respectively). After 0400 UTC, temperature remains fairly constant until 0440 UTC and the wind speed gradually increases until it peaks around 0442 UTC, which is the same time that the temperature begins to drop. This wind speed maxima and temperature drop are coincident with the passage of the convective line. A vertical cross section of the radar analysis at 0440 UTC over NOXP about 2 minutes before the temperature decrease shows NOXP just ahead of a region of descending RTF flow (Figure 47). This radar cross section looks similar to the one taken over MM2 (Figure 44) with rear inflow descending to the surface within the convective line, which not only decreases the temperature but also increases the wind speed at the surface.

Comparing the cold pool passage at NOXP and MM2, the temperature decrease is about 3°C from the cold pool passage for both MMs, however the temperature drops at a slower rate at NOXP than MM2 since NOXP was stationary and MM2 was driving north into the convective line. After the initial decrease in temperature at NOXP, the temperature slowly decreases for the remainder of the IOP most likely due to cooling by precipitation evaporation as the MCS developed more precipitation behind the main line.

MG1 and MG2 were co-located with DOW7 during the IOP so that soundings from the same location could be launched more frequently for better temporal resolution. The overall profiles of temperature, dewpoint, and wind speed at MG1 and MG2 are very similar so only data from MG1 will be shown to eliminate redundancy. Looking at the temperature profile, the nocturnal stable layer surface temperature is

about a degree warmer compared to NOXP and MM2 which is expected since MG1 was located farther south and closer to the stationary front (Figure 48). Around 0505 UTC, the temperature begins to drop as the edge of the convective line passes over MG1. However the wind speed does not attain its maximum value until around 0510 UTC and decreases rapidly afterwards (Figure 49). A vertical radar cross section over MG1 at this time shows that these high wind speeds are not associated with RTF flow but with inflow into the convective line (Figure 50). The increase in wind speed suggests that inflow into the storm is being accelerated as the MCS approaches with a maximum right before the cold pool passage. This is also supported by northeasterlies in the inflow which drastically back once the wind speed drops indicating cold air advection. This suggests that the initial cooling was due to evaporation of precipitation because of the cell developing in the inflow ahead of the main line. Further cooling is brought about by cold pool passage. The rear inflow that reaches the surface is seen about 5 km to the northwest of MG1 at this analysis time. After the temperature decrease, the environment near MG1 approaches saturation because of an increase in dewpoint so that the dewpoint depression is less than a degree after the cold pool passage. It remains that way for the rest of the IOP.

MG3 was the furthest south of all the mobile mesonets and was located outside of the radar analysis domain. Due to its location, the bowing MCS did not pass over until 0600 UTC indicated by a large temperature drop at this time (Figure 51). It is clear that MG3 was south of the frontal boundary due to a pre-MCS temperature of about 26° C with few variations prior to MCS passage. Wind speeds are also generally calm during this time however wind direction begins to veer starting at 0430 UTC (Figure

52). Around 0550 UTC, temperature slightly increases before dropping about 6° C in less than fifteen minutes with an increase in wind speed. This temperature drop is much larger than any previously observed by the Kansas Mesonet stations and MMs farther north, indicating that the bowing MCS had a much larger temperature differential between the environment and the mesoscale cold pool. This doesn't necessarily imply that the cold pool is stronger, since the environmental temperature is warmer to the south of the stationary front and the temperature after cold pool passage is similar to those recorded by NOXP, MM1, and MG1. What is interesting in this case is that dewpoint decreases in a similar manner to the temperature which was not the case for the MMs farther north. This could be caused by the bowing MCS having a drier cold pool.

c. Comparison of Mesonet Observations

While analyzing the individual mesonet observations is useful, comparing them using the relative outflow boundary passage time gives more insight into these observations. The temperature of all six mesonets one hour before and one hour after the outflow boundary passage (OBP) shows that generally the furthest south mesonets had the highest initial temperature and temperature decreases further north (Figure 53). An interesting feature to note is that three of the mesonets, NOXP, MG3, and MM2, have a slight temperature increases just before the OBP, which could be due to compressional warming ahead of the cooler outflow boundary. Another interesting feature is that the rate of cooling is largest at MG3 which experienced the bowing MCS as opposed to MG1 and NOXP which have similar slopes for the temperature decrease. MM2's slope resembles MG3 since MM2 was driving into the cold pool, which would

make the temperature drop appear faster. This indicates that the rate of cooling is smaller in the linear MCS than the bowing MCS sampled by MG3, however with the observations being almost an hour apart, it could simply show that the MCS strengthened over an hour period. Despite the different environmental temperatures pre-MCS passage, the outflow temperature is between 19.5 and 21° C for all the mesonets indicating even with mesonets recording temperature at different locations and times, the cold pool remained fairly homogeneous in temperature. This is even true for Hiawatha which did not experience cold pool passage since it was too far to the northeast where elevated cells were still present. The theta-v comparison of the 6 mesonets shows similar trends to those observed in the temperature plot except that Hiawatha's theta-v value is much larger than the other mesonets (Figure 54). This supports the conclusion that Hiawatha did not experience cold pool passage like the rest of the mesonets since the cooled air is about 3 degrees warmer than the rest. The mesonets that experienced the OFB passage all have a theta-v values that converge to ~23° C, which indicates that the cold pool was fairly homogeneous over a large spatial and temporal domain.

d. **H-Z Sounding Analysis through MCS**

An analysis of soundings launched from MG1 and MG2 at the same location for about a five hour period from 0215 to 0702 UTC covers the pre-MCS through the post-MCS mesoscale environment (Figure 55). Weak ascent begins around 0347 UTC (0.25 m s^{-1}) over an hour prior to MCS passage and increases in magnitude to approximately 1 m s^{-1} at 1 km as an elevated maximum just above the elevated residual layer mentioned earlier. The magnitude of this ascent is slightly larger than the values noted

in the sounding analysis across the stationary front (Figure 4) however this area of ascent is located well north of the front. The ascent increases in magnitude once inside the convective line as would be expected with mesoscale ascent values around 5 m s^{-1}.

The decrease of low level water vapor mixing around 20 km ahead of the outflow boundary passage coincides with the beginning of the weak ascent ahead of the MCS (Fig. 55a). Above 3 km, water vapor mixing ratio values below 8 g kg^{-1} increase in thickness and extend further in the vertical indicating that moisture from about the EML is being brought up into the mid-levels of the atmosphere. Behind the area of stronger updrafts, the q_v values decreases in the drier rear inflow beneath the stratiform precipitation area in weak subsidence.

The theta-v' field shows mostly conserved ascent with some slight cooling within the updraft region of the MCS below the 0° C isotherm (Fig. 55b). Above this level, positive perturbations are maintained through 12 km. The coldest air can be seen between 500 m and 1 km about 20 km behind the passage of the outflow boundary indicating that the coldest air isn't located along the leading edge of the cold pool but slightly aloft. The temperature drop at the surface occurs just after OFB passage and gradually cools over 20 km. This is also supported by MM observations which showed the temperature drop over a period of time rather than an abrupt change like a step function. The coldest air in the entire sounding analysis domain is located above the updraft due to continued cooling aloft after the moisture has been condensed out of the air parcels.

The warmest air ahead of the MCS in theta-e (Fig. 55c) and theta-w (Fig. 57d) is from 0.5-2 km, which is consistent with the elevated residual layer location in the

frontal sounding analysis. Once weak ascent begins, this layer cools and the nose of the warmest air is slightly lifted because after the air from south of the front is cooled from ascent over the frontal boundary, it is cooled further due to mesoscale ascent ahead of the MCS. While the ascent magnitudes of the frontal lift and the mesoscale lift are both rather small, they have a large impact on priming the pre-MCS environment for convection. Another thing to note in both theta fields is that an inversion is always present even with the cooling in the elevated residual layer, indicating that this environment is stable in the lowest levels throughout the MCS lifetime. Within the mesoscale updraft, theta-e and theta-w do not change rapidly with height like in the nocturnal stable layer since the variables are somewhat conserved during ascent.

One of the soundings labeled as P0520 was not actually launched during the IOP, since balloon launches were not possible in the convective line, rather instead was constructed using the DLA output (Figure 56). The main thing to note from the sounding is the 3 updraft maximums at 3.5 km, 6.5 km, and 12 km which is consistent with results from the radar analysis showing a lower updraft maximum along the leading line, a mid-level updraft maximum due to the more mature cells in the line, and an upper level maximum due to ice processes.

Chapter 6: Diabatic Lagrangian Analysis Results

a. Trajectory analysis

In order to answer the earlier question about whether the updrafts in the convective line of the MCS were elevated or surface based, an analysis on the origin levels of the trajectories from 0400 to 0600 UTC is shown with warmer colors indicating a larger number of trajectories (Figure 57). One of the first things to note is that over the analysis period the overall number of trajectories increases as the MCS strengthens with the lowest number of trajectories in the first thirty minutes. Most trajectories come from the lowest 4 km for the entire analysis time. After 0430 UTC, a larger number of trajectories come from the lowest 2.5 km and around 0440 UTC, when the outflow surge feature is first observed, the largest number of trajectories comes from the lowest 0.5 km. This is around the same time that MM2 and NOXP measure a surface based cold pool. It is hypothesized that the sudden increase in trajectories from lower levels is due to forced lifting from the cold pool. The majority of trajectories come from the lowest 0.5-1 km after 0500 UTC which is when the bowing MCS develops and the strongest updrafts are observed in the radar analysis. This continues until the end of the analysis period at 0600 UTC.

While it could be argued that the MCS was elevated prior to the beginning of the analysis time at 0400 UTC, air parcels from the lowest kilometer are being ingested by convective line updrafts. This trajectory analysis shows that the updrafts in the convective line are neither purely elevated nor strictly surface-based, but are lifting parcels from the lowest 2.5 km with a large portion of the trajectories being from the lowest 500 m after 0500 UTC. This again emphasizes that nocturnal MCSs should be

characterized on a continuum from elevated to surface-based, recognizing that storms are able to ingest air from both the elevated residual layer and the stable surface layer.

Another trajectory analysis was done on surface downdrafts to determine their source layers (Figure 58). This analysis clearly shows that most of the downdraft air originates from the lowest 0.5 km level for the entire time period. Later on in the time period, more air from higher levels (0.5-2 km) is able to be brought down into the surface based downdrafts as the MCS matures and intensifies.

b. 0400 UTC

0400 UTC is the first DLA analysis time since an hour of 3-D wind analysis is preferred before the initial analysis time so that trajectories have time to go back to the initial environment. Reflectivity, theta-v', theta-e, and initial trajectory height are plotted for 0400 UTC at the same location as the vertical cross section shown previously in the radar analysis section (Figure 59). In the theta-v' plot, cooler temperatures are near the surface where the rear inflow dips towards the surface in association with the highest reflectivity core (Fig. 59b). The warmer theta-v' bubble in the inflow region below the 0° isotherm is caused by adiabatic warming due to the large downdrafts (up to -10 m s^{-1}) in the developing anvil. Cold air (-10° C and colder) is seen above the main updraft cores. Initial trajectory height shows most of the air feeding the updrafts are from above 3 km while the trajectories for the RTF flow are from the lowest 3 km (Fig. 59c). No air parcels from below the stable inversion are being lifted into the updraft cores at this time which supports the idea that the initial convective line was elevated. Warmer theta-e values in the inflow region are not being lifted into the main updrafts which confirms

what the theta-v' and initial trajectory height plots are showing (Fig. 59d). Also note that the coldest theta-e air is in the RTF flow and is located right below the 0°C isotherm.

Reflectivity, snow mixing ratio, graupel mixing ratio, and rain mixing ratio are shown together to observe trends in precipitation mixing ratios (Figure 60). The highest values of rain mixing ratio are co-located with the 50 dBZ reflectivity maximum and also directly below the graupel mixing ratio maximum implying that the higher concentrations of rain are due to graupel melting (Fig. 60c and Fig. 60d). The graupel maximum is also located just downwind and below the strongest updraft core, which is expected since the graupel forms in the stronger updrafts and falls out once it is too heavy to be suspended by the updraft. An interesting feature that shows up throughout the analyses is the small area of rain mixing ratio above the 0° isotherm which is co-located with a hole in the snow mixing ratio implying the presence of supercooled water (Fig. 60c and Fig 60b). This leads to a mixed-phase region at the base of the 15 m s^{-1} updraft core. The snow mixing ratio is highest above and around the stronger updraft cores. It spreads out and decreases as the FTR flow advects it into the anvil and behind the convective line.

Looking next at water vapor mixing ratio (q_v), theta, ice mixing ratio, and cloud mixing ratio, the q_v plot shows values below 1 g kg^{-1} co-located with the anomalously warm bubble noted in theta-v' implying that subsidence below the downdrafts is responsible for drying and warming the air in the inflow (Figure 61). Also the highest value of q_v is located at the surface in the inflow region but does not get lifted into the convective line updrafts despite the bump in moisture along the RTF and FTR flow interface (Fig. 61a). One feature to note in both q_v and theta is waves that appear to

crest around 3 km and are spaced every 10 km apart (Fig. 61a and Fig. 61b). These features may have been waves in the stable inversion layer. However, the dynamics of these features including the ducting mechanism is beyond the scope of this study and likely cannot be addressed from our observations. This was the only clear indication of waves in the environment unlike previous studies (Marsham et al. 2011) which typically show evidence of bores or wave trains in radar fine lines. The same bump in q_v underneath the leading line updraft is also seen in theta and the layer of colder theta values become deeper once the RTF flow is present. Looking at the ice mixing ratios, low values are present above the -40° C isotherm (Fig. 61c). The largest values of cloud mixing ratio are evident in the leading line updraft along the RTF and FTR flow interface (Fig. 61d).

c. 0430 UTC

The MCS has organized considerably by 0430 UTC as revealed by the reflectivity, theta-v', initial trajectory height, and theta-e plotted (Figure 62). Positive theta-v' air is in all the updraft cores including the cell developing ahead of the main line which was not apparent at 0400 UTC (Fig. 62b). There is also an area of negative theta-v' air at the surface below the main updrafts of the convective line and under the areas with the largest reflectivity values, implying that diabatic cooling is driving these negative theta-v' perturbations. There is also a large negative theta-v' perturbation above the 15 m s^{-1} contour in the most rearward updraft in the convective line due to the convection becoming stronger which allows the updraft to overshoot the tropopause.

Looking at initial trajectory height, most of the air in the updrafts originated below 3 km which is in stark contrast to 0400 UTC (Fig. 62c). This is noted in the

updraft trajectory plot (Figure 57) with a shift of most trajectories coming from mid-levels to below 3 km around 0430 UTC. While none of the air is from the lowest 1 km, a large portion of the updrafts are being fed by the 1-2 km layer, implying that the MCS is ingesting air from lower levels as it intensifies. Even the cell initiating along the edge of the outflow has most of its trajectory origins between 1 and 2 km.

The rear inflow trajectories with the coolest theta-e values come from the 3-6 km level while the lower, warmer theta-e air at the surface is from the lowest kilometer. Theta-e also shows a small plume of warmer air from the surface in the updraft of one of the cells in the convective line (Fig. 62d).

The fields of reflectivity, rain mixing ratio, graupel mixing ratio, and snow mixing ratio reveal that the rain mixing ratio maximum is located in an area of reflectivity exceeding 60 dBZ (Figure 63). The graupel/hail mixing ratio plot shows a lowering in the higher values of mixing ratio towards the surface located just above this maxima in rain mixing ratio implying that this maximum in rain is due to melting graupel from a descending reflectivity core (Fig. 63d and Fig. 63c). While the peak graupel values are not located directly above the rain maximum, one is behind an updraft core and the other is located directly beneath the strongest updraft core to the rear of the system. Fallout from both of these maximums is likely contributing to the high rain mixing ratios seen at the surface.

There are larger areas of high snow mixing ratios compared to the previous time due to updrafts strengthening, increasing in areal coverage, and producing more ice (Fig. 63b). Similar to the previous time, there appears to be a “hole” in the snow mixing ratios at the base of the strongest updraft, since this area is probably a mixed phase

region and isn't conducive for snow growth. One final thing to note is the cell that initiated right along the edge of the outflow boundary has generated graupel and snow even with a weaker 5 m s^{-1} updraft.

Looking at q_v, theta, ice mixing ratio, and cloud mixing ratio, we see that the wave-like feature noted at 0400 UTC is not as apparent in the q_v and theta fields with only 2-3 waves visible in each field (Figure 64a and Figure 64b). It is hypothesized that this is due to the low-levels destabilizing because of the MCS, which isn't conducive to wave ducting. There are higher values of q_v at the surface in the outflow implying that rain evaporation in the drier air is moistening the RTF flow. There is also a small upward bump in the moisture field underneath the leading line updraft with the isolated cell. Compared to 0400 UTC, there are pockets of higher ice mixing ratios located above the updraft cores and the area of the lowest ice mixing ratio values has expanded further out in the anvil (Figure 64c). Cloud mixing ratios are significantly higher especially along the leading edge and cover a much larger area than previously. There is also a thin layer of very low cloud water mixing ratio at the surface in the outflow, which indicates that a thin fog is present.

d. 0500 UTC

At 0500 UTC, the linear MCS intensifies as the bowing MCS develops. Theta-v' values in the updrafts have a large positive perturbation that extends further vertically than any previous time indicating more buoyancy in the air parcels in the updrafts (Figure 65b). While the largest cold perturbations in the RTF flow are the same as 0430 UTC, they cover a larger area although these values are located towards the rear of the convective line rather than at the leading edge of the OFB. This is similar to what was

seen in the mesonet data with a gradual cooling as the convective line passed rather than a steep temperature drop. 0500 UTC is when trajectories in the updraft originate in the lowest kilometer (Figure 57) indicating that surface based air, which is typically considered stable in nocturnal environments, contains buoyancy and contributes to the convective line updrafts.

There is an interesting pattern in theta-e with cold air in the RTF flow located at the surface originating from the below 1 km, while the RTF flow further aloft originates from higher altitudes but isn't as cold. There is also a plume of warmer theta-e air that extends from the surface up to 5 km along the leading edge of the outflow boundary which supports the trajectory analysis that air from the surface is being lifting into the convective line updrafts (Figure 65d).

Looking at precipitation mixing ratios, the rain mixing ratio maxima is lower than at the previous time but that is mainly due to lower reflectivity values since the 0430 UTC cross section captured a descending reflectivity core (Figure 66c). Despite the rain concentrations being lower, there are still larger values beneath areas of higher graupel mixing ratio which cover a larger area than previous analyses (Figure 66d). Snow mixing ratio values and areal coverage are similar to the 0430 UTC analysis including the previously mentioned "hole" at the base of the 10 m s^{-1} updraft (Figure 66b). This region is co-located with an area of low rain mixing ratio which supports the idea that this "hole" is a mixed phase region with rain, snow, and graupel present.

The previously mentioned wave in the q_v and theta field is completely gone due to MCS intensification (Figure 67). The moisture is deeper in the inflow region of the MCS which may contribute to more trajectories coming from the lower levels since the

environment is moistening and would have larger CAPE values (Figure 67a). An interesting feature in the theta field is a ~4 km thick layer with nearly constant theta values (55-60° C) in a 10 m s^{-1} updraft since this layer is only 1 km thick throughout the rest of the cross section (Figure 67b). The ice mixing ratio plot looks similar to the 0430 UTC analysis (Figure 67c). Cloud mixing ratio maxima values are lower however there is a 17 km long section of low mixing ratios that stretches across the surface below the first two updraft cores (Figure 67d). Higher values of cloud mixing ratio still follow the top of the interface between the RTF and FTR flow.

e. 0520 UTC

DLA output can be used to help confirm some ideas about what forced severe winds and led to the severe wind report at 0520 UTC in the bowing MCS. Looking first at theta-v' at the 0.5 km level, the wind report denoted by a "W" is in the middle of an area of cooler theta-v' perturbations (-4° C) with the colder air coming from the north and west (Figure 68). This advection of cold air is due to strong northerly outflow in the region of colder theta-v' perturbations and stops once the outflow encounters the southerly inflow into the MCS (denoted by the thick black line). This advection of cold air happens over a 40 km distance starting where the westerly flow curves southward and ending at the inflow.

A vertical north-south cross section parallel to the outflow along with DLA output of snow, graupel, and rain mixing ratio shows high values of snow mixing ratio located above the strongest updraft cores and higher values of graupel within the updraft cores (Figure 69). However, the highest concentration of graupel is located behind the strongest updraft core and is co-located with the highest reflectivity values.

This could possibly be a descending reflectivity core from a dying cell. Below the reflectivity maximum, there is a reflectivity streak which was previously mentioned in the radar analysis at this time. This reflectivity streak is characterized by higher rain mixing ratios that lead up to the location of the wind report. This area of high rain mixing ratio is due to graupel melting, which would cool the air and allow it to descend more rapidly. This could cause surface winds to accelerate fast enough to produce a wind report.

f. 0530 UTC

By 0530 UTC, both the linear and bowing portions of the MCS have continued to intensify including the severe wind report at 0521 UTC. The initial trajectory height field reveals a persistent source of updraft inflow from the lowest kilometer (Figure 70c), which is consistent with the slight increase of updraft inflow trajectories originating from the lowest 2 kilometers from 0500 UTC to 0530 UTC in the overall trajectory origins plot (Figure 57). Most of the air in the RTF flow is still from the lowest kilometer, which is consistent with the 0500 UTC analysis. Although the magnitude of the warm theta-v' perturbations is not as large in the present cross-section as at 0500 UTC, the warm theta-v' perturbations at 0530 UTC nevertheless cover a large area of the FTR flow in the cross-section (Figure 70b). The theta-e plot reflects the trajectory analysis in showing that more air from 3-5 km is being dynamically entrained into the middle to upper level updrafts (Figure 70d).

Looking at reflectivity and precipitation mixing ratios, the snow mixing ratio plot shows very well the multicellular nature of the convective line with maximums in three different updraft cores (Figure 71b). Snow mixing ratio values are much higher

even outside the main updraft cores and cover a large area. The graupel mixing ratio plot shows the largest values associated with the cell developing along the leading edge of the OFB (Figure 71d). The OFB is much steeper, as discussed previously in the radar analysis chapter, so perhaps enhanced lifting at the edge of the OFB is allowing for more graupel production. In previous analyses, high graupel concentrations are associated with the strongest updraft cores however that is the not the case at 0530 UTC. An interesting feature in the rain mixing ratio plot is the updraft that extends down into the RTF flow appears to be lifting rain that is being carried in the RTF flow to the 0° C isotherm when normally rain is seen well below this level (Figure 71c). Another thing to note is the small areas showing very low values of rain mixing ratio around the -20° C level. While the updrafts in this cross section do not show rain being lofted to that level, perhaps flow perpendicular to the cross section is bringing rain aloft and contributing to mixed phase regions.

The q_v field shows a deepening of the moisture ahead of the MCS and throughout the line which is similar to the 0500 UTC analysis (Figure 72a). The theta field does not have a thick layer of constant theta like at 0500 UTC however the 60-65 degree Celsius range does become thicker in the updrafts of the MCS (Figure 72b). The overall amount of ice is lower than previous analyses however snow mixing ratios are much higher indicating that the ice mixing ratios are low due to aggregation to form snow (Figure 72c). Cloud mixing ratio is concentrated primarily above the descending RTF flow, the latter being similar to previous times (Figure 72d).

g. 0600 UTC

Since the convective line of the MCS is exiting the radar analysis domain after this time, the final DLA analysis time is 0600 UTC (Figure 73). The reflectivity cross-section reveals that the leading convective line is partially resolved (Figure 73a). The warmest theta-v' perturbations extend vertically from the base of the FTR flow within updraft regions toward the -40° C isotherm. These warm theta-v' perturbations around the -40° C isotherm suggest that ice processes are augmenting the buoyancy in concert with dominant condensational latent heating (Figure 73b). The coldest theta-v' perturbations are located around 1 km in the RTF flow and spread across a much larger area than any previous analysis, indicating that the MCS is continuing to sustain and intensify the surface based cold pool. It should be noted that the ambient inflow environmental theta-v profile, from which the theta-v perturbation field is calculated, is characterized by a warm, stable layer around 1 km.

Initial trajectory heights (Figure 73c) show that most of the air parcels being ingested in the updrafts are from the lowest 2 km, with air from the lowest kilometer contributing a sizeable portion of the total updraft mass flux as indicated by the overall updraft trajectory analysis (Figure 57). Most of the air parcels in the RTF flow originate below 1 km, with only a few small pockets of air from 1-4 km, which is quite different than any previous analysis time. Also unlike previous analyses, the coolest theta-e air in the RTF flow is not coincident with the air from higher heights according to the initial trajectory analysis (Figure 73d). The highest magnitudes of positive theta-v' are also coincident with the largest values of theta-e.

Focusing on the precipitation mixing ratios, the snow mixing ratio maxima are similar to previous times (Figure 74b). However at 0600 UTC higher mixing ratio

values are extending towards the rear of the system at the same time that a stratiform region is beginning to develop behind the linear MCS. This indicates that as the line and the FTR flow each intensified, the FTR flow was able to carry larger amounts of snow rearward to seed the developing stratiform region.

One other thing to note in the snow mixing ratio plot is an area of very low snow mixing ratio that is in the same location as a large area of low rain mixing ratio values above the 0° C isotherm (Figure 74c). These areas also overlap with low values of graupel mixing ratio, indicating that these are mixed phase regions of the convective line (Figure 74d). Similar to previous times, it appears that the updrafts are lifting rain from the descending RTF flow back into the convective cores leading to these regions. The highest graupel mixing ratio value is associated with the cell near the edge of the outflow boundary similar to the 0530 UTC analysis. The graupel mixing ratio values are consistently high in the updraft cores and there is a slight downward dip in these values located directly above the weak, elevated maximum in rain mixing ratio which is associated with a descending reflectivity core.

The q_v field shows similar trends of a bump in moisture ahead of the line and the theta field shows a thin layer of the coldest air at the surface in the RTF flow (Figure 75a). Cloud ice mixing ratio values are again small (Figure 75c), but snow mixing ratios were very large at this time similar to conditions at 0530 UTC. The cloud water mixing ratio maximum is still located above the interface between the RTF and FTR flow, however now there are also very small cloud mixing ratio values across nearly the entire area below the -40° C isotherm which was not seen on any previous analysis (Figure 75d). This may be due to increasing graupel/hail contents and melting into the RTF

flow, thereby cooling the RTF flow layer and allowing very low cloud mixing ratios to increase behind the main convective line due to melting-induced weak cloud condensation.

h. Theta v' throughout MCS development

Horizontal plots of theta-v' at 0.5 km are shown at 0400, 0500, and 0600 UTC to analyze the change in theta-v' as the MCS's mesoscale cold pool developed (Figure 76, Figure 77, and Figure 78 respectively). Looking first at 0400 UTC, the difference in theta-v' underneath and ahead of the convective line shows some evidence of a weak surface based cold pool with theta v' perturbations of -4° C under the higher reflectivity values and -2°C ahead of the convective line (Figure 76). The positive theta-v' perturbation area near NOXP could be due to subsidence warming due to downdrafts similar to the warming seen in the cross section through the line (Figure 59). At the southwestern edge of the domain, an area of positive theta-v' perturbations is located where the future bowing MCS will develop indicating this region had more available buoyancy for convection compared to the environment ahead of the present linear MCS. Overall, this theta-v' plot indicates that the low-level environment is not conducive to surface based convection and supports the previous evidence of an elevated MCS at this time.

One hour later at 0500 UTC, the colder theta-v' air is no longer in the inflow region but beneath the main convective line in both the linear and bowing MCS, and the coldest theta-v' air is located just behind the most intense convection in the linear MCS (Figure 77). This supports the previous evidence that the MCS had developed a surface based cold pool by 0500 UTC which helped the MCS to intensify and propagate quicker

to the southeast. Also note that the cross section (Figure 65) goes through the coldest air indicating that the theta-v' cross section shows the strongest region of the cold pool. This horizontal plot shows that the previously mentioned anti-cyclonic circulation behind the convective region of the bowing MCS is funneling colder outflow southward and allowing it to surge out. This is the mechanism that will lead to the wind report which occurred twenty-one minutes after this analysis time.

Most of the DLA domain at 0600 UTC reveals a large area of negative theta-v' perturbations behind the convective line which covers a larger area than at any previous analysis time (Figure 78). There are also small pockets of positive theta-v' perturbations along the edge of the convective line indicating that parcels at 0.5 km have buoyancy ahead of the convective line. This illustrates that parcels below the inversion could be contributing to the system. Another feature to note is that some locations along the line have a sharp gradient in theta-v'. Other areas have more diffuse gradients similar to how the MM observations show gradual temperature decreases rather than sharp step-function decreases, with the exception of MG3 which noted a sharp decrease (Figure 51).

i. Time-height mixing ratio for ice, cloud, snow, graupel, and rain

Time-height plots similar to those constructed for reflectivity and updraft maxima (Figure 35) were made for cloud water and cloud ice (Figure 79), snow (Figure 80), and rain and graupel/hail mixing ratio (Figure 81). The plot of maximum cloud ice and cloud water mixing ratios versus height shows that increases in ice mixing ratio magnitude are coincident with increases in cloud mixing ratio magnitude (Figure 79). After an initial cloud ice mixing ratio of 4 g kg^{-1} at 11 km, the value decreases and

doesn’t increase until around the time that the outflow surge associated with the anticyclonic circulation begins to develop. About 10 minutes before the wind report (the latter denoted by the "W" symbol), the cloud ice mixing ratio reaches a maximum value of 8 g kg^{-1} from 11-12 km at the same time that updraft speeds increase. After the wind report, the cloud ice maximum decreases and stays lower for the rest of the analysis. The cloud water mixing ratio plot shows larger values initially which decrease after 0420 UTC perhaps due to increased precipitation scavenging associated with increasing reflectivity at this time. The cloud water mixing ratio does not increase again until around 0450 UTC, which is coincident with an increase in updraft speed about ten minutes after the surging outflow feature is first noted. As updraft speeds continue to increase up until the time of the wind report, the maximum value of cloud water mixing ratio increases in magnitude and in height so that at the time of the wind report, large values of cloud water mixing ratio are about ½ a kilometer above the -40° C isotherm. After this maximum, there is one final maximum a bit lower in height and magnitude around 0535 UTC before the cloud water and ice mixing ratios taper off.

Plots of maximum snow volume and mass both show pulses of higher values until around 0450 UTC when the maximum values become consistent over time (Figure 80). By 0500 UTC, maximum values are reached and stay at that magnitude for most of the time period with a decreases around 0550 UTC, which is most likely due to the convective line moving out of the DLA domain. One thing to note is the maximum in snow volume from 0510 to 0600 UTC increases in height from having a base around 6 km at 0510 UTC to around 8 km at 0600 UTC implying a 2 km increase. This increase is around the same time that updraft volume increased implying that updrafts were

covering a larger volume of the MCS and were able to lift more snow particles higher. The largest values of snow volume cover almost the entire area between 0 and -40° C whereas snow mass is more concentrated around the -20° C isotherm, near the dendritic growth zone. This makes sense intuitively because dendrites are the largest snow crystals and would contribute the most to the mass. Snow mass does not show an increase in height like snow volume does, implying that the height of the maximum in snow mass is not tied to updraft volume but is more dependent on the height of the dendritic growth region which changes little over time.

The time-height plots of graupel/hail and rain mixing ratio show an overall trend that increases in mixing ratio are time-lagged behind an increase in updraft speed with at times a decrease in dBZ and mixing ratio when updraft first increases (Figure 81). When updraft magnitude initially increases, it allows for more particles to be lofted higher up and stored at altitude for longer periods of time. Hence, precipitation fallout is initially delayed, which in turn leads to the initial decrease in dBZ. This explains the time lag between updraft magnitude increase and increases in mixing ratio and dBZ. The highest values of rain mixing ratio are present at the surface as expected. Values at the surface are initially large (between 3.5 and 4 g kg^{-1}) for the first 40 minutes, then drop off to below 2.5 g kg^{-1} between 0430 and 0530 UTC. This decrease is most likely due to updraft magnitude and area increasing over this time period as the MCS goes through upscale growth. After 0530 UTC the values at the surface increase but are not as high as the initial values.

One thing to note is the maximum in rain mixing ratios above the 0°C isotherm which becomes consistent after 0435 UTC. This is indicative of the presence of

supercooled rain water in the strongest updrafts. This feature is consistent with meltwater rain that subsequently recycles upward in strong updrafts. This elevated supercooled rain water mixing ratio feature does not appear above 7.5 km, due to heterogeneous freezing of large rain drops. These features are often coincident with increases in graupel/hail mixing ratio since frozen rain drops are often graupel/hail embryos. This makes sense physically as subsequent graupel/hail growth is aided by supercooled water riming onto the frozen drops within strong convective updrafts. The overall values of graupel/hail mixing ratio are rather small during the early development phase, but increase explosively after 0530 UTC. Meltwater rain mixing ratios increase commensurately with increasing graupel/hail both at the surface and above the 0° C isotherm. This is likely due in part to the intensifying updrafts that had been developing in the bowing MCS that first appear around 0500 UTC, which is the start of a rapid intensification period according to maximum updraft values. These updrafts are most likely located in the bowing MCS due to its proximity to warmer, moister inflow air from the warm sector south of the front. The warmer, more moist storm inflow would allow for more thermal buoyancy in a few intense convective cores. After 0530 UTC we also see an increase in the height of the maximum value of graupel/hail mixing ratio, which occurs at the same time as an increase in the height of the rain mixing ratios above the 0° C isotherm.

j. **Melting and Evaporative Cooling**

Melting of graupel/hail and rain evaporation are the main contributors to diabatic cooling in the convective and storm scale downdrafts that subsequently forces the development of the surface-based cold pool. At 0400 UTC, the integrated diabatic

cooling from rain evaporation along each trajectory (degrees K) is shown in the top panel (Figure 82). Since it is early in the life of the MCS, the integrated diabatic cooling values are generally low (only getting up to 4.5 degrees K) with the maximum values located near the surface. Although most of the integrated rain evaporative cooling is confined to the lowest 4 km, a narrow column of rising air that originally passed through the melting layer extends vertically in a stronger updraft core. The maximum value is in the lowest 2.5 km with the exception of the evaporation along the leading interface between the FTR and RTF flow.

The graupel/hail melting rates (Figure 82, bottom panel) are larger in magnitude than rain evaporation throughout the entire analysis period (i.e., note the scale difference between the rain evaporation and graupel/hail melting plots). The maximum in graupel/hail melting is located above the maximum in rain evaporation and concentrated in the 1-3 km layer. The largest values of cooling by graupel/hail melting are on the back edge of the reflectivity maximum which is also where the highest amounts of graupel/hail mixing ratio are located (Figure 60).

Rain evaporation values at 0430 UTC are slightly larger than the values at 0400 UTC however the height of the maximum has shifted up and is not as close to the surface (Figure 83). Also, the maximum located along the leading edge of the RTF and FTR flow interface is no longer present, but a tendril of cooling begins at the leading edge and follows the flow up into a strong updraft. The graupel/hail melting rates (bottom panel) are much larger than at the previous analysis time due to a descending reflectivity core with reflectivity values of 55 dBZ which also correlates to large values of graupel mixing ratio (Figure 63). The depth of graupel melting is much thicker

(between 1 and 5 km) than the previous time due to larger values of graupel. Another thing to note is that lower values of cooling (below 2 degrees Kelvin) cover a large portion of the domain at this time.

Moving on to 0500 UTC, the maxima for both melting and evaporation are slightly lower than at 0430 UTC but that is most likely due to lower reflectivity values in the domain and does not necessarily indicate that the system was weakening (Figure 84). The majority of cooling from rain evaporation is still located towards the rear of the convective line since the cells with the longest lifetime, and therefore precipitating the longest, would be further back in the line. The maximum in cooling is located at 1 km in height above ground which is slightly lower than at 0430 UTC. Low values of cooling due to graupel/hail melting are still consistent over a large portion of the domain. Integrated melting cooling rates of 3-4 degrees Kelvin have reached the surface behind some of the descending reflectivity cores associated with older convective cells. A final thing to note is that the cooling rates from graupel/hail in the updrafts have increased by about a degree from the previous analysis.

Cooling rates are also analyzed at 0520 UTC to see the impact of melting and evaporation on the air that descended as cool, southerly outflow leading to the first wind report (Figure 85). While both rain evaporation and graupel melting contributed to cooling the southerly outflow, graupel melting dominated the cooling process with maximum cooling values between 7.5 and 8 degrees Kelvin. This supports the earlier conclusion that diabatic cooling created a density current at the surface which propagated towards the south and led to a wind report.

At 0530 UTC, rain evaporation cooling is present across the entire surface in the domain even though the maximum value appears to be shifted further back relative to the leading edge of the line (Figure 86). The maximum at the leading edge of the FTR and RTF interface is present again with a tendril extending into the main updrafts of the convective line. The rain maximum is co-located with a maximum in cooling from graupel melting which isn't as large in magnitude as in previous analysis times. However, similar to cooling by rain evaporation, cooling due to graupel melting covers an extensive area of the convective line.

By 0600 UTC, we see similar trends of cooling covering a large portion of the convective line however the magnitudes of cooling by rain evaporation and graupel melting have increased by about 2 degrees for rain evaporation and 4 degrees for graupel melting (Figure 87). Looking specifically at rain evaporation, a secondary maximum is present around 13 km which is likely caused by recycling of meltwater-cooled air to altitude within locally intense updrafts. The graupel maximum is the largest out of all the analyses with a value between 16 and 17 degrees Kelvin. This maximum also seems to be shifted up slightly, with a majority of the maximum between 2 and 6 km. Unlike previous analyses, the graupel maximum extends throughout the entire length of the convective line and has much higher magnitudes of cooling in the updrafts.

Chapter 7: Discussion

While previous results chapters presented different aspects of the analysis, this discussion will attempt to bridge between the multiple measuring platforms to bring together a cohesive review of the June 25-26 2015 Kansas MCS. The isolated cells that began to form around 0230 UTC were supported by elevated CAPE (Figure 10) that was enhanced by an elevated mixed layer due to the stationary front to the south. This frontal lifting was analyzed using four north-south soundings oriented perpendicular to the front (Figure 4) to illustrate the weak ascent and warm air advection due to the boundary which has been found to help focus convection in multiple studies such as Zheng et al. 1995; Jirak and Cotton 2007; Coniglio et al. 2010; Wetzel et al. 1983; Maddox 1983, 1980; Johns and Hirt 1987; Trier et al. 2011; Trier and Parsons 1993; and Gale et al. 2002. While there was no LLJ, which was present in some of the studies, the transport of warm air over the front was clearly an important factor in the initial convective cells initiation. Similar to other nocturnal convection studies, these initial cells were based above the surface layer which is supported by early radar analyses (Figure 8) and surface measurements at Hiawatha which do not show any evidence of a surface based cold pool with calm wind speeds, no discernible wind shift, and gradual cooling by evaporation (Figure 36 and Figure 37).

By 0400 UTC, the isolated convective cells had merged into an elevated linear MCS (Figure 11) with trajectory origin analysis at this time showing most trajectories from an elevated layer (Figure 57). Further evidence for an elevated convective line comes from wave like features noted for DLA output q_v and theta (Figure 61). Approximately four wave crests were noted in the analysis with the first one located at

the RTF and FTR interface. Many studies have highlighted the importance of waves to sustain elevated convection at night (Schmidt and Cotton 1990), that the stability in the nocturnal boundary layer leads to systems that propagate due to waves (Carbone et al. 1990), and that systems without surface based cold pools lift with bores or waves (Marsham et al. 2011). At this time downdrafts from the convective cells in the line would not be cold enough to descend to the surface and would instead induce a wave on top of the frontal inversion. While the limitations of this study do not allow us to determine whether wave dynamics led to sustained lifting for the linear MCS, a surface based cold pool was not evident at this time. This in turn implies that a wave-like lifting mechanism was hypothetically the most likely lifting mechanism which was the case in Marsham et al (2011).

By 0430 UTC, the waves are much less noticeable (Figure 64) due to the destabilization of the environment as the linear MCS transitioned to being surface-based which would inhibit waves. This transition from elevated to surface-based convection was due to the development of a surface-based cold pool. The first mobile mesonet to measure cold air at the surface was MM1 which drove through multiple convective cores starting around 0415 UTC when the line was still elevated (Figure 40). It recorded multiple drops and rises in temperature coincident with driving in and out of storm scale cold pools generated by convective cells. At this point, the storm scale cold pools had not merged together to form a mesoscale surface based cold pool. These storm scale cold pools were driven by diabatic cooling from graupel melting and rain evaporation as shown in the descending reflectivity core in 0430 UTC which had high values of graupel mixing ratio (Figure 63) and also large values of cooling due to graupel melting

(Figure 83). Once the diabatic cooling became large enough, a surface based cold pool was detected by mobile mesonets while the radar analysis showed evidence of convergence along the leading line between inflow and the OFB.

After 0500 UTC, most of the trajectories originated from the lowest 500 m (Figure 57) and the surface based bowing MCS developed (Figure 17). Looking at the winds vectors in the 0.5 km radar analysis at 0500 UTC, convergence was evident at the leading edge of the convective lines for the bowing and linear MCS which has been used in previous studies such as Wilson and Roberts 2006 to indicate that a system is surface based (Figure 17). Also many studies such as Billings and Parker (2012) and Parker (2008) have defined surface based convection as a system that ingests parcels below 500 m while Corfidi et al. (2008) defined a storm as surface based when air going into the updrafts was coming mainly from the PBL. Both the linear and bowing MCS fit the definition for surface based convection from all of these studies with trajectories from the lowest 500 m which would also be from the PBL. Air from the stable layer had enough CAPE to help sustain the convective line updrafts (Schumacher 2015). Further evidence that the MCS was surface based is the severe wind report which occurred at 0520 UTC due to surging cold outflow. Cold pools have been shown to be a key factor in whether a storm can produce severe surface winds since the mesoscale pressure gradients in cold pools can cause severe winds without downdrafts (Bryan and Weisman 2006; Kuchera and Parker 2006). Schmidt and Cotton (1989) showed that systems with stable PBLs, such as a nocturnal environment, can still produce damaging winds at the surface. The surging surface based cold pool was caused by diabatic cooling due to melting of graupel and rain evaporation leading to a density

current that caused the severe wind report at 0520 UTC, not a downdraft, which implies the mechanisms in the previously mentioned studies were at work in the bowing MCS.

Both the linear and bowing MCS continued to intensify throughout the IOP and develop a stratiform rain region however the bowing MCS was the first to develop one. The more intense, surface based bowing MCS was likely advecting more ice particles rearward in its more intense FTR flow due to stronger convective updrafts. Multiple studies have shown that a strong FTR flow is necessary to develop a stratiform rain region (Smull and Houze 1987a; Rutledge and Houze 1987; Watson et al. 1988). However another mechanism that inhibited the linear MCS from initially developing a stratiform rain region was likely the presence of convection behind the line which initiated due to lift over the cold pool. This was similar to the "bow and arrow" mechanism described by Keene and Schumacher (2013). The lifting of warm air over the cold pool continued until the bowing MCS developed a stratiform rain region which cut off the southerly flow and allowed the linear MCS to develop a stratiform region.

Parker (2008) described a surface-based squall line going through distinct phases as it progresses through an environment that is cooling, similar to the development of a nocturnal boundary layer. These phases were strengthening where the cold pool develops and intensifies, quasi-steady where the squall line develops new convection along the OFB which lifts as a density current, stalling where the cold pool to environmental temperature deficit becomes small so that forward progress slows and the storm goes through a secondary maximum in updraft, and finally elevated where the system propagates as a gravity wave and no air comes from the surface. In the current study, the MCS goes through these phases but in a different order, beginning as an

elevated system, then intensifying and developing a cold pool before finally becoming a surface-based storm followed by another intensifying period before reaching steady state. This development highlights the importance of developing a surface-based cold pool that has a large temperature deficit in comparison to the environment so that stable surface parcels can be lifted to their LFC.

Chapter 8: Conclusion

Although one previous study (Marsham et al. 2011) has analyzed the evolution of an elevated system to a surface-based one, the present study is the first to the author's knowledge to analyze an MCS from isolated convective cells through upscale growth and maturation for three and one-half hours. A comprehensive array of available fixed and mobile assets on 25-26 June during PECAN included up to 6 mobile radars, Topeka's WSR-88D, Kansas mesonet sites, mobile mesonets, and mobile sounding units. The multi-Doppler radar coverage has allowed for an unprecedented three and one-half hours of 3-D wind fields, allowing a detailed analysis of MCS kinematics and microphysics both as an elevated and a surface based system.

One of the main findings from this study is that deep, moist convective updrafts that begin as elevated above a stable boundary layer can evolve into significantly surface-based updrafts, provided that the diabatically driven cold pool becomes cooler than the surface-based nocturnal boundary layer environment. A unique aspect of this study is the ability to analyze how the diabatic cooling led to the production of the surface-based cold pool. As bulk diabatic cooling increases in the lowest 4 km, increasing work is exerted via the cold pool and the RTF-FTR circulation on initially stable parcels in the surface-based nocturnal boundary layer. It is hypothesized that this external source of work can provide mechanical forcing for updraft air parcels to be lifted to their LFC to initiate and maintain deep convection. Therefore, the dynamics that lead to a formation of a surface-based cold pool are probably critical for understanding the difference in propagation between elevated and surface-based storms. It is hypothesized that knowledge of the existence of surface-based mesoscale cold

pools along with strong convective lines and expansive trailing stratiform regions would assist forecasters in anticipating the risks of flooding and severe surface winds in nocturnal MCSs.

The ability to analyze surface-based mesoscale cold pools is also hypothesized to be important to help achieve consistently robust numerical forecasts of nocturnal MCSs. In the event that the low-level stratification in a prediction model is not correctly initialized, a poor resolution of the resultant dynamics of cold pools and a possible transition from elevated to surface-based convection and mesoscale cold pool would likely contribute to large numerical forecast errors. The results from this study could be used in a comparison study with the output from different microphysical parameterizations to determine whether the microphysics in the convection are correct. Microphysical parameterizations in prediction models are a large source of error for both nocturnal and daytime convection. Because of this, future work will focus in part on simulating the 25-26 June 2015 Kansas MCS to assess the underlying nocturnal MCS dynamical processes and gauge how realistically a deterministic, state-of-art cloud model is able to simulate this event. Validation of the simulation would be provided by the radar and Lagrangian analysis fields obtained and reported in the present study. Next, data assimilation of the available observations such as 3-D wind fields, mobile mesonets, etc may be performed to understand the dynamics of the MCS better, since models can provide information on processes that our current platforms are not capable of fully observing.

The present study has contributed a detailed analysis of the kinematic, thermal, and microphysical evolution of a nocturnal MCS. Combining MCS observations and

analyses from the present and other PECAN studies would allow additional questions to be addressed more quantitatively: (a) why did the initial isolated storms develop?; (b) what initiated and maintained the development of the bowing MCS segment?; (c) why was the MCS able to evolve to become surface-based after a period of evolution away from its initial state?; (d) how did updrafts evolve from largely elevated to significantly surface-based?; and (e) what are the relevant dynamical processes that regulate the transition from an elevated to a surface-based MCS? The present study combined with current and future studies from the PECAN field project should allow for better understanding of nocturnal MCSs and their main dynamical processes.

References

Bernstein, B. C., and R. H. Johnson, 1994: A Dual-Doppler Radar Study of an OK PRE-STORM Heat Burst Event. *Mon. Weather Rev.*, **122**, 259–273, doi:10.1175/1520-0493(1994)122<0259:ADDRSO>2.0.CO;2. http://journals.ametsoc.org/doi/abs/10.1175/1520-0493(1994)122%3C0259:ADDRSO%3E2.0.CO;2.

Biggerstaff, M. I., and R. A. Houze, 1991: Kinematic and Precipitation Structure of the 10–11 June 1985 Squall Line. *Mon. Weather Rev.*, **119**, 3066–3079, doi:10.1175/1520-0493(1991)119<3066:MVSOTJ>2.0.CO;2.

Biggerstaff, M. I., and R. A. Houze, 1993: Kinematics and Microphysics of the Transition Zone of the 10–11 June 1985 Squall Line. *J. Atmos. Sci.*, **50**, 3091–3110, doi:10.1175/1520-0469(1993)050<3091:KAMOTT>2.0.CO;2. http://dx.doi.org/10.1175/1520-0469(1993)050%3C3091:KAMOTT%3E2.0.CO;2.

Biggerstaff, M. I., and Coauthors, 2005: The Shared Mobile Atmospheric Research and Teaching Radar: A Collaboration to Enhance Research and Teaching. *Bull. Am. Meteorol. Soc.*, **86**, 1263–1274, doi:10.1175/BAMS-86-9-1263.

Billings, J. M., and M. D. Parker, 2012: Evolution and Maintenance of the 22–23 June 2003 Nocturnal Convection during BAMEX. *Weather Forecast.*, **27**, 279–300, doi:10.1175/WAF-D-11-00056.1.

Bryan, G., D. Ahijevych, C. Davis, S. Trier, and M. Weisman, 2005: Observations of Cold Pool Properties in Mesoscale Convective Systems during BAMEX. *32nd Conference on Radar Meteorology*, Albuqueque, NM, American Meteorological Society.

Bryan, G. H., and M. L. Weisman, 2006: Mechanisms for the Production of Severe Surface Winds in a Simulation of an Elevated Convective System. *23rd Conference on Severe Local Storms*, St. Louis, MO, American Meteorological Society.

Bryan, G. H., and M. D. Parker, 2010: Observations of a Squall Line and Its Near Environment Using High-Frequency Rawinsonde Launches during VORTEX2. *Mon. Weather Rev.*, **138**, 4076–4097, doi:10.1175/2010MWR3359.1. http://journals.ametsoc.org/doi/abs/10.1175/2010MWR3359.1.

Carbone, R. E., and J. D. Tuttle, 2008: Rainfall Occurrence in the U.S. Warm Season: The Diurnal Cycle. *J. Clim.*, **21**, 4132–4146, doi:10.1175/2008JCLI2275.1.

Carbone, R. E., J. W. Conway, N. A. Crook, and M. W. Moncrieff, 1990: The Generation and Propagation of a Nocturnal Squall Line. Part I: Observations and Implications for Mesoscale Predictability. *Mon. Weather Rev.*, **118**, 26–49.

Coniglio, M. C., J. Y. Hwang, and D. J. Stensrud, 2010: Environmental Factors in the Upscale Growth and Longevity of MCSs Derived from Rapid Update Cycle Analyses. *Mon. Weather Rev.*, **138**, 3514–3539, doi:10.1175/2010MWR3233.1. http://journals.ametsoc.org/doi/abs/10.1175/2010MWR3233.1.

Corfidi, S. F., 2003: Cold Pools and MCS Propagation: Forecasting the Motion of Downwind-Developing MCSs. *Weather Forecast.*, **18**, 997–1017.

——, S. J. Corfidi, and D. M. Schultz, 2008: Elevated Convection and Castellanus: Ambiguities, Significance, and Questions. *Weather Forecast.*, **23**, 1280–1303, doi:10.1175/2008WAF2222118.1.

Davis, C. A., and Coauthors, 2004: The bow echo and MCV experiment: Observations and opportunities. *Bull. Am. Meteorol. Soc.*, **85**, 1075–1093, doi:10.1175/BAMS-85-8-1075.

Engerer, N. A., D. J. Stensrud, and M. C. Coniglio, 2008: Surface Characteristics of Observed Cold Pools. *Mon. Weather Rev.*, **136**, 4839–4849, doi:10.1175/2008MWR2528.1. http://journals.ametsoc.org/doi/abs/10.1175/2008MWR2528.1.

Gale, J. J., J. W. A. Gallus, and K. A. Jungbluth, 2002: Toward Improved Prediction of Mesoscale Convective System Dissipation. *Wea. Forecast.*, **17**, 856–872, doi:10.1175/1520-0434(2002)017<0856:TIPOMC>2.0.CO;2. http://journals.ametsoc.org/doi/abs/10.1175/1520-0434(2002)017%3C0856:TIPOMC%3E2.0.CO;2.

Geerts, B., 2013: *Plains Elevated Convection at Night Experimental Design Overview*. 37 pp.

Grady, R. L., and J. Verlinde, 1997: Triple-Doppler Analysis of a Discretely Propagating, Long-Lived, High Plains Squall Line. *J. Atmos. Sci.*, **54**, 2729–2748, doi:10.1175/1520-0469(1997)054<2729:TDAOAD>2.0.CO;2. http://journals.ametsoc.org/doi/full/10.1175/1520-0469(1997)054%3C2729:TDAOAD%3E2.0.CO%3B2.

Grim, J. A., R. M. Rauber, G. M. McFarquhar, B. F. Jewett, and D. P. Jorgensen, 2009: Development and Forcing of the Rear Inflow Jet in a Rapidly Developing and Decaying Squall Line during BAMEX. *Mon. Weather Rev.*, **137**, 1206–1229, doi:10.1175/2008MWR2503.1. http://journals.ametsoc.org/doi/abs/10.1175/2008MWR2503.1.

Hildebrand, P. H., and Coauthors, 1996: The ELDORA/ASTRAIA airborne Doppler weather radar: High-resolution observations from TOGA COARE. *Bull. Am. Meteorol. Soc.*, **77**, 213–232, doi:10.1175/1520-0477(1996)077<0213:TEADWR>2.0.CO;2.

Houze, R. A., M. I. Biggerstaff, S. A. Rutledge, and B. F. Smull, 1989: Interpretation of

Doppler Weather Radar Displays of Midlatitude Mesoscale Convective Systems. *Bull. Am. Meteorol. Soc.*, **70**, 608–619, doi:10.1175/1520-0477(1989)070<0608:IODWRD>2.0.CO;2. http://journals.ametsoc.org/doi/abs/10.1175/1520-0477%281989%29070%3C0608%3AIODWRD%3E2.0.CO%3B2.

Jirak, I. L., and W. R. Cotton, 2007: Observational Analysis of the Predictability of Mesoscale Convective Systems. *Weather Forecast.*, **22**, 813–838, doi:10.1175/WAF1012.1. http://journals.ametsoc.org/doi/abs/10.1175/WAF1012.1.

Johns, R. H., and W. D. Hirt, 1987: Derechos: Widespread Convectively Induced Windstorms. *Weather Forecast.*, **2**, 32–49.

Jorgensen, D. P., and B. F. Smull, 1993: Mesovortex Circulations Seen by Airborne Doppler Radar within a Bow-Echo Mesoscale Convective System. *Bull. Am. Meteorol. Soc.*, **74**, 2146–2157.

——, M. A. LeMone, and S. B. Trier, 1997: Structure and Evolution of the 22 February 1993 TOGA COARE Squall Line: Aircraft Observations of Precipitation, Circulation, and Surface Energy Fluxes. *J. Atmos. Sci.*, **54**, 1961–1985, doi:10.1175/1520-0469(1997)054<1961:SAEOTF>2.0.CO;2. http://journals.ametsoc.org/doi/abs/10.1175/1520-0469%281997%29054%3C1961%3ASAEOTF%3E2.0.CO%3B2.

Keene, K. M., and R. S. Schumacher, 2013: The Bow and Arrow Mesoscale Convective Structure. *Mon. Weather Rev.*, **141**, 1648–1672, doi:10.1175/MWR-D-12-00172.1. http://journals.ametsoc.org/doi/abs/10.1175/MWR-D-12-00172.1.

Kessinger, C. J., P. S. Ray, and C. E. Hane, 1987: The Oklahoma Squall Line of 19 May 1977. Part I: A Multiple Doppler Analysis of Convective and Stratiform Structure. *J. Applied Meteor.*, **44**, 2840–2864.

Klimowski, B. A., 1994: Initiation and Development of Rear Inflow within the 28-29 June 1989 North Dakota Mesoconvective System. *Mon. Wea. Rev.*, **122**, 765–779.

Kuchera, E. L., and M. D. Parker, 2006: Severe Convective Wind Environments. *Wea. Forecast.*, **21**, 595–612, doi:10.1175/WAF931.1.

Lewis, S. A., M. A. LeMone, and D. P. Jorgensen, 1998: Evolution and Dynamics of a Late-Stage Squall Line That Occurred on 20 February 1993 during TOGA COARE. *Mon. Weather Rev.*, 3189–3212, doi:10.1175/1520-0493(1998)126<3189:EADOAL>2.0.CO;2.

Lin, Y., R. Pasken, and H.-W. Chang, 1992: The Structure of a Subtropical Prefrontal Convective Rainband. Part I: Mesoscale Kinematic Structure Determined from Dual-Doppler Measurements. *Mon. Weather Rev.*, **120**, 1816–1836.

Maddox, R. A., 1980: Mesoscale Convective Complexes. *Bull. Amer. Soc.*, **61**, 1374–1387.

——, 1983: Large-Scale Meteorologicl Conditions Associated with Midlatitide, Mesoscale Convective Complexes. *Mon. Weather Rev.*, **111**, 1475–1493.

Marsham, J. H., S. B. Trier, T. M. Weckwerth, and J. W. Wilson, 2011: Observations of Elevated Convection Initiation Leading to a Surface-Based Squall Line during 13 June IHOP_2002. *Mon. Weather Rev.*, **139**, 247–271, doi:10.1175/2010MWR3422.1.

McAnelly, R. L., J. E. Nachamkin, W. R. Cotton, and M. E. Nicholls, 1997: Upscale Evolution of MCSs: Doppler Radar Analysis and Analytical Investigation. *Mon. Weather Rev.*, **125**, 1083–1110, doi:10.1175/1520-0493(1997)125<1083:UEOMDR>2.0.CO;2.

Nachamkin, J. E., R. L. McAnelly, and W. R. Cotton, 1994: An Observational Analysis of a Developing Mesoscale Convective Complex. *Mon. Weather Rev.*, **122**, 1168–1188.

——, R. L. McAnelly, and W. R. Cotton, 2000: Interactions between a Developing Mesoscale Convective System and Its Environment. Part I: Observational Analysis. *Mon. Weather Rev.*, **128**, 1205–1224, doi:10.1175/1520-0493(2000)128<1225:IBADMC>2.0.CO;2. %5C%5CIBSERVER%5CID_enl%5CMonthly_weather_review%5C2000%5C128-05-1205.pdf.

O'Brien, J. J., 1970: Alternative solutions to the classical vertical velocity problem. J. Appl. Meteor., **9**, 197-203.

Parker, M. D., 2008: Response of Simulated Squall Lines to Low-Level Cooling. *J. Atmos. Sci.*, **65**, 1323–1341, doi:10.1175/2007JAS2507.1.

Protat, A., and Y. Lemaitre, 2001: Scale Interactions Involved in the Initiation , Structure , and Evolution of the 15 December 1992 MCS Observed during TOGA COARE . Part I : Synoptic-Scale Processes. *Mon. Weather Rev.*, **129**, 1757–1778, doi:10.1175/1520-0493(2001)129<1757:SIIITI>2.0.CO;2.

Rasmussen, E. N., and S. A. Rutledge, 1993: Evolution of Quasi-Two-Dimensional Squall Lines. Part I: Kinematic and Reflectivity Structure. *J. Atmos. Sci.*, **50**, 2584–2606.

Ray, P., C. Ziegler, W. Bumgarner, and R. Serafin, 1980: Single- and multiple-Doppler radar observations of tornadic storms. *Mon. Wea. Rev.*, **108**, 1607-1625.

Rotunno, R., J. B. Klemp, and M. L. Weisman, 1988: A Theory for Strong, Long-Lived Squall Lines. *J. Atmos. Sci.*, **45**, 463–485, doi:10.1175/1520-0469(1988)045<0463:ATFSLL>2.0.CO;2.

http://journals.ametsoc.org/doi/abs/10.1175/1520-0469%281988%29045%3C0463%3AATFSLL%3E2.0.CO%3B2.

Roux, F., 1988: The West African Squall Line Observed on 23 June 1981 during COPT 81: Kinematics and Thermodynamics of the Convective Region. *J. Atmos. Sci.*, **45**, 406–426, doi:10.1175/1520-0469(1988)045<0406:TWASLO>2.0.CO;2. http://journals.ametsoc.org/doi/abs/10.1175/1520-0469%281988%29045%3C0406%3ATWASLO%3E2.0.CO%3B2.

Rutledge, S. a., R. a. Houze Jr, M. I. Biggerstaff, and T. Matejka, 1988: The Oklahoma-Kansas Mesoscale Convective System of 10-11 June 1985: Precipitation Structure and Single-Doppler Rader Analysis. *Mon. Weather Rev.*, **116**, 1409–1430, doi:10.1175/1520-0493(1988)116<1409:TOMCSO>2.0.CO;2.

Rutledge, S. A., and R. A. Houze, 1987: A Diagnostic Modelling Study of the Trailing Stratiform Region of a Midlatitude Squall Line. *J. Atmos. Sci.*, **44**, 2640–2656, doi:10.1175/1520-0469(1987)044<2640:ADMSOT>2.0.CO;2. http://journals.ametsoc.org/doi/abs/10.1175/1520-0469%281987%29044%3C2640%3AADMSOT%3E2.0.CO%3B2.

Schmidt, J. M., and W. R. Cotton, 1989: A High Plains Squall Line Associated with Severe Surface Winds. *J. Atmos. Sci.*, **46**, 281–302, doi:10.1175/1520-0469(1989)046<0281:AHPSLA>2.0.CO;2. http://journals.ametsoc.org/doi/abs/10.1175/1520-0469(1989)046%3C0281:AHPSLA%3E2.0.CO;2.

——, and ——, 1990: Interactions between Upper and Lower Tropospheric Gravity Waves on Squall Line Structure and Maintenance. *J. Atmos. Sci.*, **47**, 1205–1222.

Schumacher, R. S., 2015: Sensitivity of Precipitation Accumulation in Elevated Convective Systems to Small Changes in Low-Level Moisture. *J. Atmos. Sci.*, **72**, 2507–2524, doi:10.1175/JAS-D-14-0389.1. http://journals.ametsoc.org/doi/10.1175/JAS-D-14-0389.1.

Schuur, T. J., and S. A. Rutledge, 2000: Electrification of Stratiform Regions in Mesoscale Convective Systems. Part I: An Observational Comparison of Symmetric and Asymmetric MCSs. *J. Atmos. Sci.*, **57**, 1961–1982, doi:10.1175/1520-0469(2000)057<1961:EOSRIM>2.0.CO;2. http://dx.doi.org/10.1175/1520-0469(2000)057%3C1961:EOSRIM%3E2.0.CO%5Cnhttp://2%5Cnhttp://journals.ametsoc.org/doi/abs/10.1175/1520-0469%282000%29057%3C1961%3AEOSRIM%3E2.0.CO%3B2.

Scott, J. D., and S. A. Rutledge, 1995: Doppler Radar Observations of an Asymmetric Mesoscale Convective System and Associated Vortex Couplet. *Mon. Weather Rev.*, **123**, 3437–3457, doi:10.1175/1520-0493(1995)123<3437:DROOAA>2.0.CO;2. http://journals.ametsoc.org/doi/abs/10.1175/1520-

0493(1995)123%3C3437:DROOAA%3E2.0.CO;2.

Smull, B. F., and R. A. Houze, 1985: A Midlatitude Squall Line with a Trailing Region of Stratiform Rain: Radar and Satellite Observations. *Mon. Weather Rev.*, **113**, 117–133.

Smull, B. F., and R. A. Houze, 1987a: Dual Doppler Radar Analysis of a Midlatitude Squall Line with a Trailing Region of Statiform Rain. *J. Atmopsheric Sci.*, **44**, 2128–2148, doi:10.1175/1520-0469(1987)044<2128:DDRAOA>2.0.CO;2.

——, and ——, 1987b: Rear Inflow in Squall Lines with Trailing Stratiform Precipitation. *Mon. Weather Rev.*, **115**, 2869–2889, doi:10.1175/1520-0493(1987)115<2869:RIISLW>2.0.CO;2. http://journals.ametsoc.org/doi/abs/10.1175/1520-0493(1987)115%3C2869:RIISLW%3E2.0.CO;2.

——, and J. a. Augustine, 1993: Multiscale Analysis of a Mature Mesoscale Convective Complex. *Mon. Weather Rev.*, **121**, 103–132, doi:10.1175/1520-0493(1993)121<0103:MAOAMM>2.0.CO;2.

Storm, B. A., M. D. Parker, and D. P. Jorgensen, 2007: A Convective Line with Leading Stratiform Precipitation from BAMEX. *Mon. Weather Rev.*, **135**, 1769–1785, doi:10.1175/MWR3392.1. http://journals.ametsoc.org/doi/abs/10.1175/MWR3392.1.

Straka, J. M., E. N. Rasmussen, and S. E. Fredrickson, 1996: A Mobile Mesonet for Finescale Meteorological Observations. *J. Atmos. Ocean. Technol.*, **13**, 921–936.

Trier, S. B., and D. B. Parsons, 1993: Evolution of Environmental Conditions Preceding the Development of a Nocturnal Mesoscale Convective Complex. *Mon. Weather Rev.*, **121**, 1078–1098.

Trier, S. B., J. H. Marsham, C. A. Davis, and D. A. Ahijevych, 2011: Numerical Simulations of the Postsunrise Reorganization of a Nocturnal Mesoscale Convective System during 13 June IHOP_2002. *J. Atmos. Sci.*, **68**, 2988–3011, doi:10.1175/JAS-D-11-0112.1. http://dx.doi.org/10.1175/JAS-D-11-0112.1.

Wakimoto, R. M., H. V. Murphey, C. A. Davis, and N. T. Atkins, 2006a: High Winds Generated by Bow Echoes. Part II: The Relationship between the Mesovortices and Damaging Straight-Line Winds. *Mon. Weather Rev.*, **134**, 2813–2829, doi:10.1175/MWR3216.1. http://journals.ametsoc.org/doi/abs/10.1175/MWR3216.1.

——, ——, A. Nester, D. P. Jorgensen, and N. T. Atkins, 2006b: High Winds Generated by Bow Echoes. Part I: Overview of the Omaha Bow Echo 5 July 2003 Storm during BAMEX. *Mon. Weather Rev.*, **134**, 2793–2812, doi:10.1175/MWR3215.1. http://journals.ametsoc.org/doi/abs/10.1175/MWR3215.1.

Wallace, J. M., 1975: Diurnal Variations in Precipitation and Thunderstorm Frequency over the Conterminous Unites States. *Mon. Weather Rev.*, **103**, 406–419.

Wang, J.-J., and L. D. Carey, 2005: The Development and Structure of an Oceanic Squall-Line System during the South China Sea Monsoon Experiment. *Mon. Weather Rev.*, **133**, 1544–1561, doi:10.1175/MWR2933.1.

Wang, T., Y. Lin, H. Shen, and R. Pasken, 1990: Characteristics of a Subtropical Squall Line Determined from TAMEX Dual-Doppler Data. Part I: Kinematic Structure. *J. Atmos. Sci.*, **47**, 2357–2381. http://cat.inist.fr/?aModele=afficheN&cpsidt=19850343.

Watson, A. I., J. Meitín, and J. B. Cunning, 1988: Evolution of the Kinematic Structure and Precipitation Characteristics of a Mesoscale Convective System on 20,May 1979. *Mon. Weather Rev.*, **116**, 1555–1567, doi:10.1175/1520-0493(1988)116<1555:EOTKSA>2.0.CO;2. http://journals.ametsoc.org/doi/abs/10.1175/1520-0493%281988%29116%3C1555%3AEOTKSA%3E2.0.CO%3B2.

Wetzel, P. J., W. R. Cotton, and R. L. McAnelly, 1983: A Long-Lived Mesoscale Convective Complex. Part II: Evolution and Structure of the Mature Complex. *Mon. Weather Rev.*, **111**, 1919–1937.

Wilson, J. W., and R. D. Roberts, 2006: Summary of Convective Storm Initiation and Evolution during IHOP: Observational and Modeling Perspective. *Mon. Weather Rev.*, **134**, 23–47, doi:10.1175/MWR3069.1. http://journals.ametsoc.org/doi/abs/10.1175/MWR3069.1.

Wurman, J., J. Straka, E. Rasmussen, M. Randall, and A. Zahrai, 1997: Design and deployment of a portable, pencil-beam, pulsed, 3-cm Doppler radar. *J. Atmos. Ocean. Technol.*, **14**, 1502–1512, doi:10.1175/1520-0426(1997)014<1502:DADOAP>2.0.CO;2.

Yu, C.-K., B. J.-D. Jou, B. F. Smull, C.-K. Yu, B. J.-D. Jou, and B. F. Smull, 1999: Formative Stage of a Long-Lived Mesoscale Vortex Observed by Airborne Doppler Radar. *Mon. Weather Rev.*, **127**, 838–857, doi:10.1175/1520-0493(1999)127<0838:FSOALL>2.0.CO;2. http://journals.ametsoc.org/doi/abs/10.1175/1520-0493%281999%29127%3C0838%3AFSOALL%3E2.0.CO%3B2.

Zheng, Y., Q. Xu, and D. J. Stensrud, 1995: A Numerical Simulation of the 7 May 1985 Mesoscale Convective System. *Mon. Weather Rev.*, **123**, 1781–1799.

Ziegler, C., P. Ray, and N. Knight, 1983: Hail growth in an Oklahoma multicell storm. *J. Atmos. Sci.*, **40**, 1768-1791.

Ziegler, C., 1985: Retrieval of thermal and microphysical variables in observed convective storms. Part I: Model development and preliminary testing. *J. Atmos.*

Sci., **42**, 1487-1509.

Ziegler, C., 1988: Retrieval of thermal and microphysical variables in observed convective storms. Part II: Sensitivity of cloud processes to variation of the microphysical parameterization. *J. Atmos. Sci.*, **45**, 1072-1090.

Ziegler, C., D. MacGorman, J. Dye, and P. Ray, 1991: A model evaluation of non-inductive graupel-ice charging in the early electrification of a mountain thunderstorm. J. Geophys. Res., 96, 12,833-12,855

Ziegler, C., 1999: Issues in forecasting Mesoscale Convective Systems: An observational and modeling perspective, Chapter 32, **Vol. 2**, *STORMS*, R. Pielke, Jr. and R. Pielke, Sr, Eds., Routledge Press, London, 26-42.

Ziegler, C. L., D. Kennedy, and E. N. Rasmussen, 2004: A Wireless Network for Collection and Synthesis of Mobile Mesoscale Weather Observations. *J. Atmos. Ocean. Technol.*, **21**, 1659–1669.

Ziegler, C., 2013a: A diabatic Lagrangian technique for the analysis of convective storms. Part I: Description and validation via an observing system simulation experiment. *J. Atmos. Ocean. Tech.*, **30**, 2248-2265, doi:10.1175/JTECH-D-12-00194.1.

Ziegler, C., 2013b: A diabatic Lagrangian technique for the analysis of convective storms. Part II: Application to a radar-observed storm. *J. Atmos. Ocean. Tech.*, **30**, 2266-2280, doi:10.1175/JTECH-D-13-00036.1.

Appendix A: Tables

Table 1. List of all radar analysis times with radars contributing.

Time	# of Radars in volume	Name of Radars	Comments
0300 UTC	5	SR1, SR2, NOXP, Dow7, KTWX	Isolated convective cells in NW corner of domain.
0310 UTC	5	SR1, SR2, NOXP, Dow7, KTWX	
0320 UTC	5	SR1, SR2, NOXP, Dow7, KTWX	
0330 UTC	5	SR1, SR2, NOXP, Dow7, KTWX	
0340 UTC	5	SR1, SR2, NOXP, Dow7, KTWX	
0345 UTC	4	SR1, SR2, NOXP, KTWX	
0350 UTC	5	SR1, SR2, NOXP, Dow7, KTWX	
0355 UTC	4	SR1, SR2, NOXP, KTWX	
0400 UTC	5	SR1, SR2, NOXP, Dow7, KTWX	Cells have converged into linear MCS.
0405 UTC	4	SR1, SR2, NOXP, KTWX	
0410 UTC	5	SR1, SR2, NOXP, Dow7, KTWX	
0415 UTC	4	SR1, SR2, NOXP, KTWX	
0420 UTC	5	SR1, SR2, NOXP, Dow7, KTWX	
0425 UTC	4	SR1, SR2, NOXP, KTWX	
0430 UTC	5	SR1, SR2, NOXP, Dow7,	

		KTWX	
0435 UTC	4	SR1, SR2, NOXP, KTWX	
0440 UTC	5	SR1, SR2, NOXP, Dow7, KTWX	Dow7 switches scanning strategy to complete volume every 5 minutes. Surging outflow feature begins.
0445 UTC	5	SR1, SR2, NOXP, Dow7, KTWX	
0450 UTC	5	SR1, SR2, NOXP, Dow7, KTWX	
0455 UTC	5	SR1, SR2, NOXP, Dow7, KTWX	
0500 UTC	7	SR1, SR2, NOXP, Dow7, Dow6, Dow8, KTWX	First volume with all 7 radars. Bowing MCS.
0505 UTC	7	SR1, SR2, NOXP, Dow7, Dow6, Dow8, KTWX	
0510 UTC	7	SR1, SR2, NOXP, Dow7, Dow6, Dow8, KTWX	
0515 UTC	7	SR1, SR2, NOXP, Dow7, Dow6, Dow8, KTWX	
0520 UTC	7	SR1, SR2, NOXP, Dow7, Dow6, Dow8, KTWX	Last volume with all 7 radars. Wind report in this analysis.
0525 UTC	6	SR1, SR2, NOXP, Dow7, Dow6, KTWX	
0530 UTC	6	SR1, SR2,	

		NOXP, Dow7, Dow6, KTWX
0535 UTC	6	SR1, SR2, NOXP, Dow7, Dow6, KTWX
0540 UTC	6	SR1, SR2, NOXP, Dow7, Dow6, KTWX
0545 UTC	6	SR1, SR2, NOXP, Dow7, Dow6, KTWX
0550 UTC	6	SR1, SR2, NOXP, Dow7, Dow6, KTWX
0555 UTC	6	SR1, SR2, NOXP, Dow7, Dow6, KTWX
0600 UTC	6	SR1, SR2, NOXP, Dow7, Dow6, KTWX
0605 UTC	6	SR1, SR2, NOXP, Dow7, Dow6, KTWX
0610 UTC	6	SR1, SR2, NOXP, Dow7, Dow6, KTWX
0615 UTC	6	SR1, SR2, NOXP, Dow7, Dow6, KTWX
0620 UTC	5	SR1, SR2, NOXP, Dow6, KTWX
0625 UTC	4	SR1, SR2, NOXP, KTWX

Appendix B: Figures

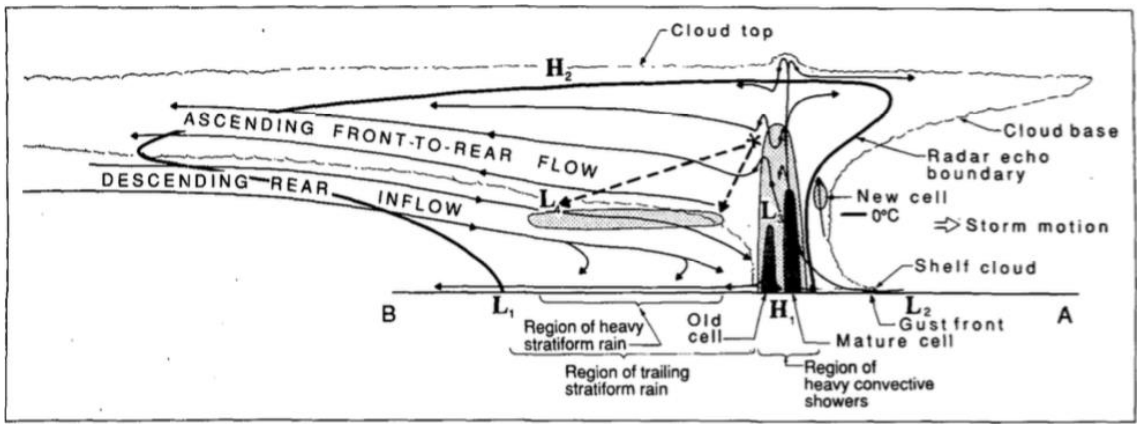

Figure 1. MCS conceptual model from Houze et al. 1989. The solid black line denotes the area of the radar echo with darker shading indicating higher reflectivity values at the melting level and in convective cores. Thin black arrows denote streamlines in the MCS with flow going up into the main convective cells and diverging at the storm top to create the anvil. The ascending FTR flow and descending rear inflow is labeled.

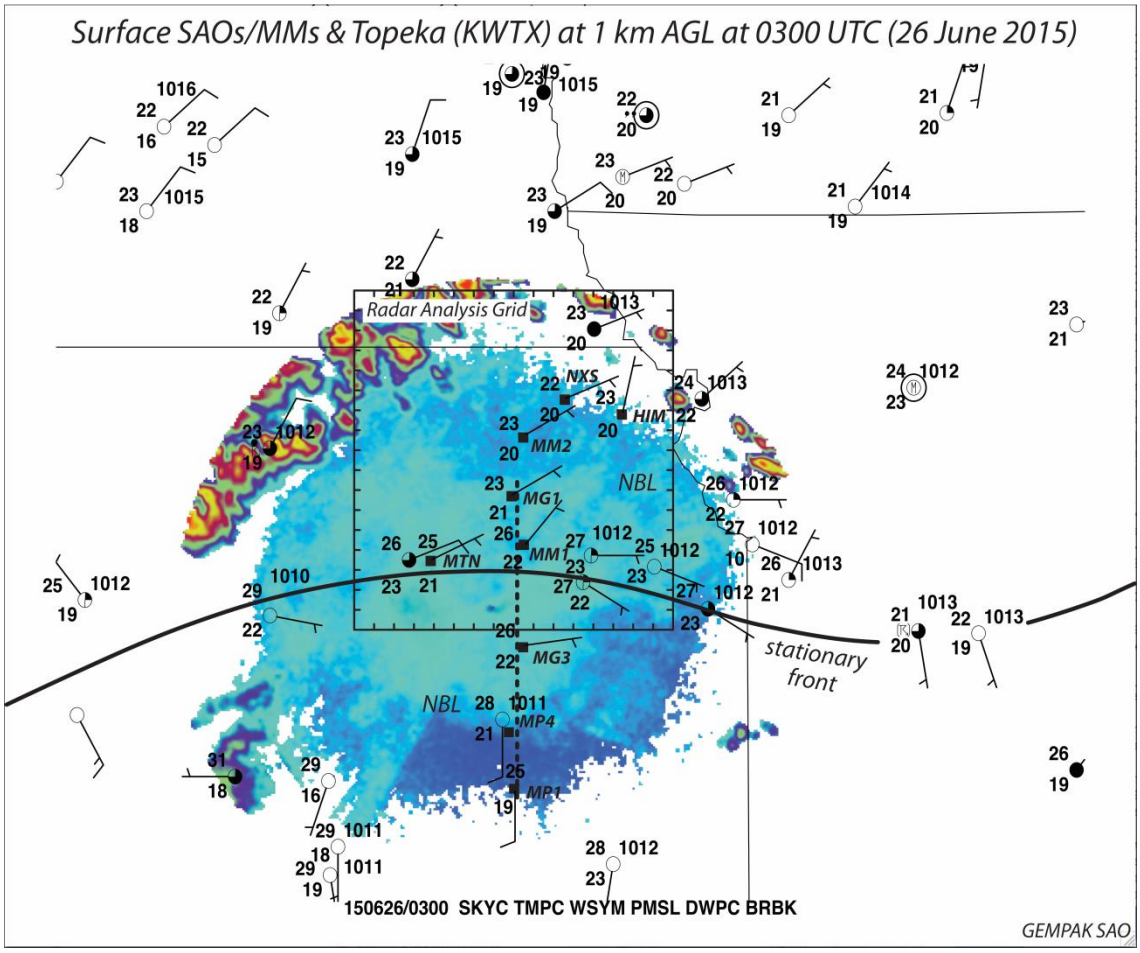

Figure 2. 0300 UTC KTWX reflectivity is overlaid with 0300 UTC surface SAOs and mobile mesonet observations. The radar analysis domain is indicated by the black box. The stationary front is a solid black line that crosses over the southern portion of the radar analysis domain. The black dashed line indicates the location of the sounding analysis cross section shown in figure 4.

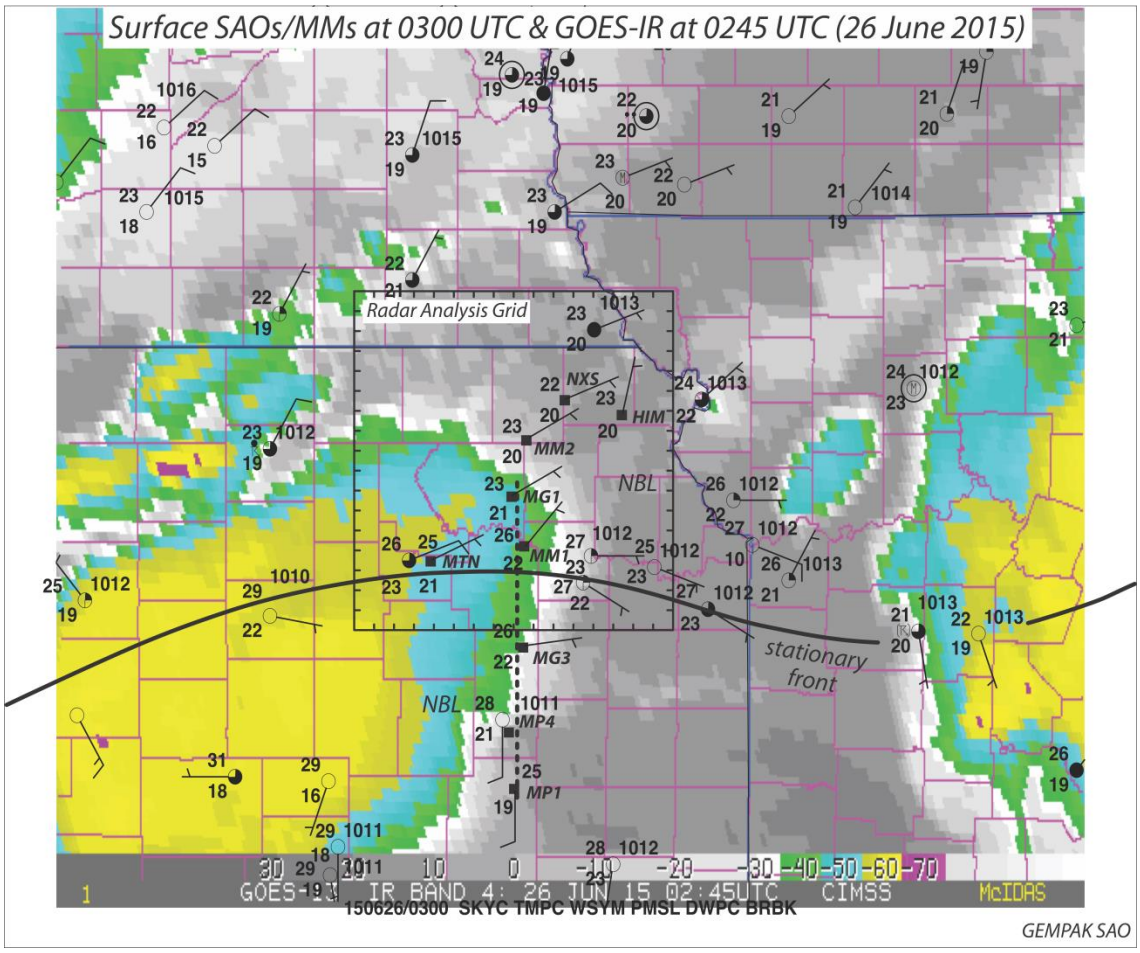

Figure 3. 0245 UTC GOES-IR image is overlaid with 0300 UTC surface SAOs and mobile mesonet observations. The radar analysis domain is indicated by the black box. The stationary front is a solid black line that crosses over the southern portion of the radar analysis domain. The black dashed line indicates the location of the sounding analysis cross section shown in figure 4.

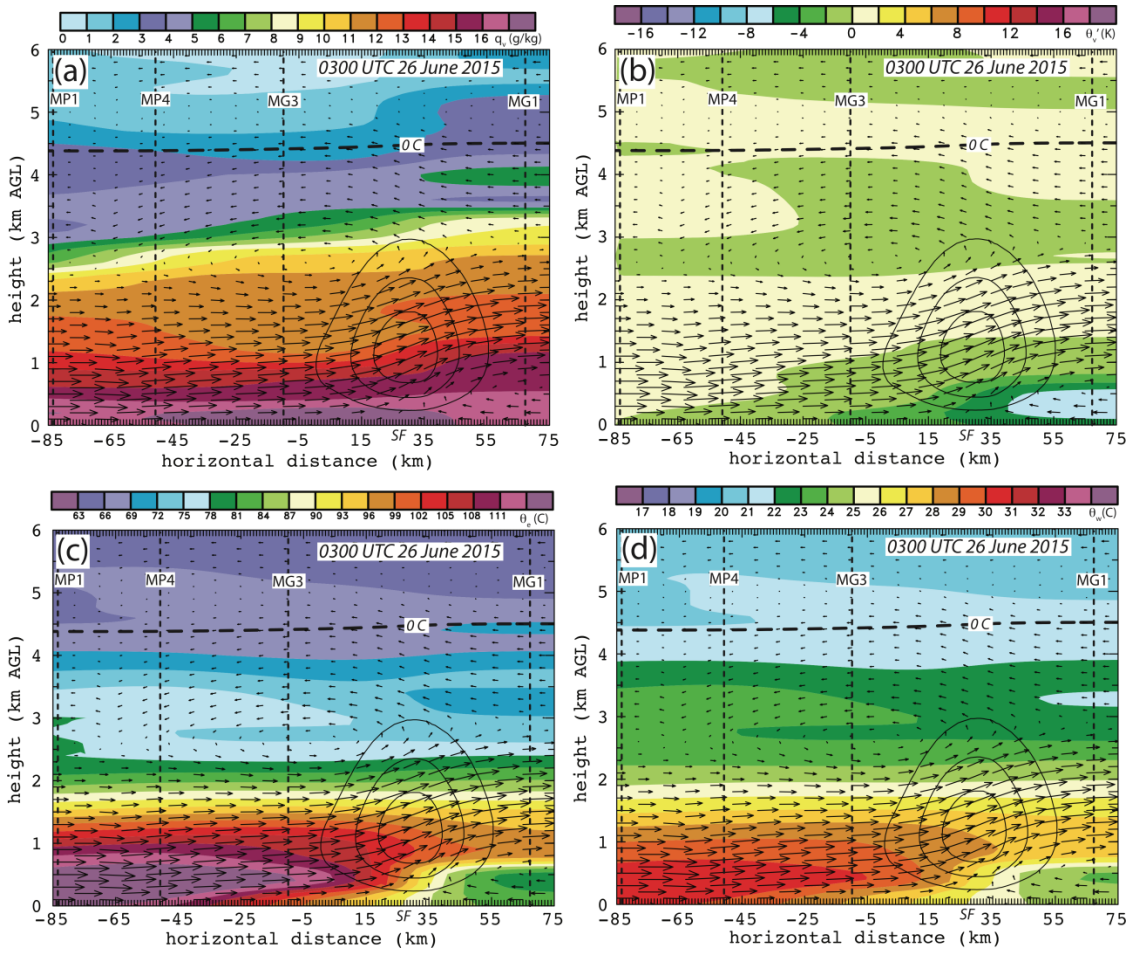

Figure 4. North-south cross section through the stationary front at 0300 UTC using 4 soundings from MG1, MG3, MP4, and MP1 indicated by black dashed lines and labeled with the respective sounding unit. All panels have solid black contours every 0.05 m/s to show weak ascent due to the front, labeled "SF". The four panels show a) water vapor mixing ratio b) theta-v' c) theta e d) theta w.

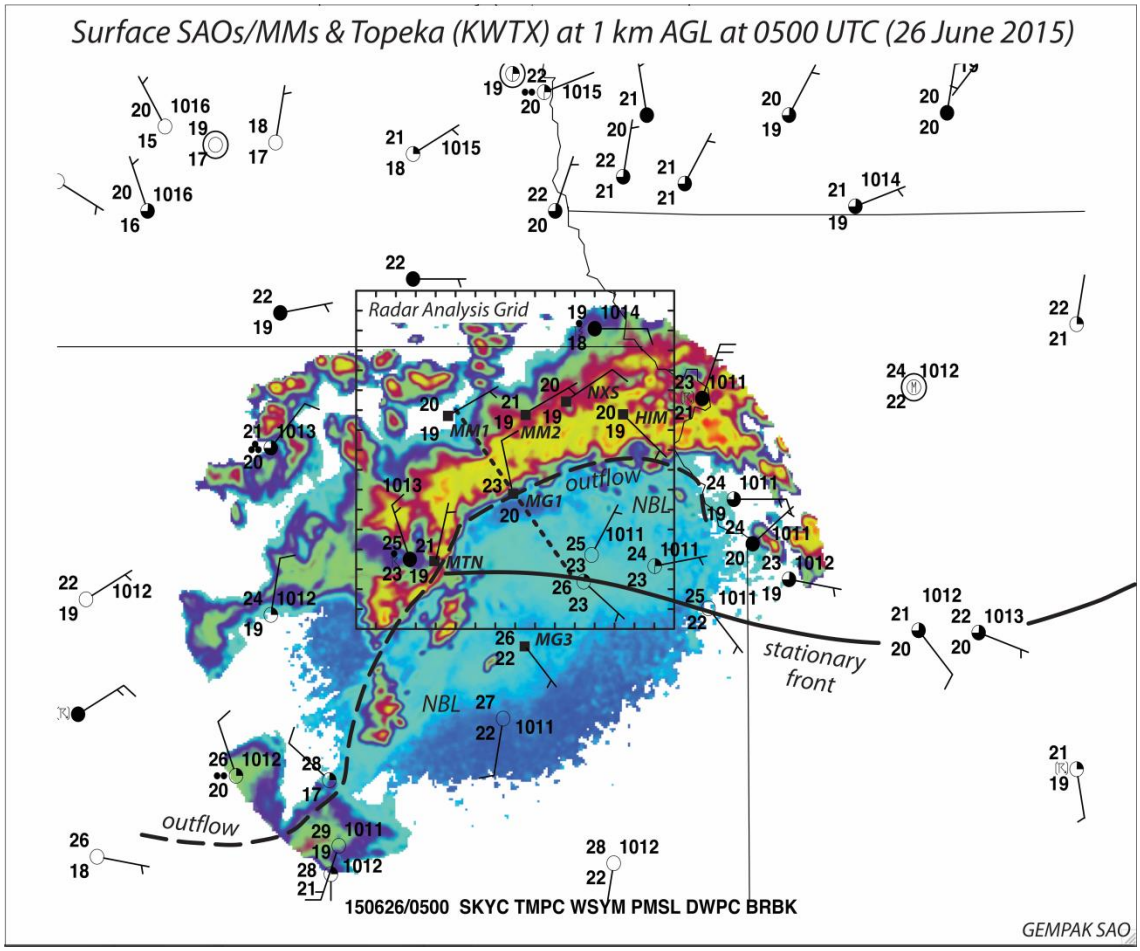

Figure 5. 0500 UTC KTWX reflectivity is overlaid with 0500 UTC surface SAOs and mobile mesonet observations. The radar analysis domain is indicated by the black box. The stationary front is a solid black line that crosses over the southern portion of the radar analysis domain and the long black dash line indicates the location of the outflow boundary. The short black dashed line indicates the location of the sounding analysis cross section shown in figure 54.

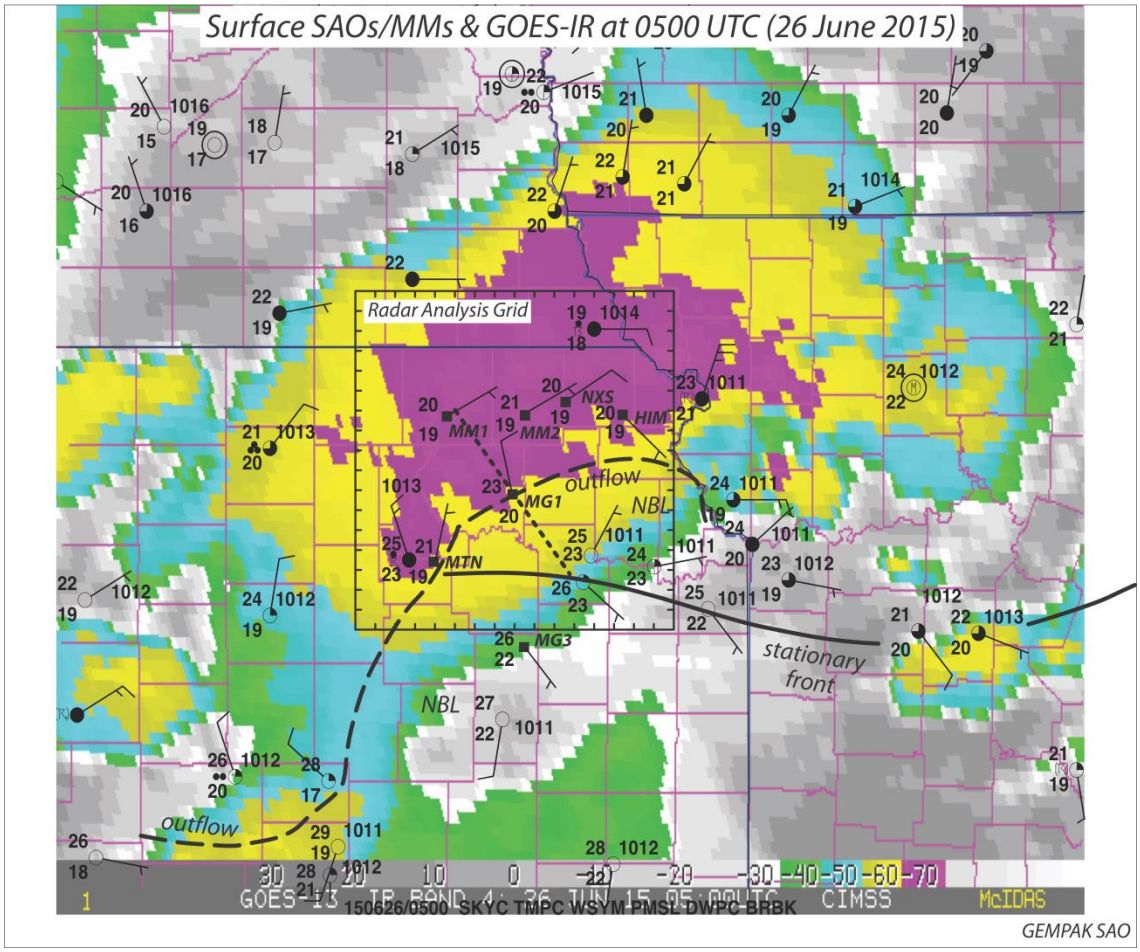

Figure 6. 0500 UTC GOES-IR image is overlaid with 0500 UTC surface SAOs and mobile mesonet observations. The radar analysis domain is indicated by the black box. The stationary front is a solid black line that crosses over the southern portion of the radar analysis domain and the long black dash line indicates the location of the outflow boundary. The short black dashed line indicates the location of the sounding analysis cross section shown in figure 54.

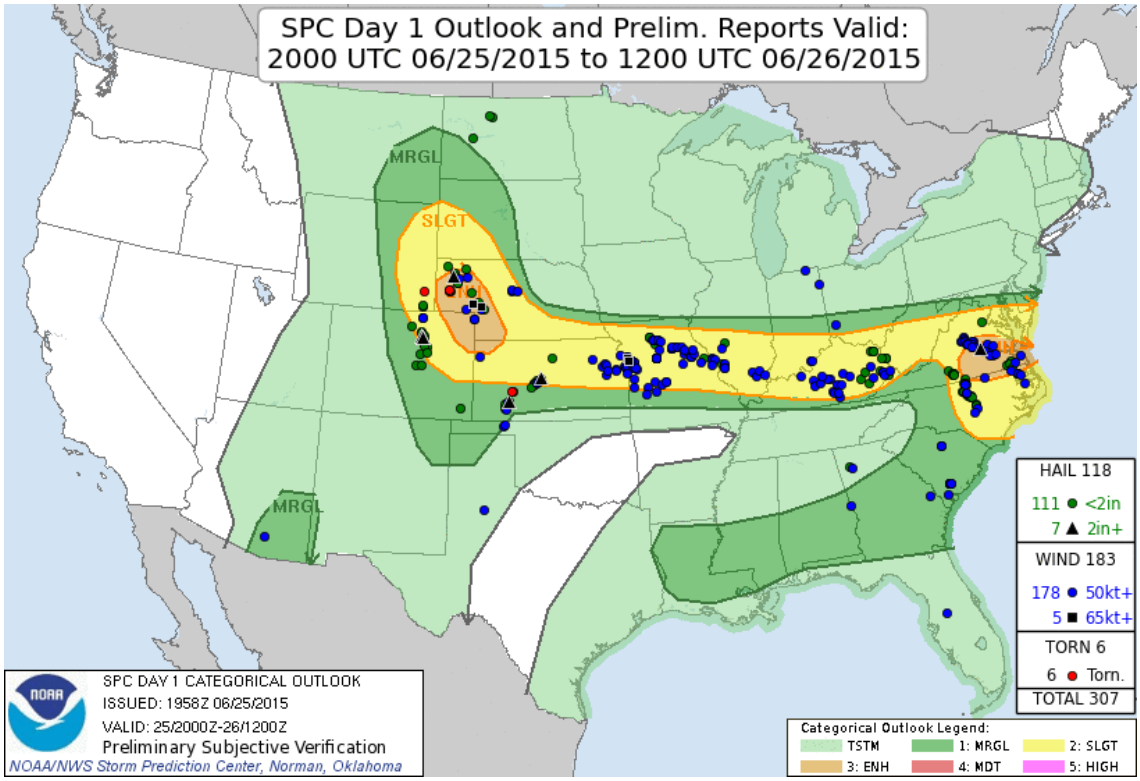

Figure 7. SPC storm reports of tornadoes, wind, and hail overlaid with day 1 convective outlook. The severe wind reports associated with the overnight Kansas MCS are clustered in eastern Kansas and western Missouri in a slight risk region. This MCS only produced wind reports with no other forms of severe weather noted.

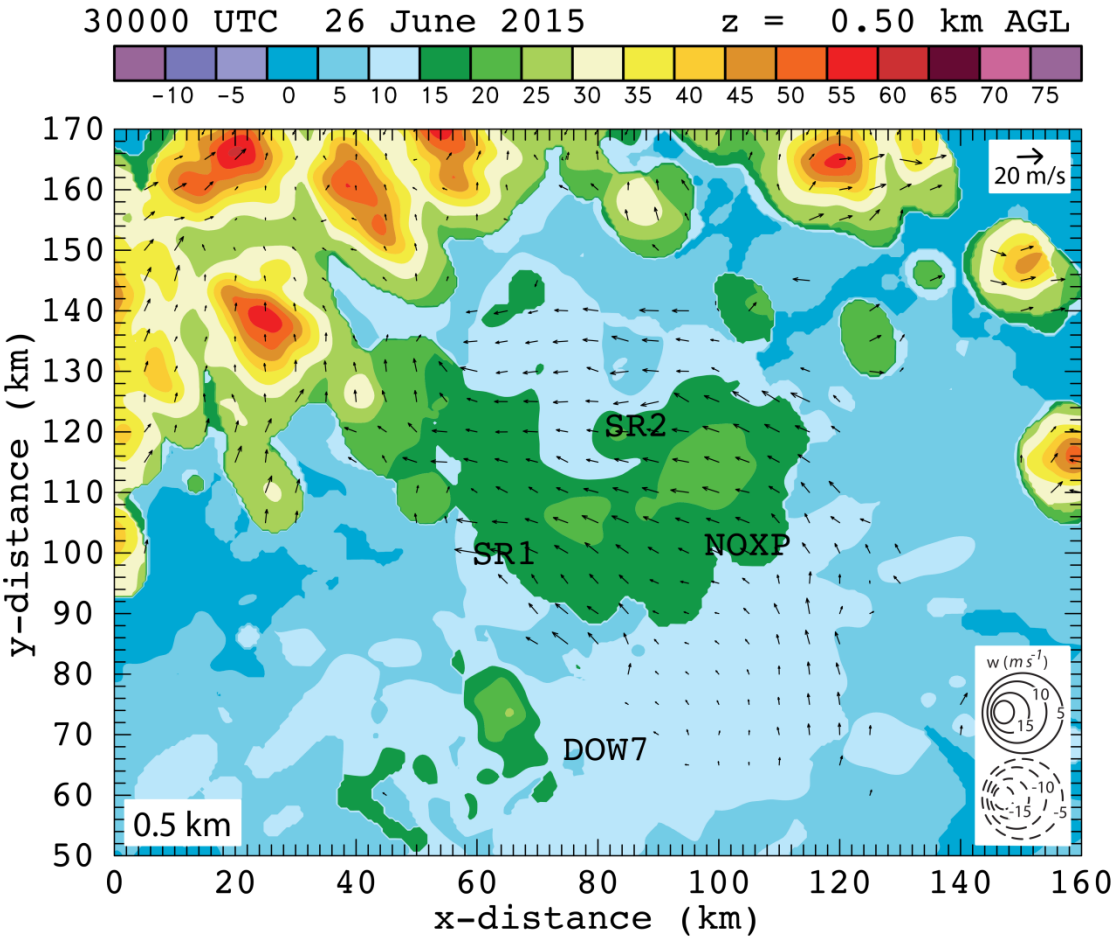

Figure 8. 0.5 km level radar analysis with horizontal wind vectors plotted and dBZ values color-filled at 0300 UTC in the northern portion of the radar analysis domain. 5 radars contributed to this analysis: SR1, SR2, NOXP, Dow7, and KTWX. All radar locations are labeled with the exception of KTWX since it was further south in the domain. Scaling factor for wind vectors and contour intervals are located in the upper right corner and lower right corner, respectively.

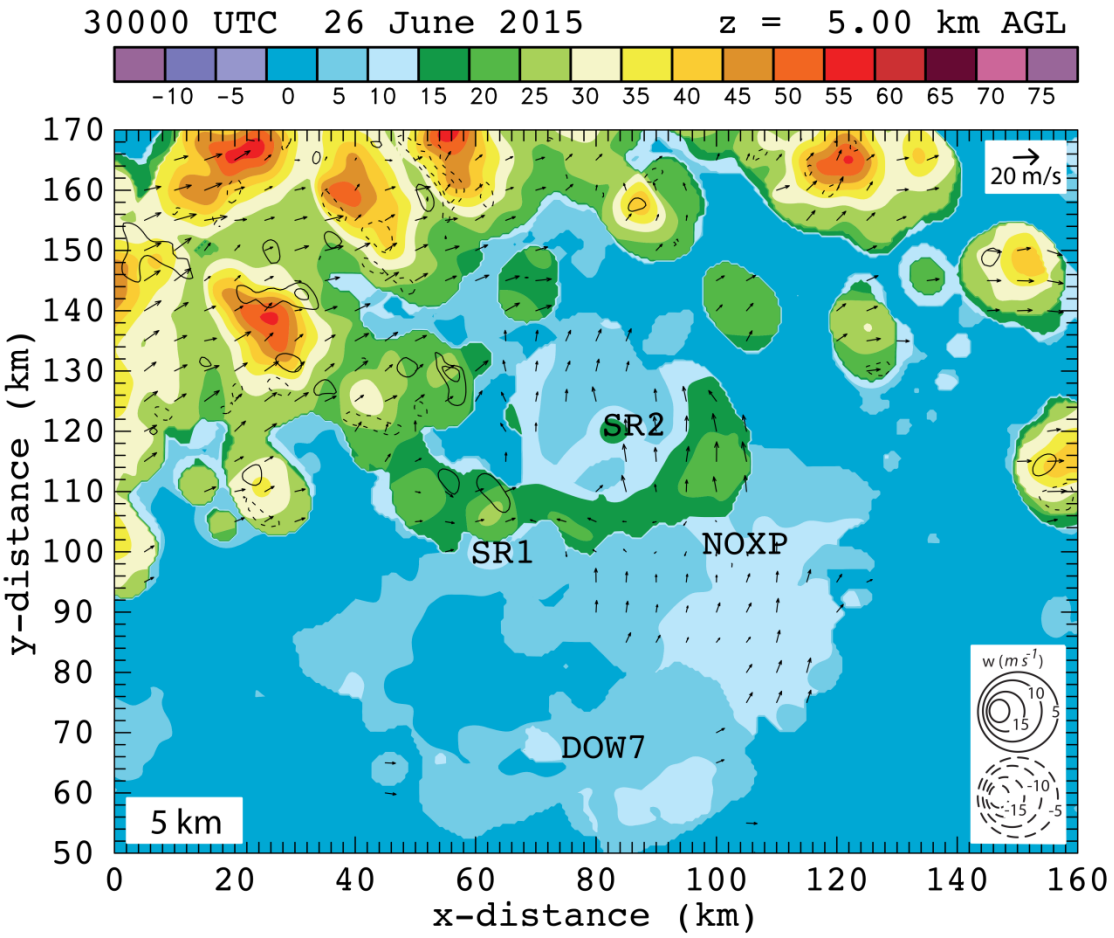

Figure 9. 5 km level radar analysis with horizontal wind vectors plotted and dBZ values color-filled at 0300 UTC in the northern portion of the radar analysis domain. 5 radars contributed to this analysis: SR1, SR2, NOXP, Dow7, and KTWX. All radar locations are labeled with the exception of KTWX since it was further south in the domain. Scaling factor for wind vectors and contour intervals are located in the upper right corner and lower right corner, respectively.

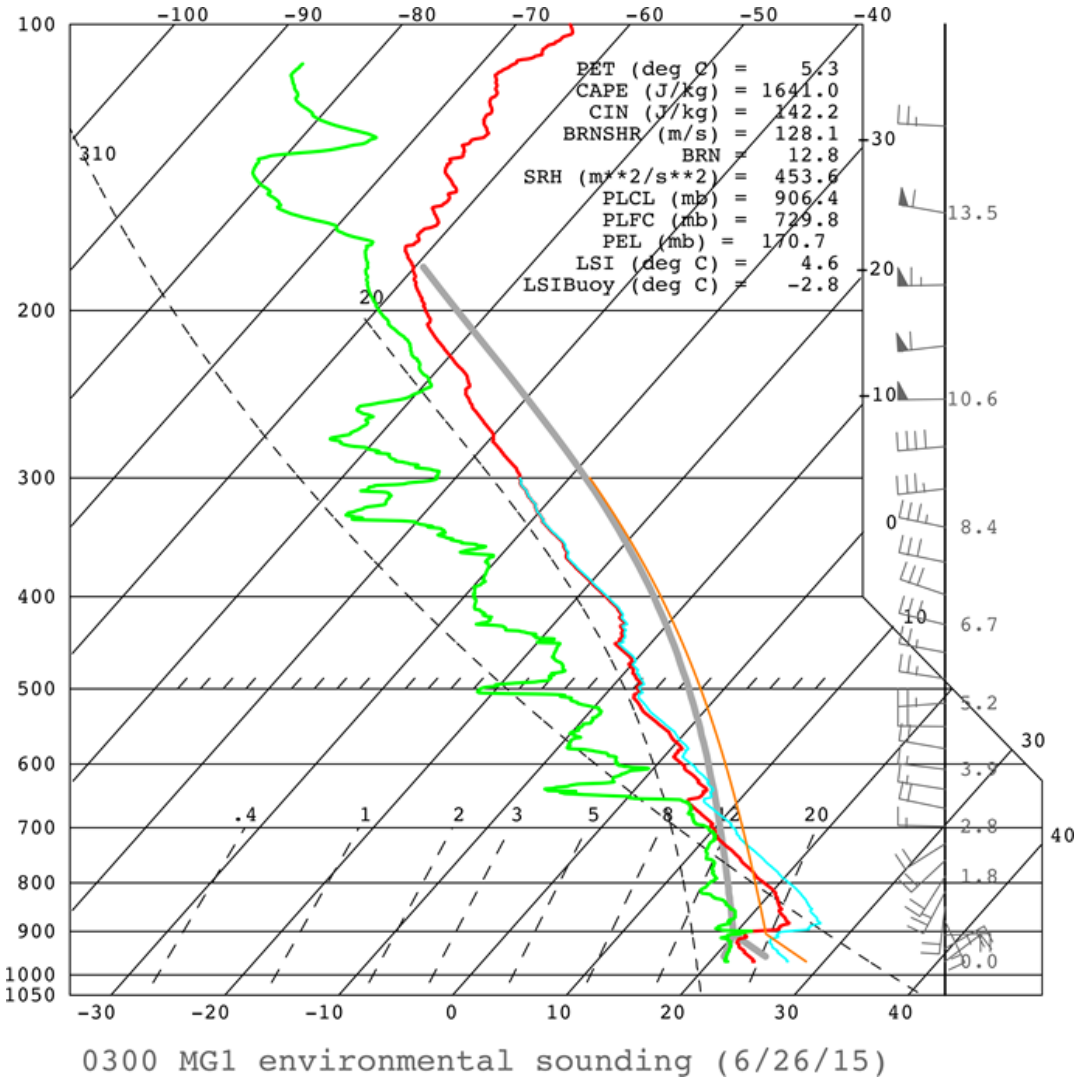

Figure 10. 0300 UTC environmental sounding from MG1 which was co-located with Dow7. Red line indicates temperature, green line indicates dewpoint, and the gray line is a parcel trace if air was lifted from the surface. Calculations for quantities determined by parcel trace such as CAPE, CIN, etc are shown in the upper right corner. Wind vectors are shown to the right of the temperature with a half bar for 5 knots, a full bar for 10 knots, and a triangle for 50 knots.

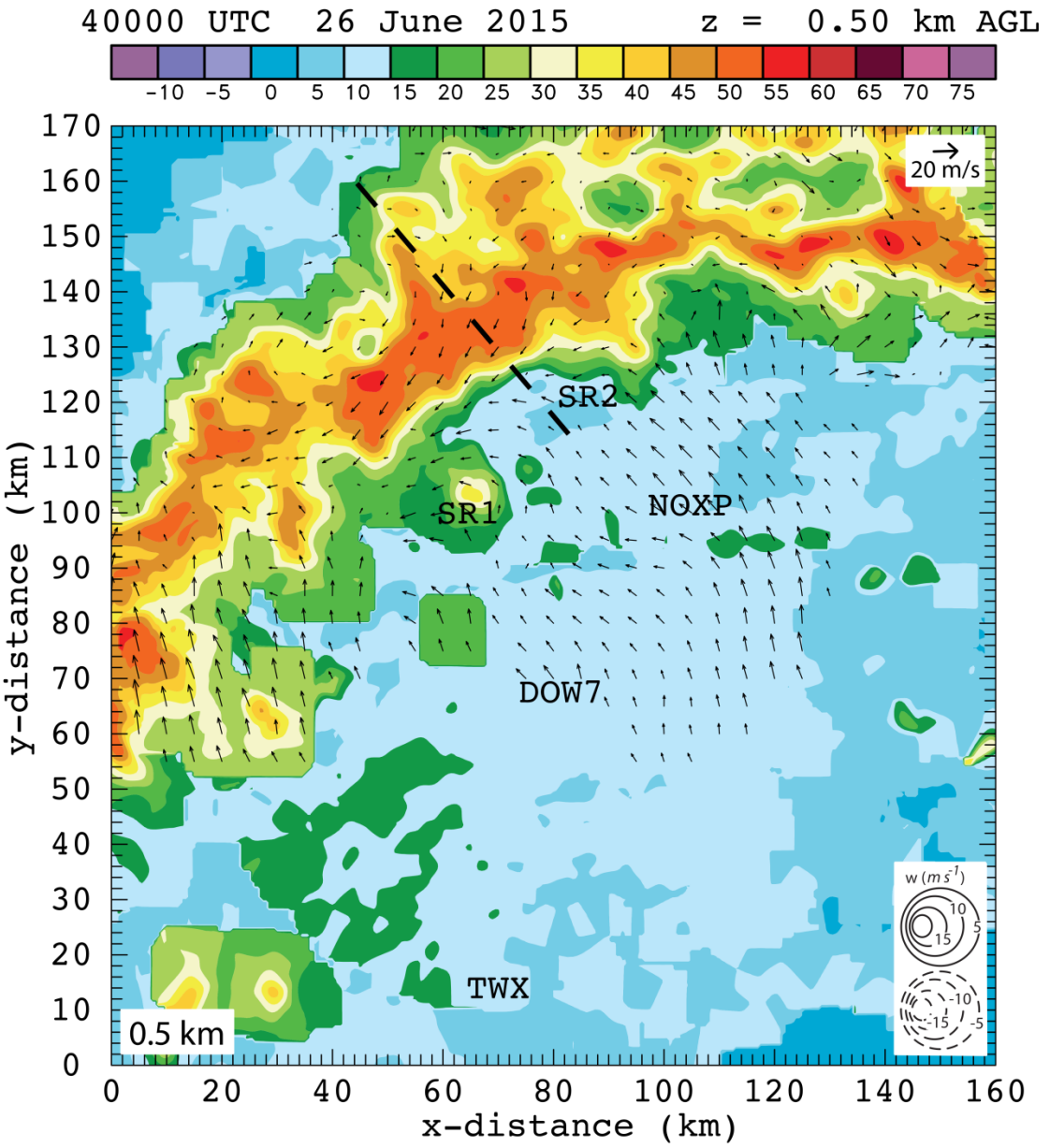

Figure 11. 0.5 km level radar analysis with horizontal wind vectors plotted and dBZ values color-filled at 0400 UTC. The dashed black line indicates the location of the vertical cross section shown in figure 13. 5 radars contributed to this analysis: SR1, SR2, NOXP, Dow7, and KTWX. All radar locations are labeled. Scaling factor for wind vectors and contour intervals are located in the upper right corner and lower right corner, respectively.

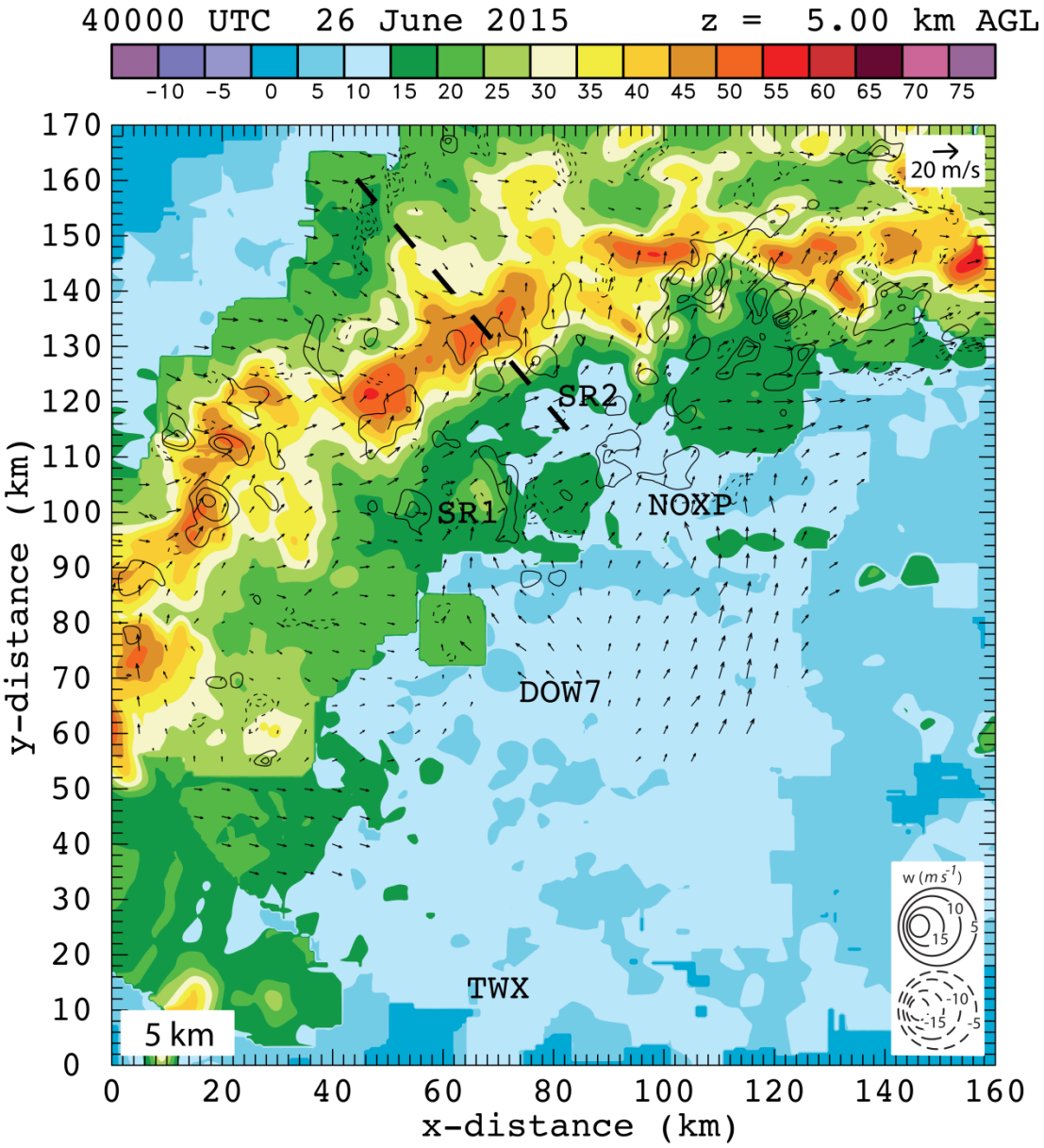

Figure 12. 5 km level radar analysis with horizontal wind vectors plotted and dBZ values color-filled at 0400 UTC. The dashed black line indicates the location of the vertical cross section shown in figure 13. 5 radars contributed to this analysis: SR1, SR2, NOXP, Dow7, and KTWX. All radar locations are labeled. Scaling factor for wind vectors and contour intervals are located in the upper right corner and lower right corner, respectively.

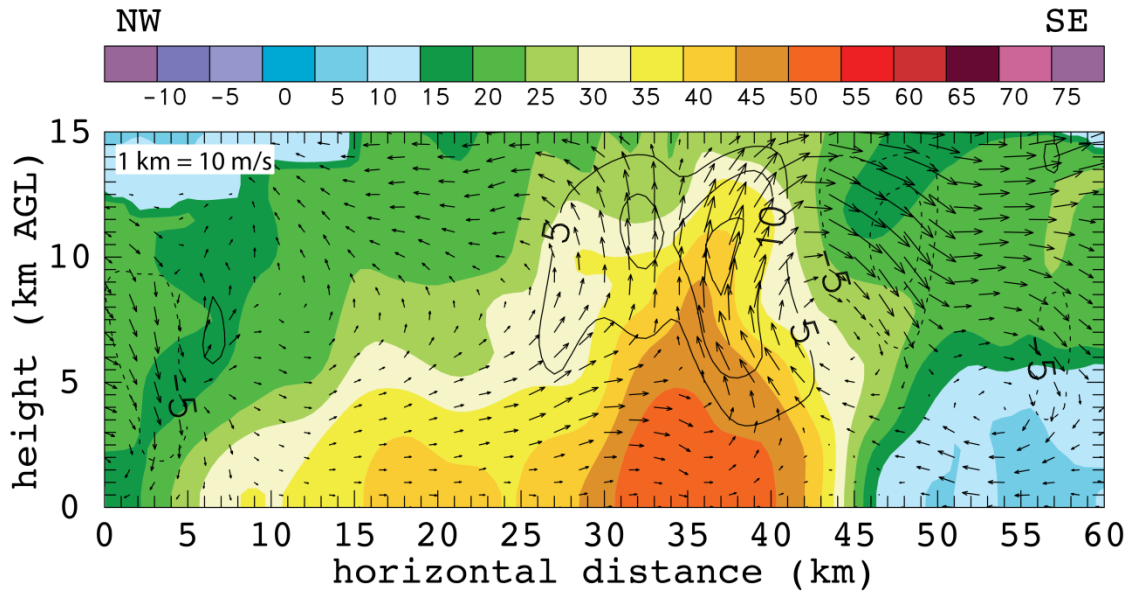

Figure 13. Vertical cross section through radar analysis at 0400 UTC indicated by the dashed black line in figures 11 and 12. dBZ values color-filled and wind vectors plotted with black contours every 5 m/s, solid lines indicated positive w and dashed lines indicate negative w. 5 radars contributed to this analysis: SR1, SR2, NOXP, Dow7, and KTWX. Scaling factor for wind vectors is located in the upper left corner.

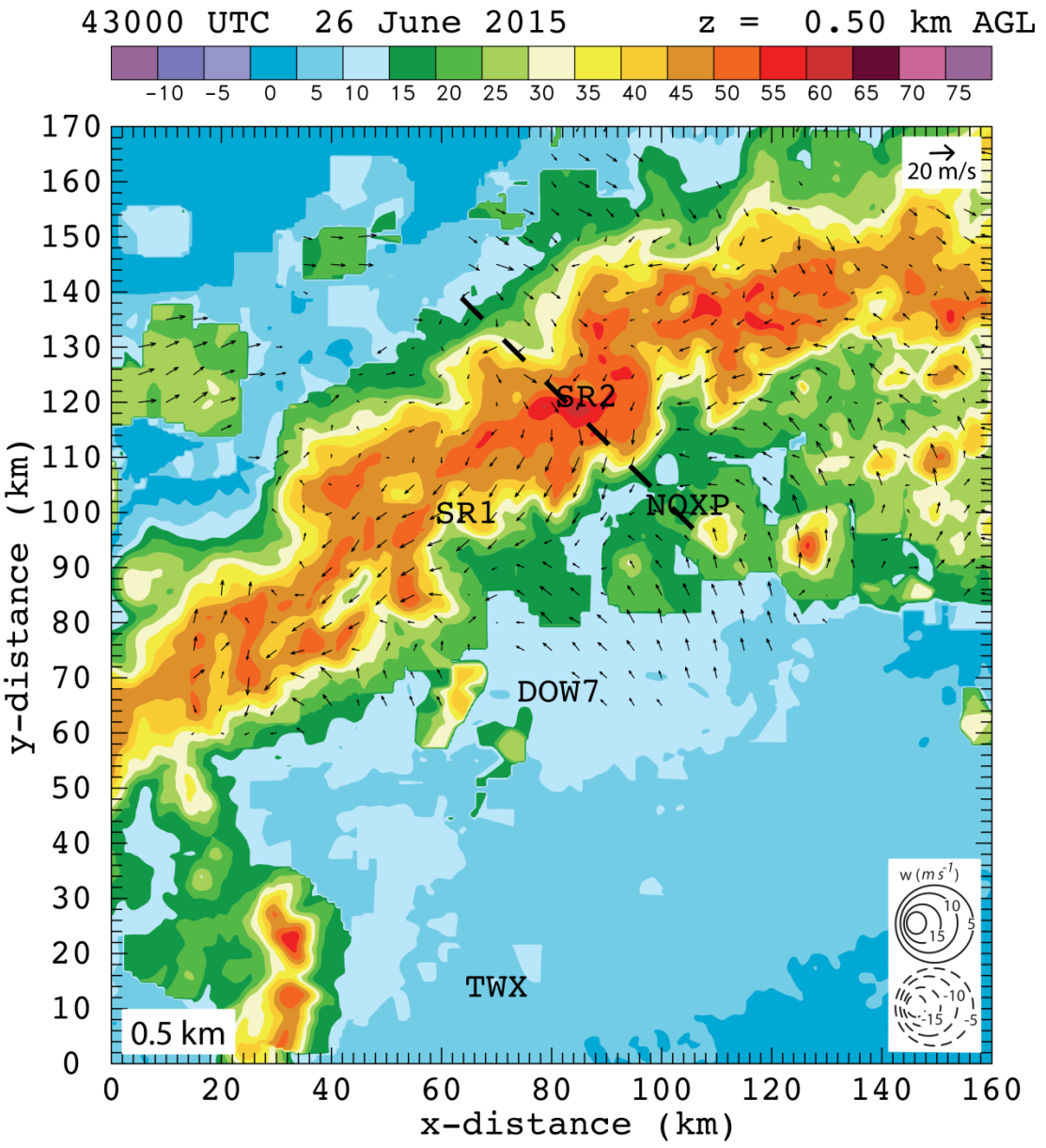

Figure 14. 0.5 km level radar analysis with horizontal wind vectors plotted and dBZ values color-filled at 0430 UTC. The dashed black line indicates the location of the vertical cross section shown in figure 16. 5 radars contributed to this analysis: SR1, SR2, NOXP, Dow7, and KTWX. All radar locations are labeled. Scaling factor for wind vectors and contour intervals are located in the upper right corner and lower right corner, respectively.

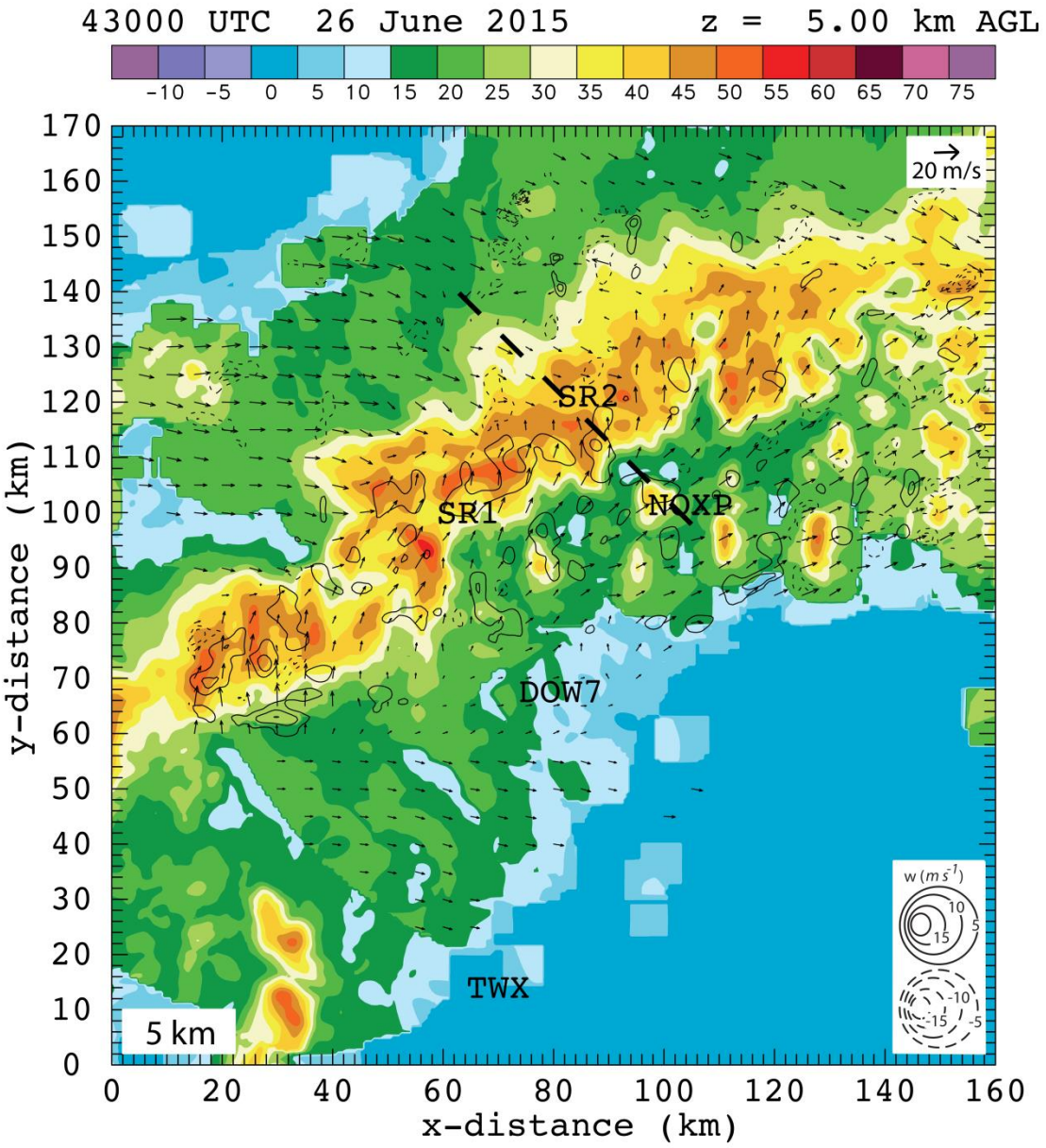

Figure 15. 5 km level radar analysis with horizontal wind vectors plotted and dBZ values color-filled at 0430 UTC. The dashed black line indicates the location of the vertical cross section shown in figure 16. 5 radars contributed to this analysis: SR1, SR2, NOXP, Dow7, and KTWX. All radar locations are labeled. Scaling factor for wind vectors and contour intervals are located in the upper right corner and lower right corner, respectively.

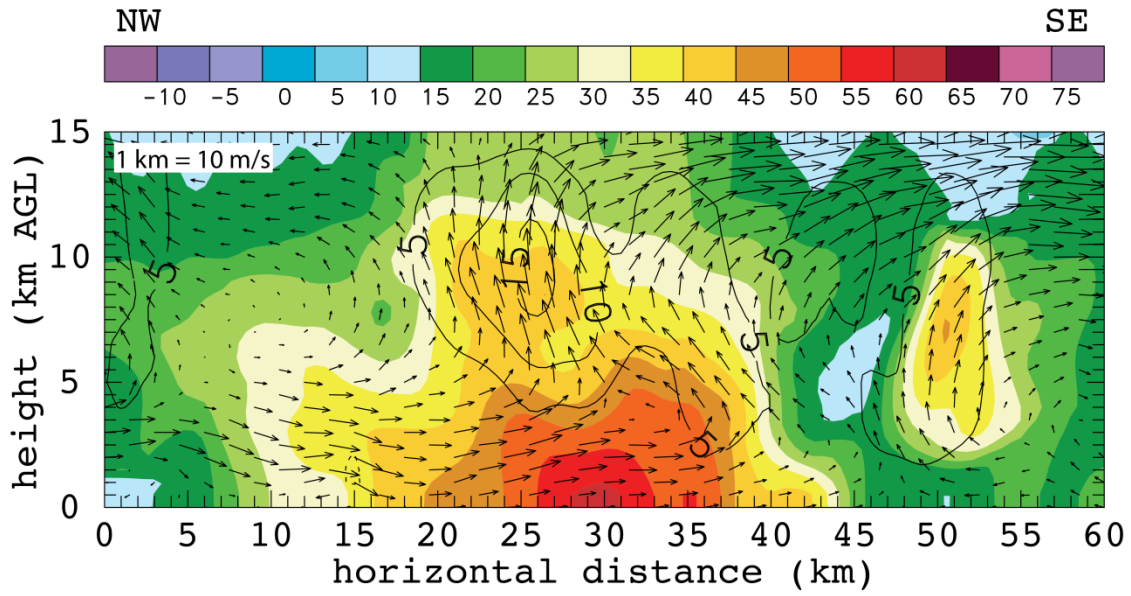

Figure 16. Vertical cross section through radar analysis at 0430 UTC indicated by the dashed black line in figures 14 and 15. dBZ values color-filled and wind vectors plotted with black contours every 5 m/s, solid lines indicated positive w and dashed lines indicate negative w. 5 radars contributed to this analysis: SR1, SR2, NOXP, Dow7, and KTWX. Scaling factor for wind vectors is located in the upper left corner.

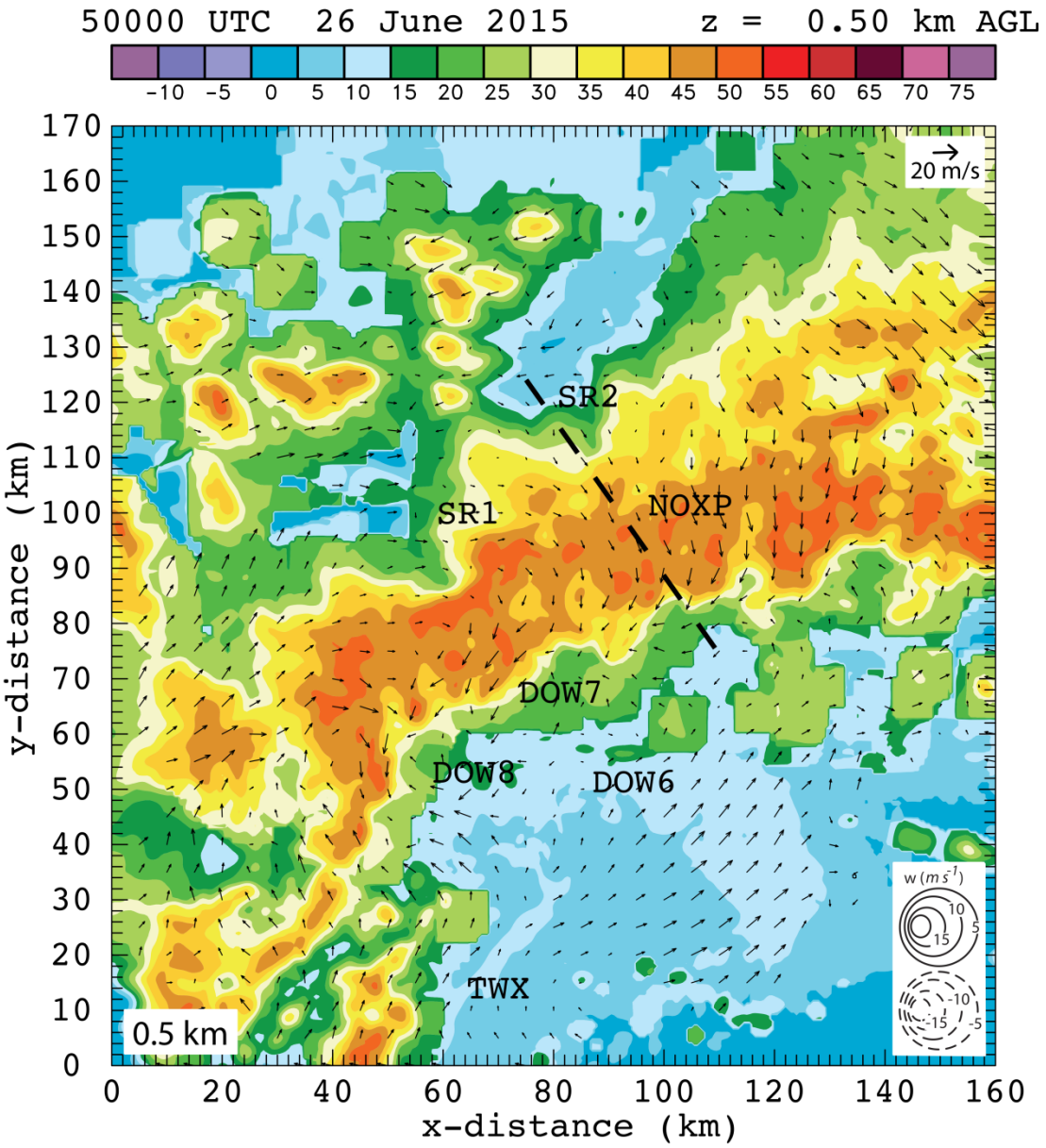

Figure 17. 0.5 km level radar analysis with horizontal wind vectors plotted and dBZ values color-filled at 0500 UTC. The dashed black line indicates the location of the vertical cross section shown in figure 19. 7 radars contributed to this analysis: SR1, SR2, NOXP, Dow7, Dow6, Dow8 and KTWX. All radar locations are labeled. Scaling factor for wind vectors and contour intervals are located in the upper right corner and lower right corner, respectively.

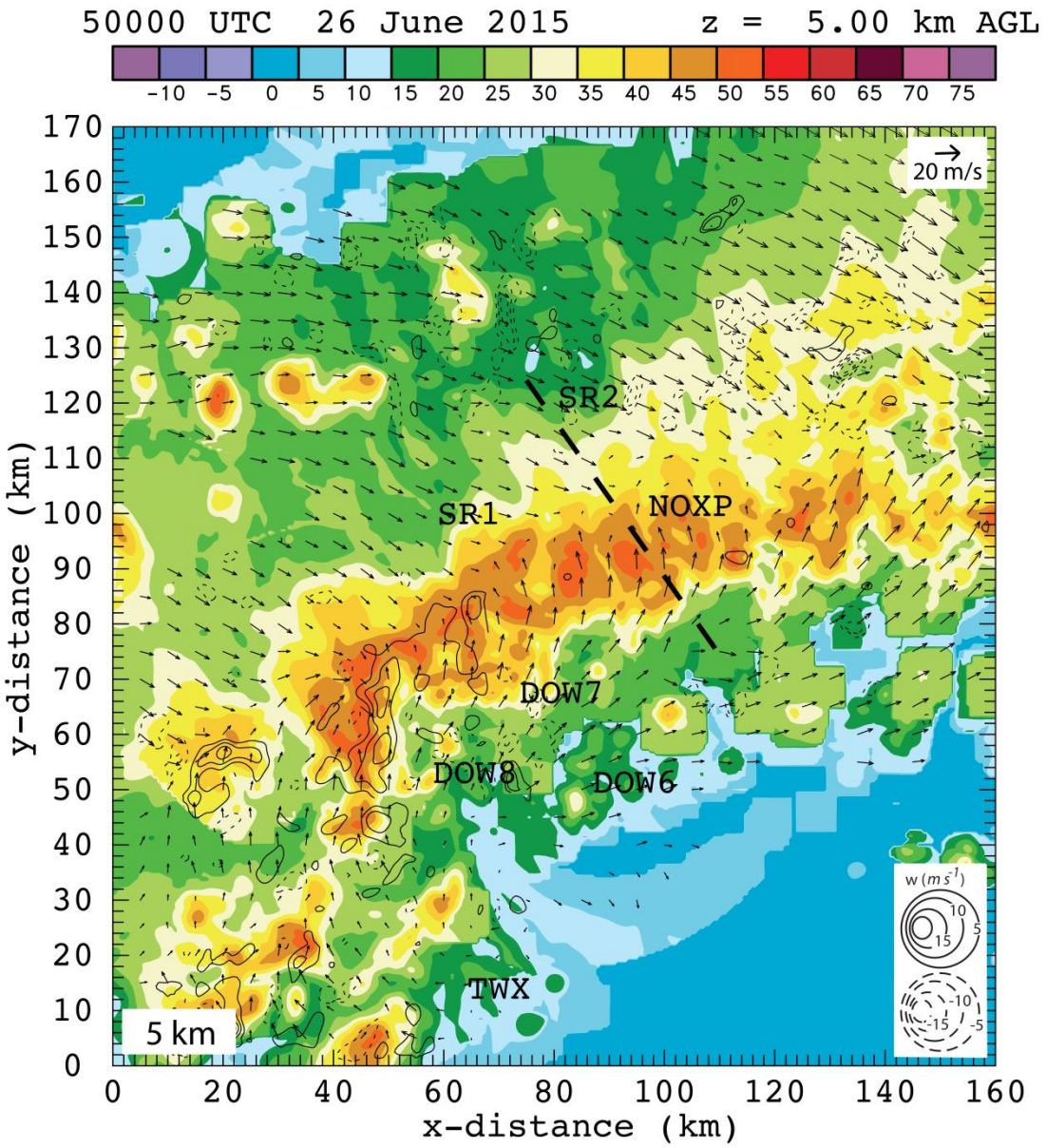

Figure 18. 5 km level radar analysis with horizontal wind vectors plotted and dBZ values color-filled at 0500 UTC. The dashed black line indicates the location of the vertical cross section shown in figure 19. 7 radars contributed to this analysis: SR1, SR2, NOXP, Dow7, Dow6, Dow8 and KTWX. All radar locations are labeled. Scaling factor for wind vectors and contour intervals are located in the upper right corner and lower right corner, respectively.

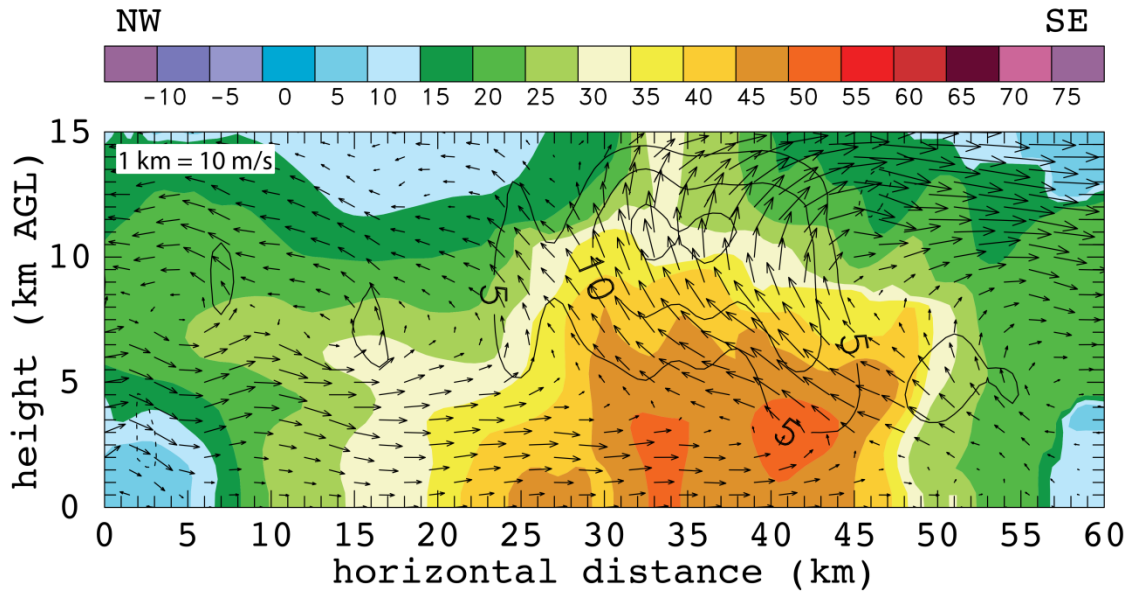

Figure 19. Vertical cross section through radar analysis at 0500 UTC indicated by the dashed black line in figures 17 and 18. dBZ values color-filled and wind vectors plotted with black contours every 5 m/s, solid lines indicated positive w and dashed lines indicate negative w. 7 radars contributed to this analysis: SR1, SR2, NOXP, Dow7, Dow6, Dow8 and KTWX. Scaling factor for wind vectors is located in the upper left corner.

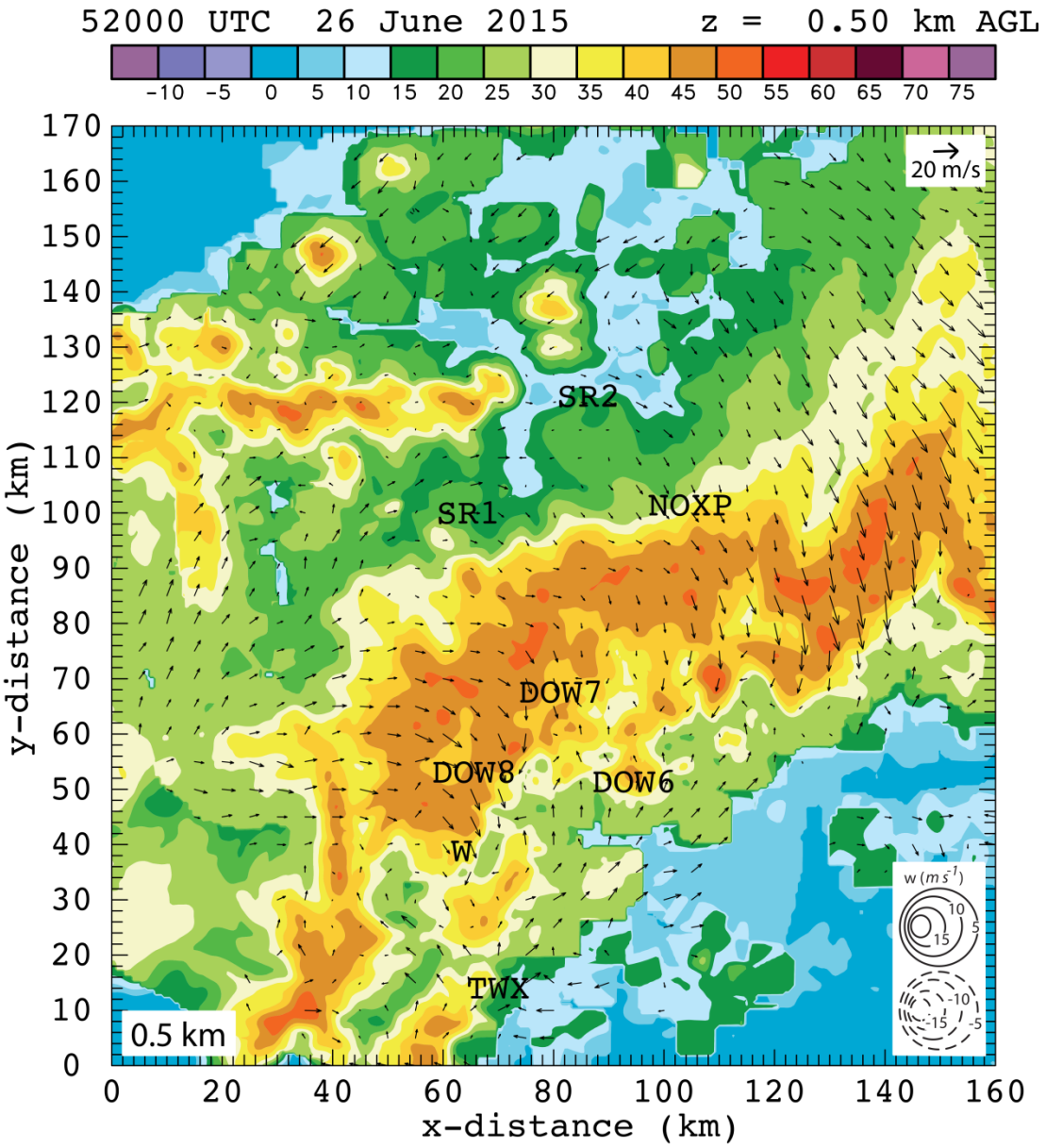

Figure 20. 0.5 km level radar analysis with horizontal wind vectors plotted and dBZ values color-filled at 0520 UTC. 7 radars contributed to this analysis: SR1, SR2, NOXP, Dow7, Dow6, Dow8 and KTWX. All radar locations are labeled. Scaling factor for wind vectors and contour intervals are located in the upper right corner and lower right corner, respectively. Wind report location is labeled with a "W" south of Dow8.

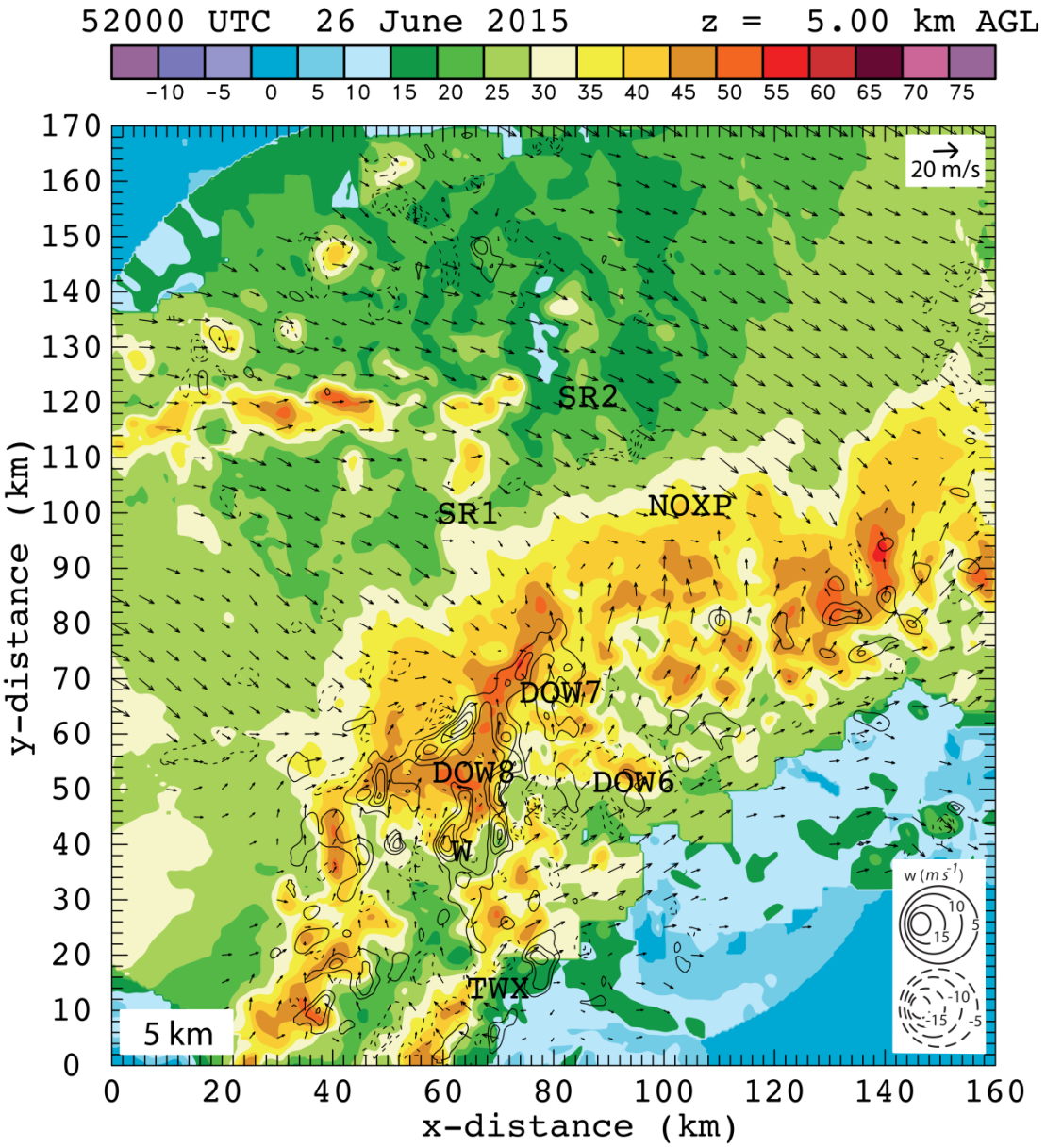

Figure 21. 5 km level radar analysis with horizontal wind vectors plotted and dBZ values color-filled at 0520 UTC. 7 radars contributed to this analysis: SR1, SR2, NOXP, Dow7, Dow6, Dow8 and KTWX. All radar locations are labeled. Scaling factor for wind vectors and contour intervals are located in the upper right corner and lower right corner, respectively. Wind report location is labeled with a "W" south of Dow8.

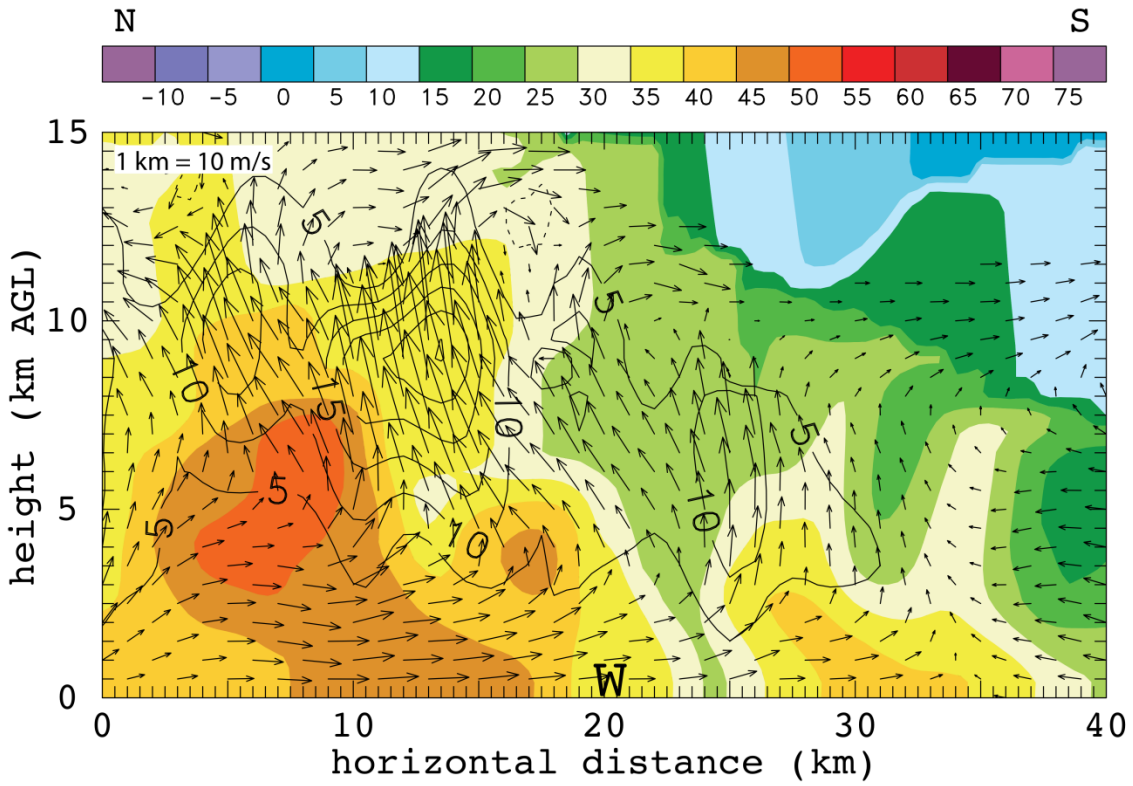

Figure 22. Vertical cross section through radar analysis at 0520 UTC centered on the wind report labeled with a "W" and oriented north-south. dBZ values color-filled and wind vectors plotted with black contours every 5 m/s, solid lines indicated positive w and dashed lines indicate negative w. 7 radars contributed to this analysis: SR1, SR2, NOXP, Dow7, Dow6, Dow8 and KTWX. Scaling factor for wind vectors is located in the upper left corner.

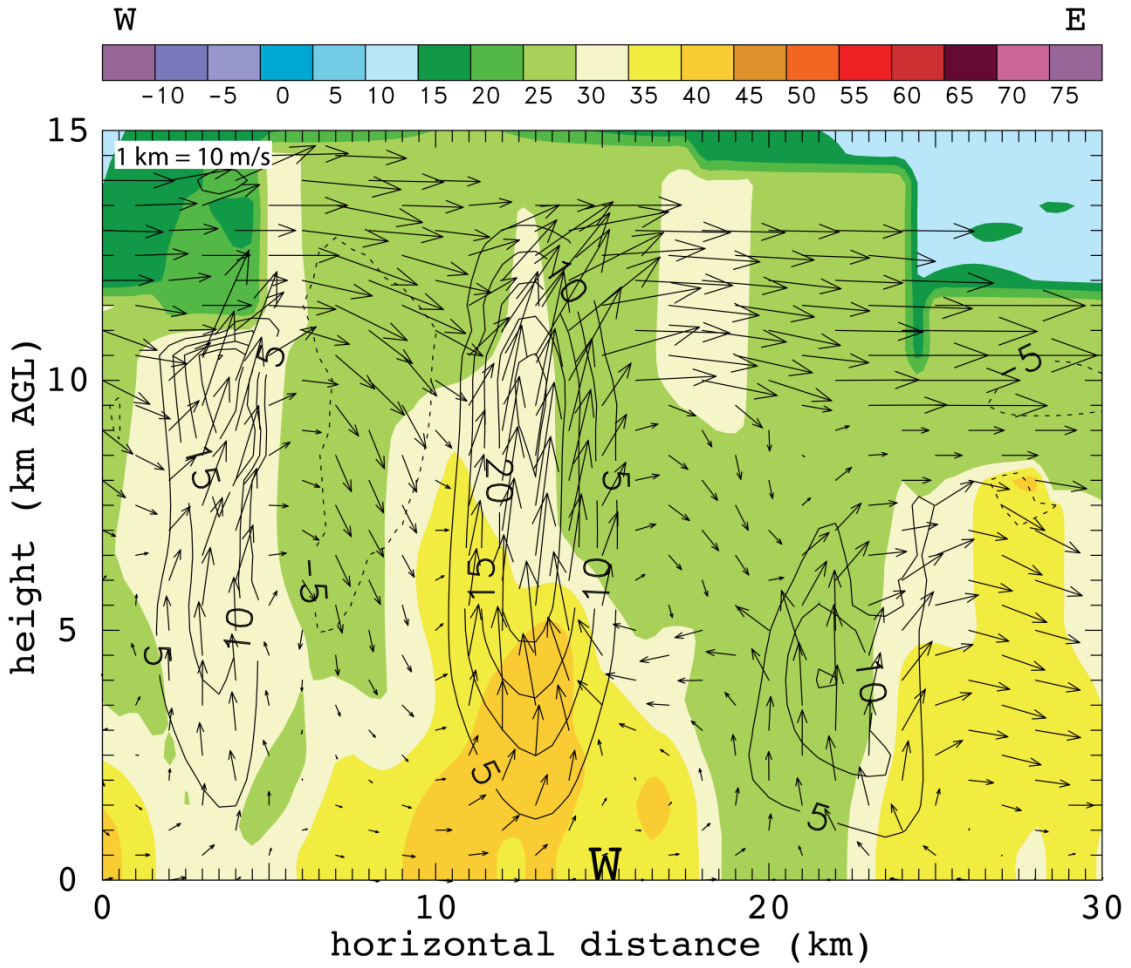

Figure 23. Vertical cross section through radar analysis at 0520 UTC centered on the wind report labeled with a "W" and oriented east-west. dBZ values color-filled and wind vectors plotted with black contours every 5 m/s, solid lines indicated positive w and dashed lines indicate negative w. 7 radars contributed to this analysis: SR1, SR2, NOXP, Dow7, Dow6, Dow8 and KTWX. Scaling factor for wind vectors is located in the upper left corner.

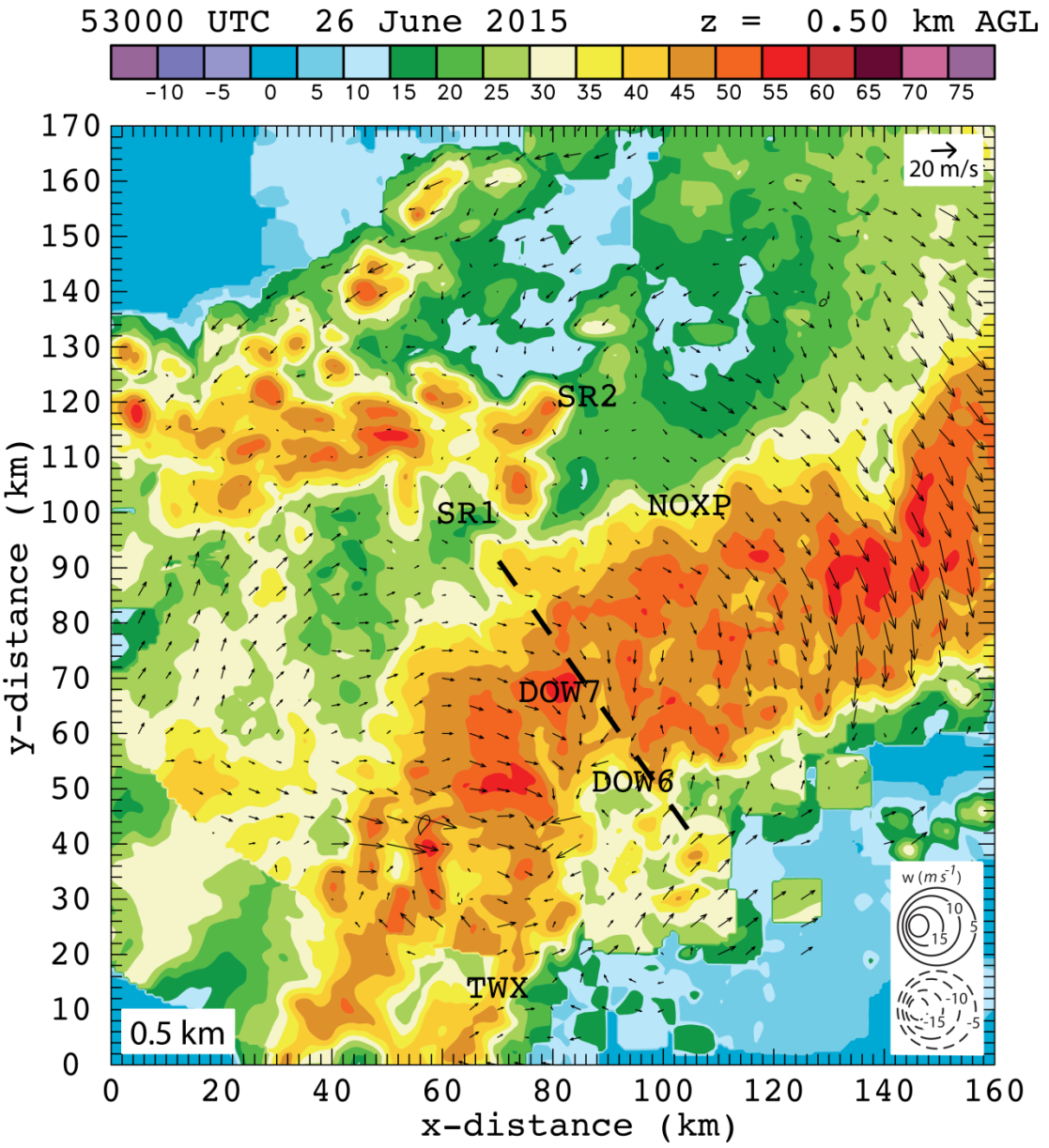

Figure 24. 0.5 km level radar analysis with horizontal wind vectors plotted and dBZ values color-filled at 0530 UTC. The dashed black line indicates the location of the vertical cross section shown in figure 26. 6 radars contributed to this analysis: SR1, SR2, NOXP, Dow7, Dow6, and KTWX. All radar locations are labeled. Scaling factor for wind vectors and contour intervals are located in the upper right corner and lower right corner, respectively.

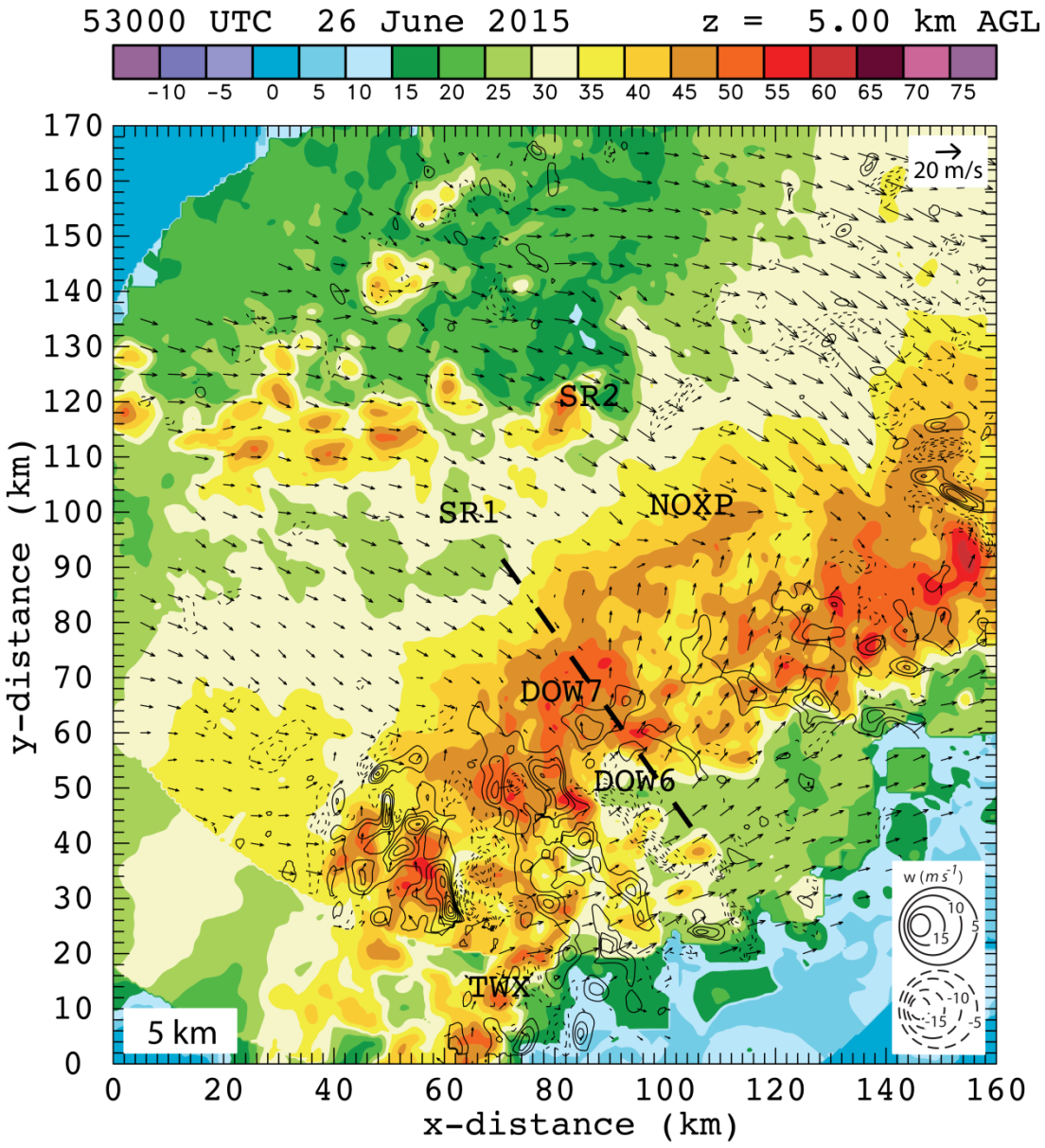

Figure 25. 5 km level radar analysis with horizontal wind vectors plotted and dBZ values color-filled at 0530 UTC. The dashed black line indicates the location of the vertical cross section shown in figure 26. 6 radars contributed to this analysis: SR1, SR2, NOXP, Dow7, Dow6, and KTWX. All radar locations are labeled. Scaling factor for wind vectors and contour intervals are located in the upper right corner and lower right corner, respectively.

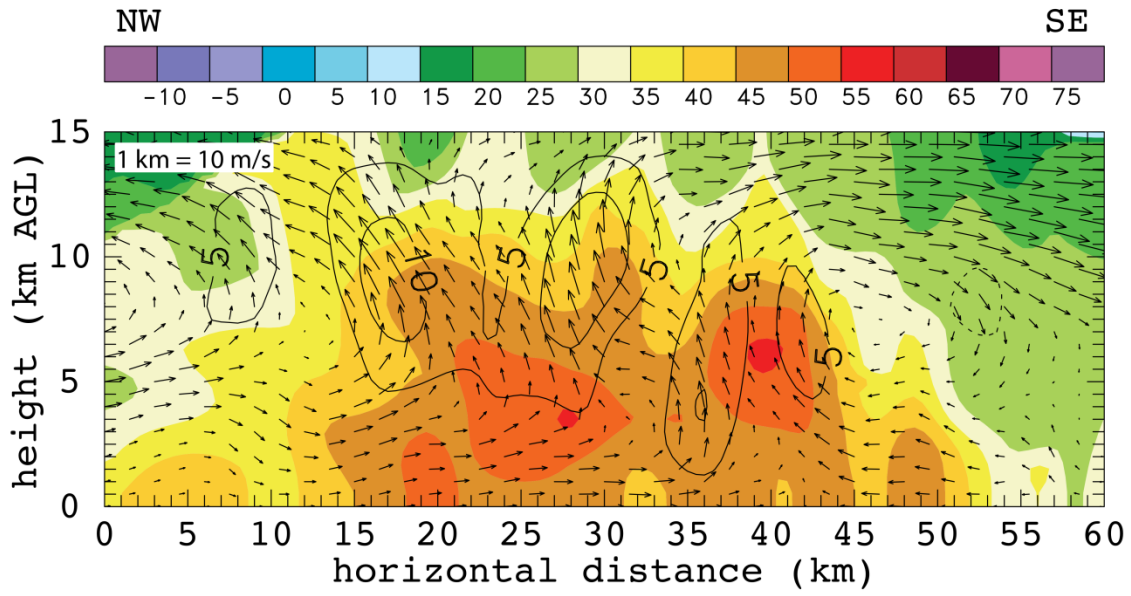

Figure 26. Vertical cross section through radar analysis at 0530 UTC indicated by the dashed black line in figures 24 and 25. dBZ values color-filled and wind vectors plotted with black contours every 5 m/s, solid lines indicated positive w and dashed lines indicate negative w. 6 radars contributed to this analysis: SR1, SR2, NOXP, Dow7, Dow6, and KTWX. Scaling factor for wind vectors is located in the upper left corner.

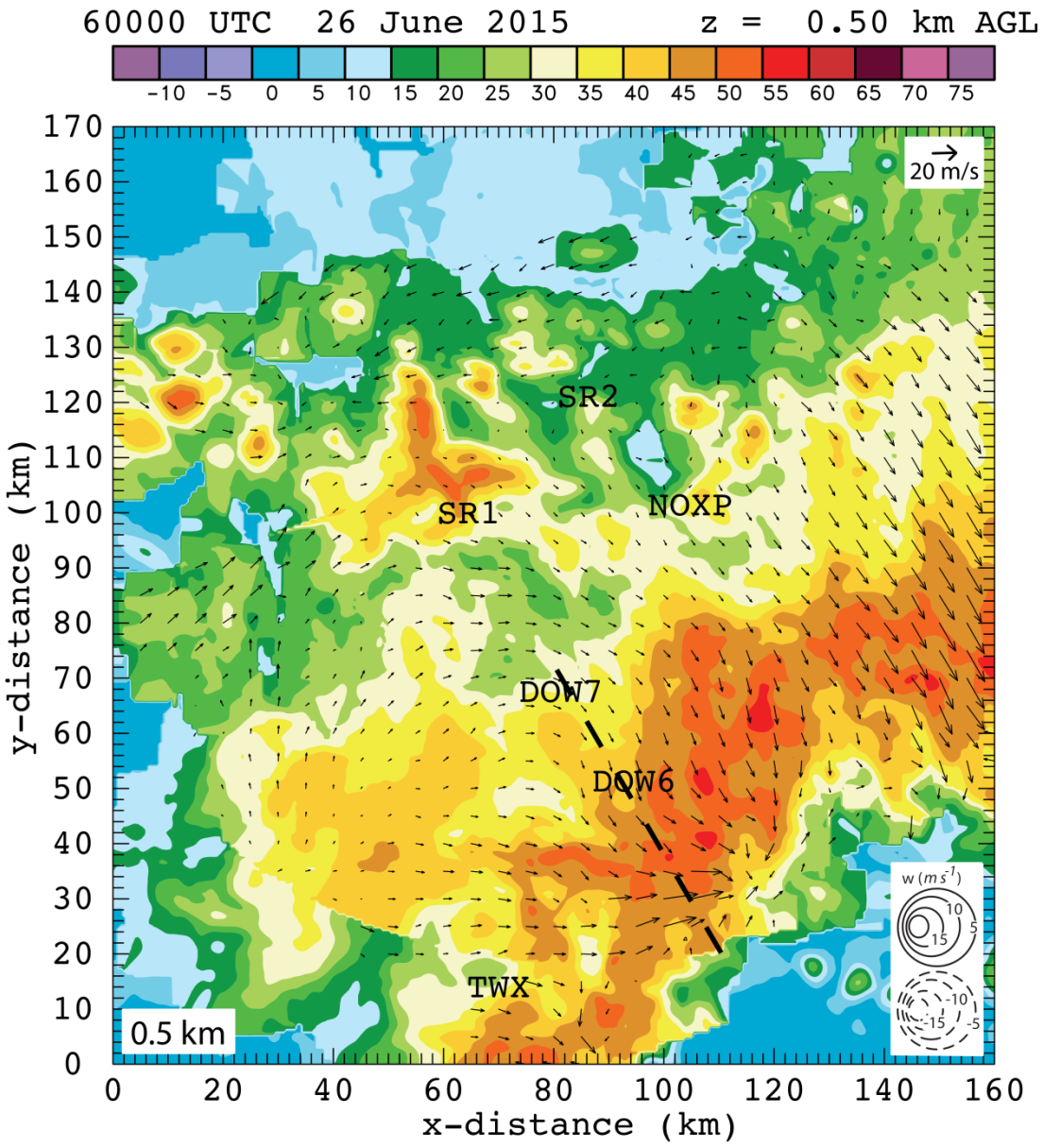

Figure 27. 0.5 km level radar analysis with horizontal wind vectors plotted and dBZ values color-filled at 0600 UTC. The dashed black line indicates the location of the vertical cross section shown in figure 29. 6 radars contributed to this analysis: SR1, SR2, NOXP, Dow7, Dow6, and KTWX. All radar locations are labeled. Scaling factor for wind vectors and contour intervals are located in the upper right corner and lower right corner, respectively.

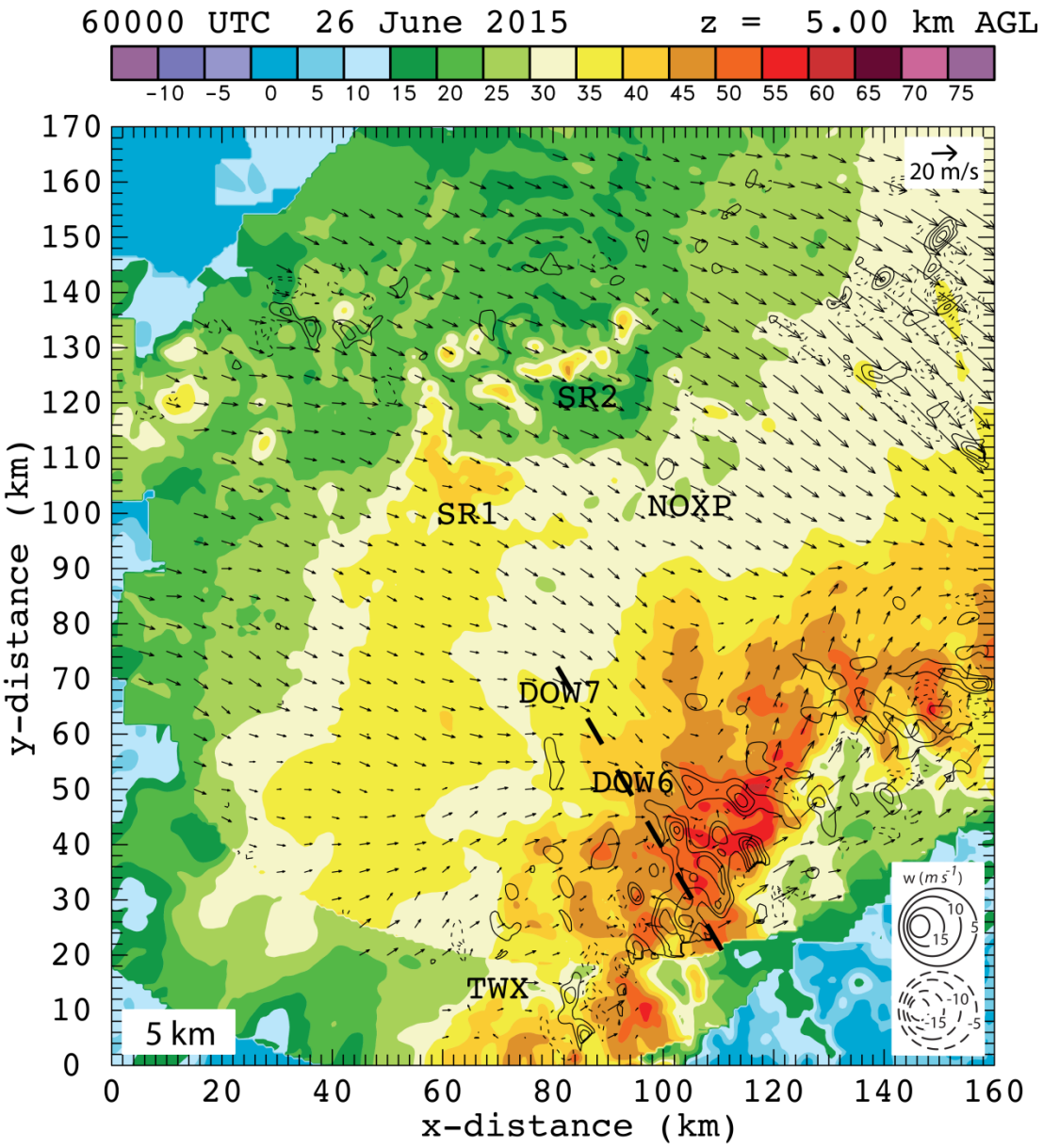

Figure 28. 5 km level radar analysis with horizontal wind vectors plotted and dBZ values color-filled at 0600 UTC. The dashed black line indicates the location of the vertical cross section shown in figure 29. 6 radars contributed to this analysis: SR1, SR2, NOXP, Dow7, Dow6, and KTWX. All radar locations are labeled. Scaling factor for wind vectors and contour intervals are located in the upper right corner and lower right corner, respectively.

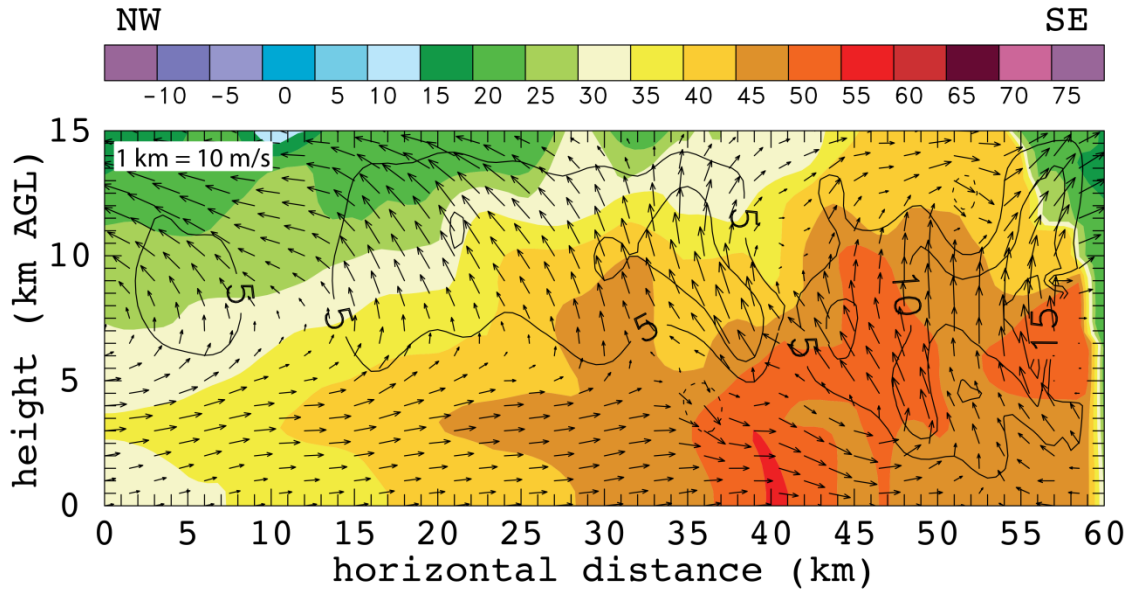

Figure 29. Vertical cross section through radar analysis at 0600 UTC indicated by the dashed black line in figures 27 and 28. dBZ values color-filled and wind vectors plotted with black contours every 5 m/s, solid lines indicated positive w and dashed lines indicate negative w. 6 radars contributed to this analysis: SR1, SR2, NOXP, Dow7, Dow6, and KTWX. Scaling factor for wind vectors is located in the upper left corner.

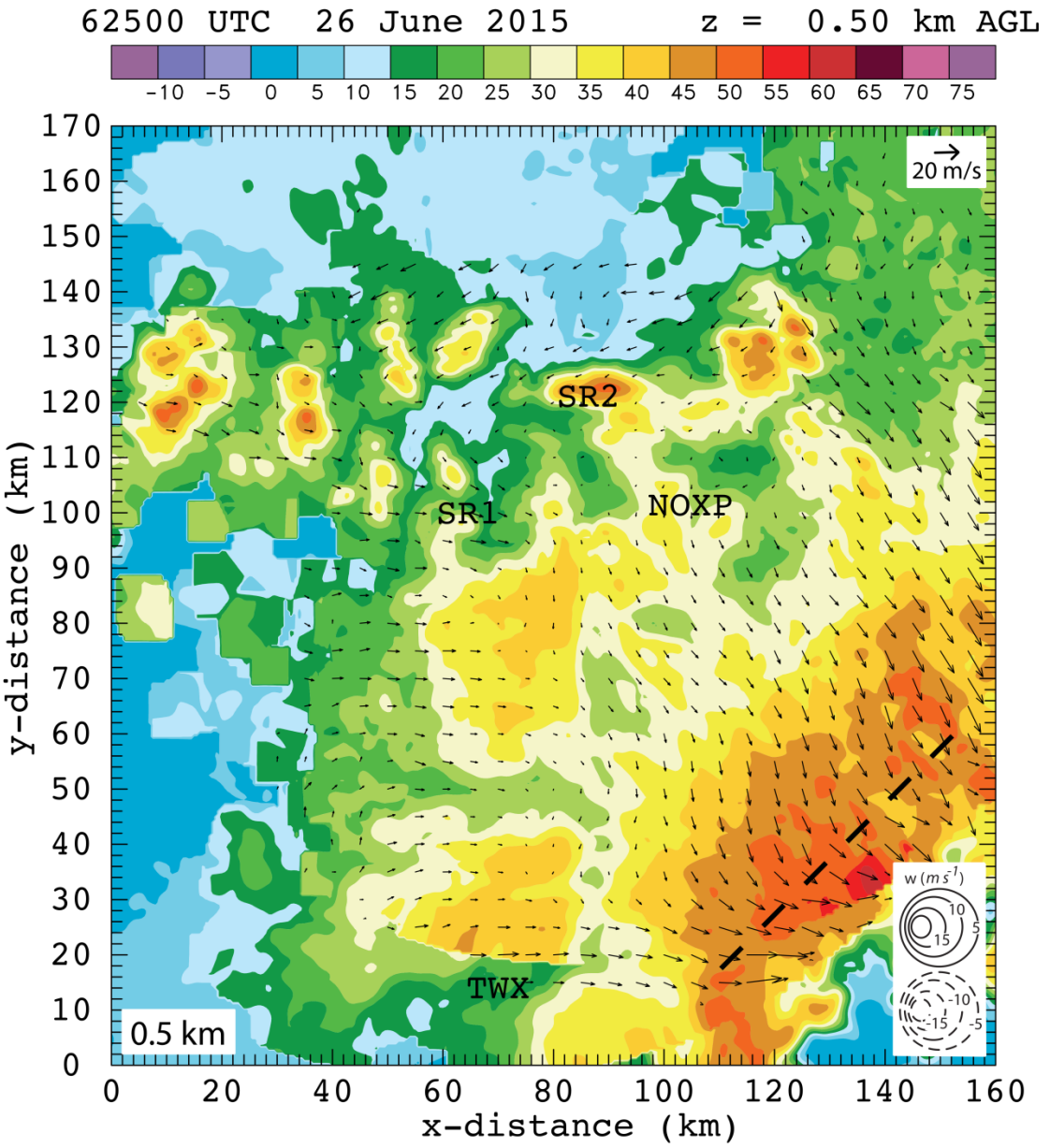

Figure 30. 0.5 km level radar analysis with horizontal wind vectors plotted and dBZ values color-filled at 0625 UTC. The dashed black line indicates the location of the vertical cross section shown in figure 32. 4 radars contributed to this analysis: SR1, SR2, and KTWX. All radar locations are labeled. Scaling factor for wind vectors and contour intervals are located in the upper right corner and lower right corner, respectively.

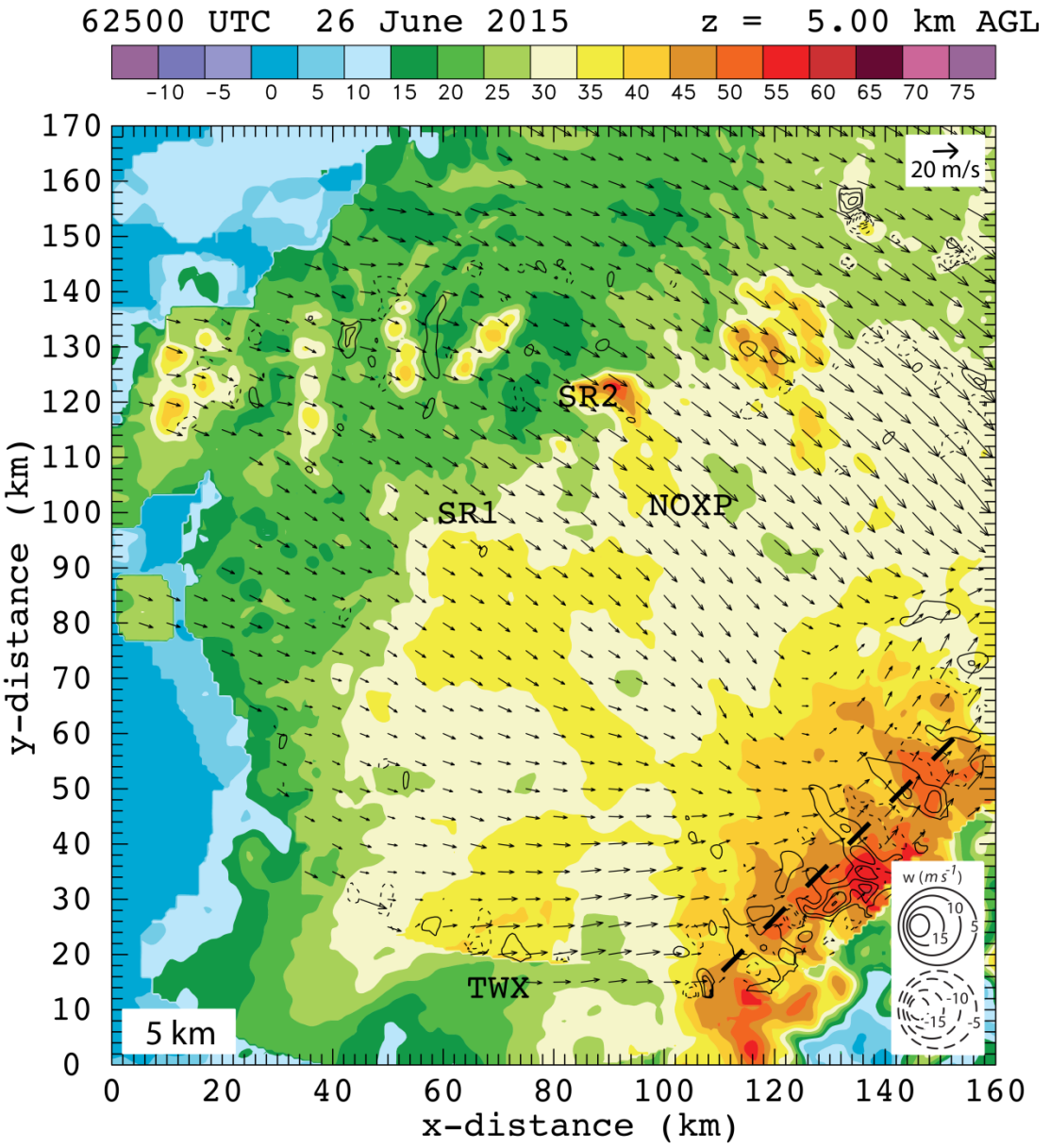

Figure 31. 5 km level radar analysis with horizontal wind vectors plotted and dBZ values color-filled at 0625 UTC. The dashed black line indicates the location of the vertical cross section shown in figure 32. 4 radars contributed to this analysis: SR1, SR2, and KTWX. All radar locations are labeled. Scaling factor for wind vectors and contour intervals are located in the upper right corner and lower right corner, respectively.

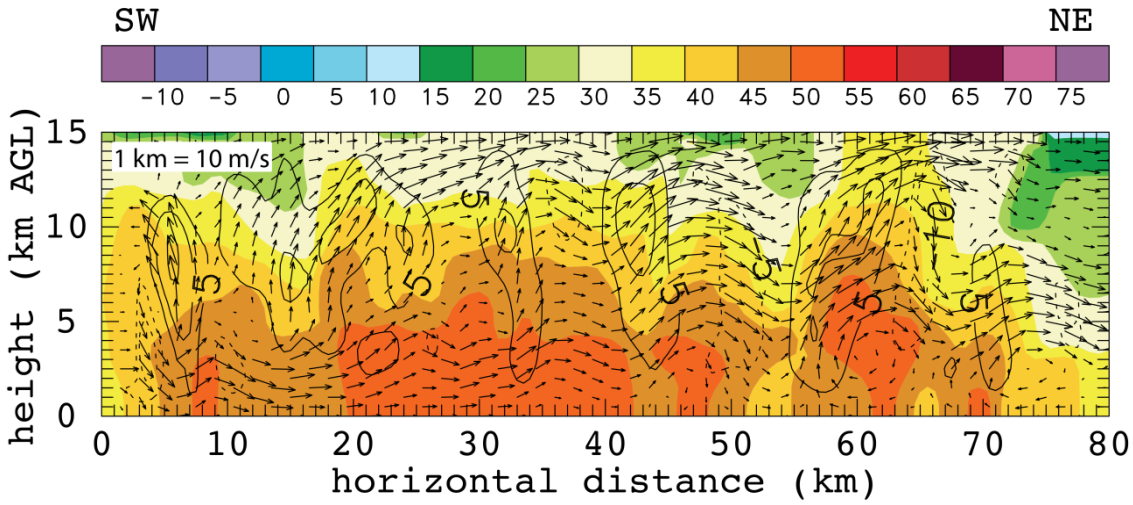

Figure 32. Vertical cross section through radar analysis at 0625 UTC indicated by the dashed black line in figures 30 and 31. dBZ values color-filled and wind vectors plotted with black contours every 5 m/s, solid lines indicated positive w and dashed lines indicate negative w. 4 radars contributed to this analysis: SR1, SR2, NOXP, and KTWX. Scaling factor for wind vectors is located in the upper left corner.

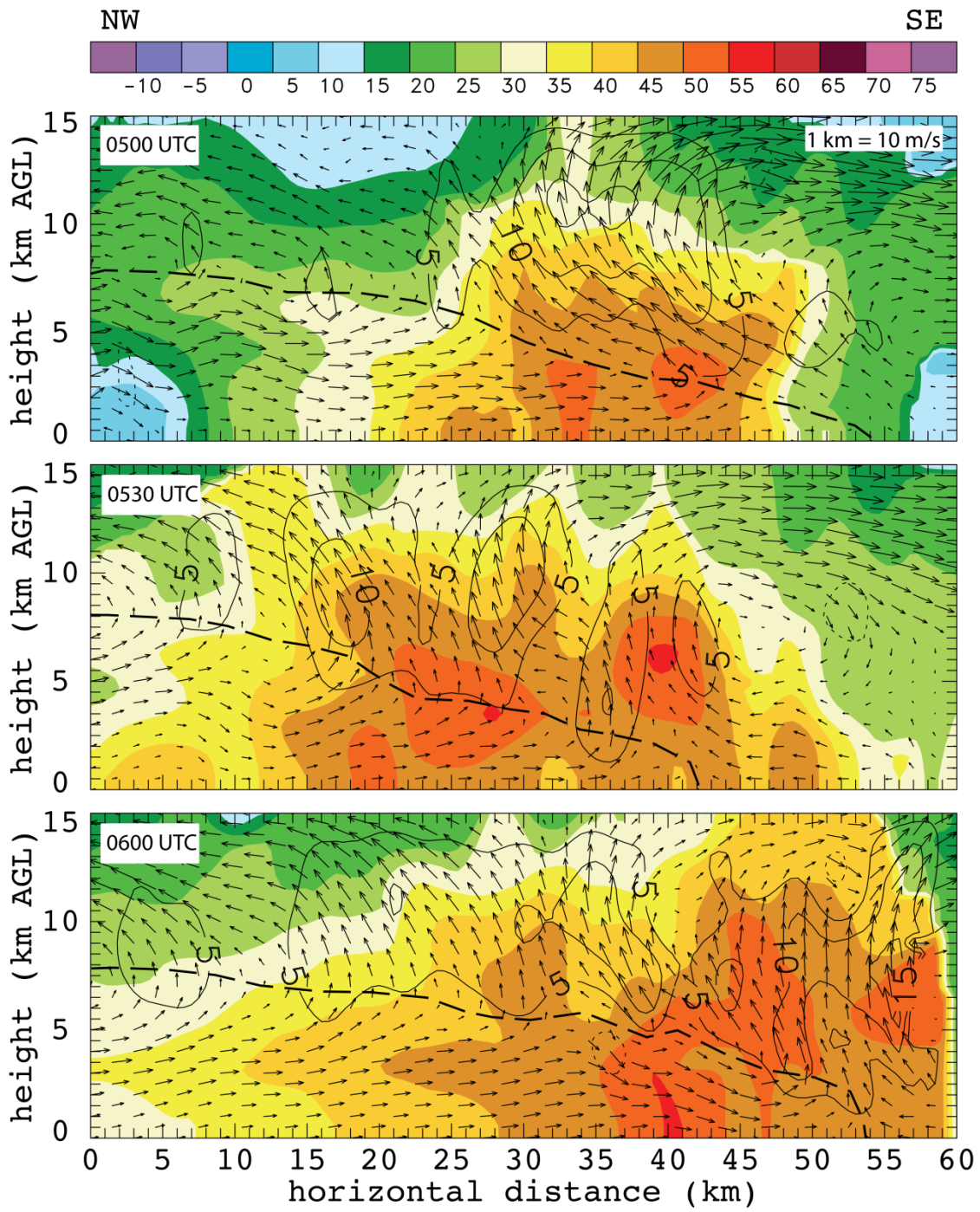

Figure 33. 3 northwest to southeast oriented vertical cross sections from 0500, 0530, and 0600 UTC (figures 23, 26, and 29 respectively). W contours, color fill, and scaling are all the same as previous vertical cross section figures. Time of cross section is labeled in the upper left corner. Dashed black line is the interface between the front to rear and rear to front flow.

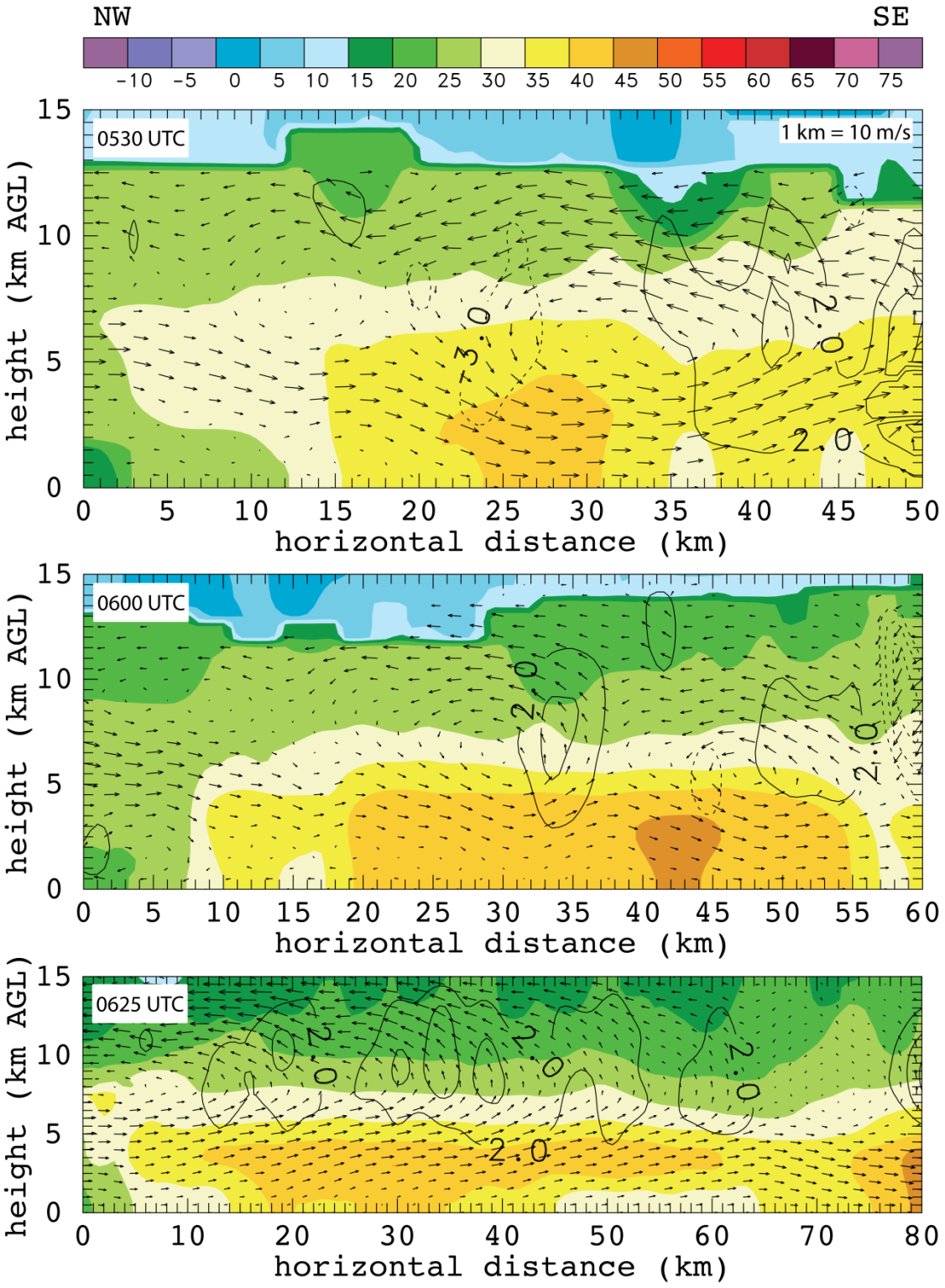

Figure 34. Northwest to southeast oriented vertical cross sections from 0530, 0600, and 0625 UTC through the stratiform precipitation region. The 0530 and 0600 UTC cross sections are in the bowing MCS's stratiform region while the cross section at 0625 UTC is through the linear MCS's stratiform region. Color fill and

scaling are the same as previous vertical cross section figures however the w contours are now every 2 m/s with solid line indicating positive w and dashed lines indicating negative w. Time of cross section is labeled in the upper left corner.

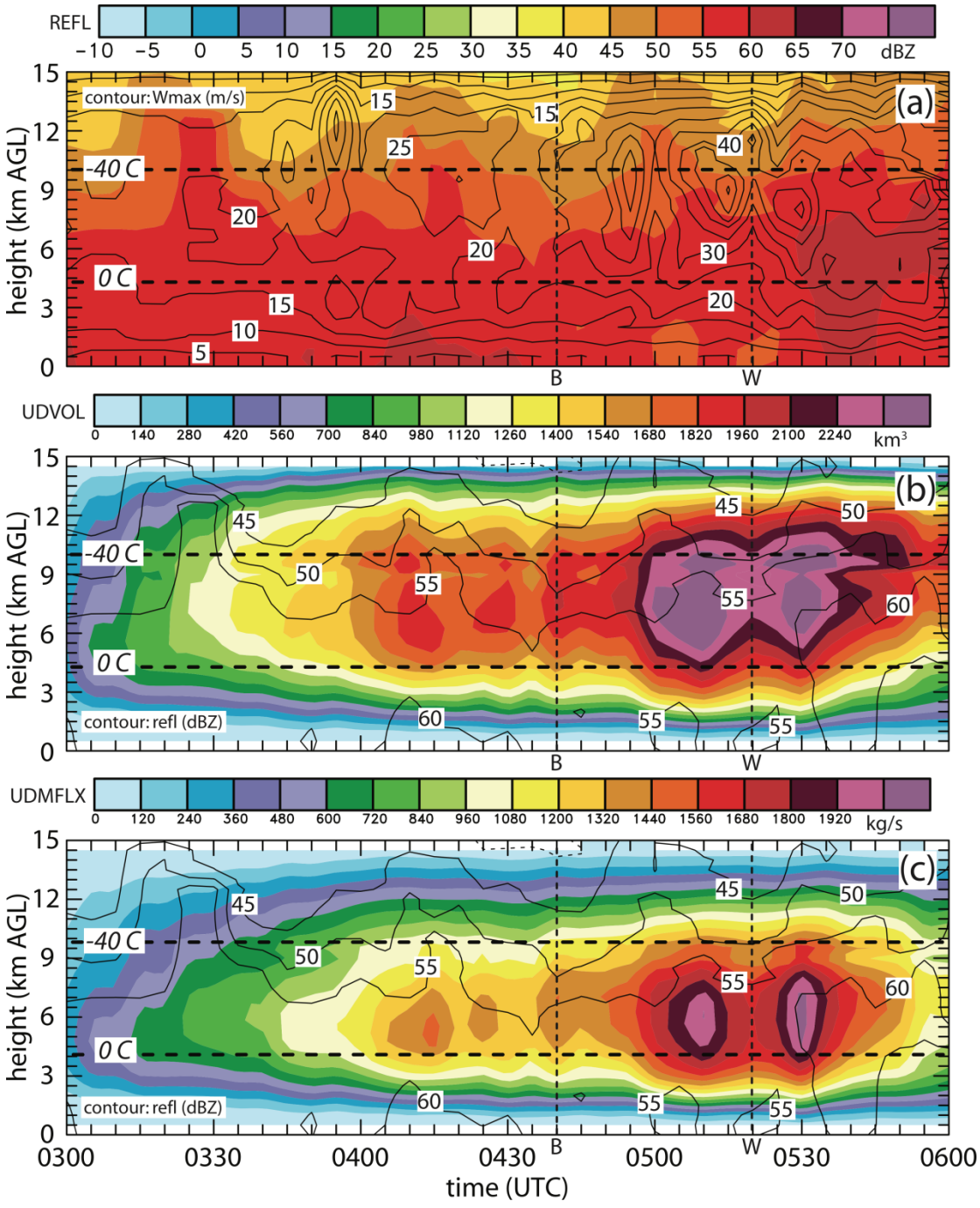

Figure 35. Integrated values for entire radar domain for a 3 hour time period from 0300 to 0600 UTC with the 0° and -40° Celsius isotherm overlaid. Vertical line B

indicates the first time the surging outflow feature is noted and vertical line W indicates the approximate time of the first wind report. Panel (a) shows color filled maximum reflectivity at each level with the maximum w value contoured. Panel (b) shows color filled updraft volume, which is a summation of every grid cell volume with W greater than 3 m/s, with the maximum reflectivity contoured. Panel (c) shows color filled updraft volume flux, which is the updraft volume weighted with the W value, with maximum reflectivity contoured.

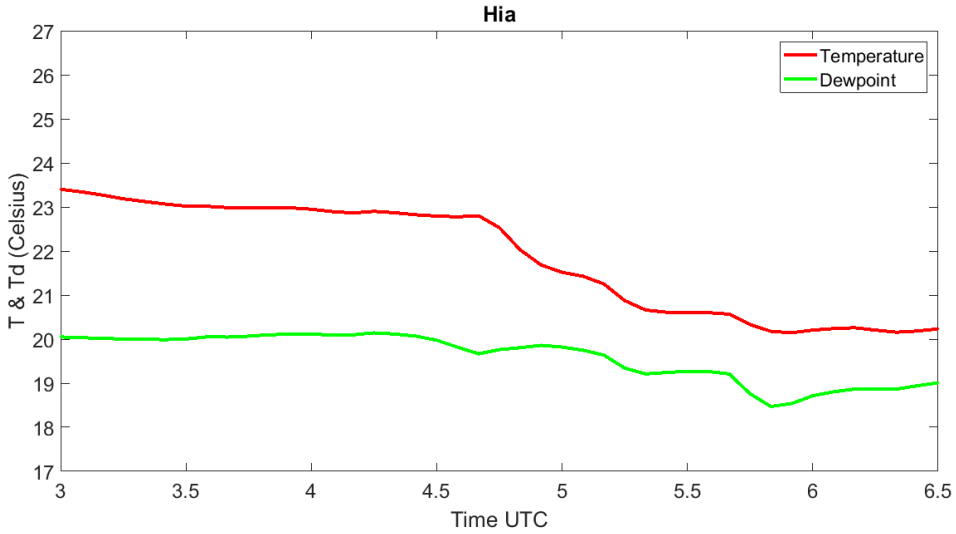

Figure 36. Temperature (red line) and dewpoint (green line) in Celsius at the Hiawatha Kansas mesonet station from 0300 to 0630 UTC. Data is recorded every 5 minutes as a 5 minute average.

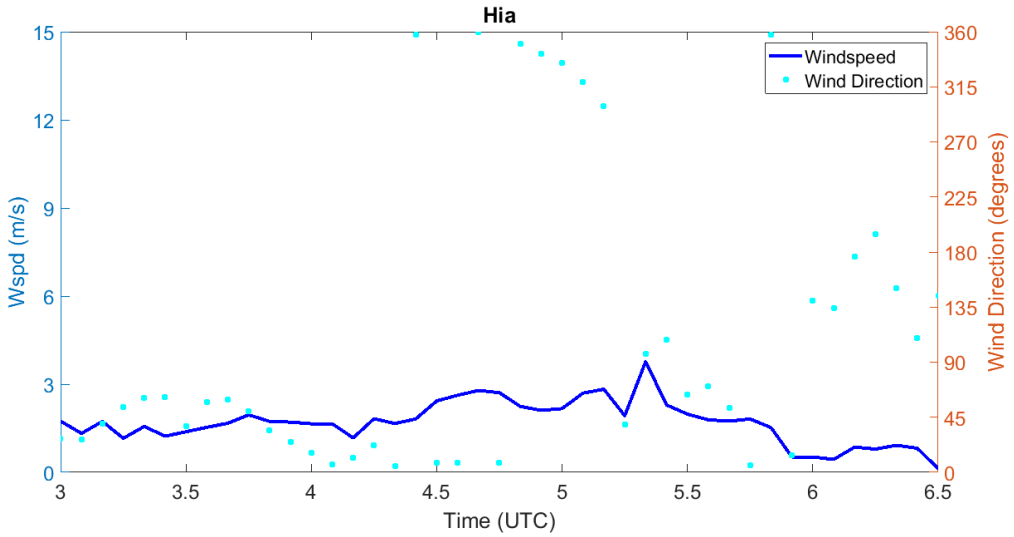

Figure 37. Windspeed (dark blue line) in meters per second and wind direction (light blue dots) in degrees at the Hiawatha Kansas mesonet station from 0300 to 0630 UTC. Data is recorded every 5 minutes as a 5 minute average.

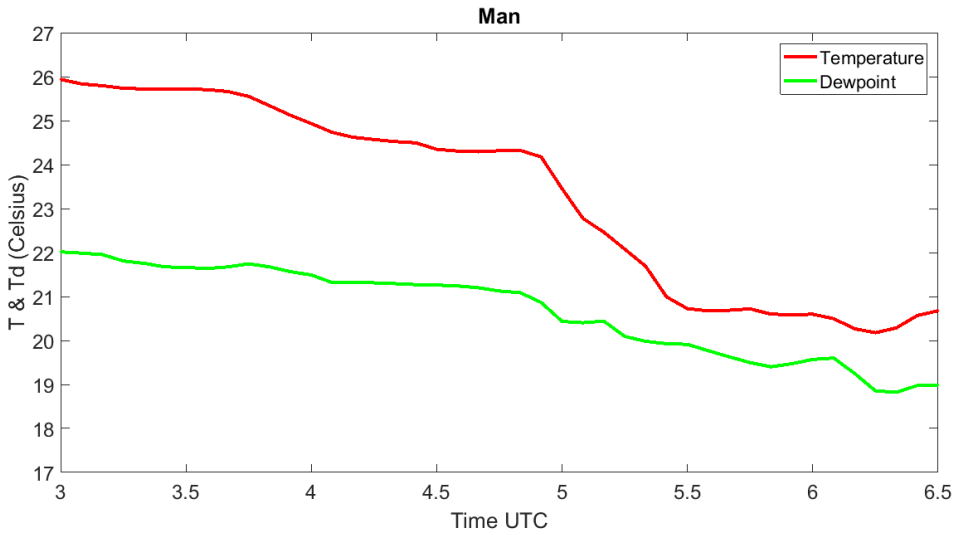

Figure 38. Temperature (red line) and dewpoint (green line) in Celsius at the Manhattan Kansas mesonet station from 0300 to 0630 UTC. Data is recorded every 5 minutes as a 5 minute average.

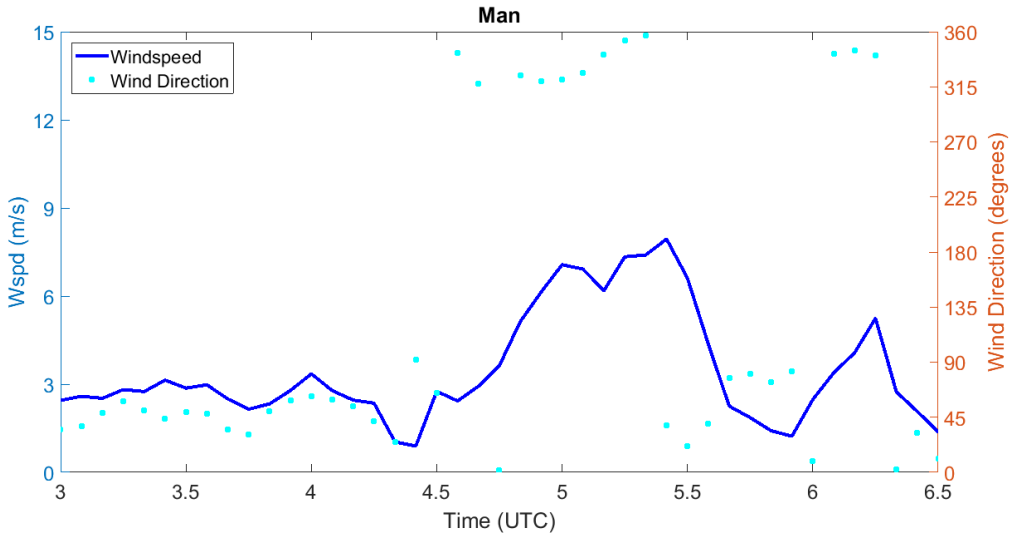

Figure 39. Windspeed (dark blue line) in meters per second and wind direction (light blue dots) in degrees at the Manhattan Kansas mesonet station from 0300 to 0630 UTC. Data is recorded every 5 minutes as a 5 minute average.

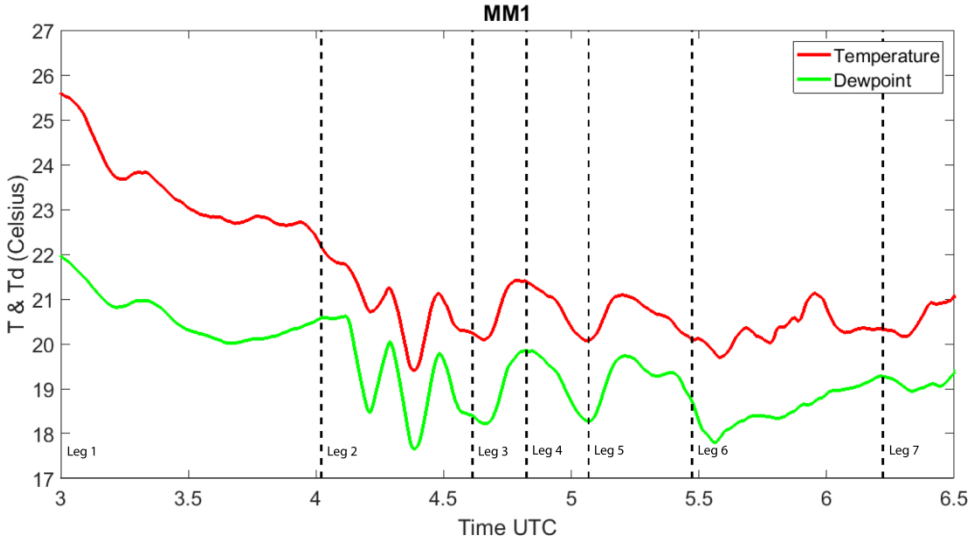

Figure 40. Temperature (red line) and dewpoint (green line) in Celsius recorded by MM1 as it drove around the MCS environment from 0300 to 0630 UTC. Vertical dashed lines indicate that the mesonet changed directions. MM1 drove north for leg 1, west for leg 2, south for leg 3, east for leg 4, south for leg 5, southeast for leg 6, and west for leg 7.

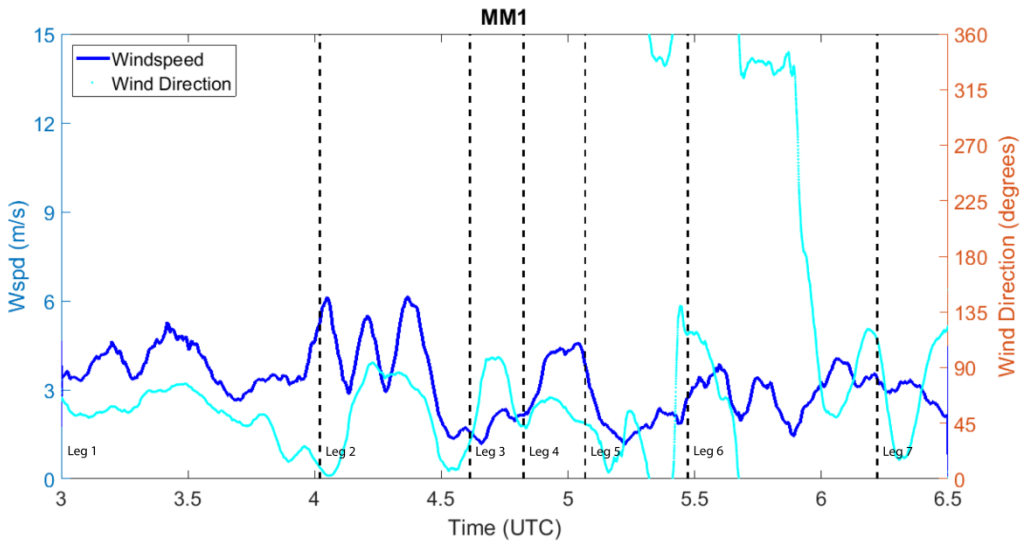

Figure 41. Windspeed (dark blue line) in meters per second and wind direction (light blue dots) in degrees recorded by MM1 as it drove around the MCS environment from 0300 to 0630 UTC. Vertical dashed lines indicate that the mesonet changed directions. MM1 drove north for leg 1, west for leg 2, south for leg 3, east for leg 4, south for leg 5, southeast for leg 6, and west for leg 7.

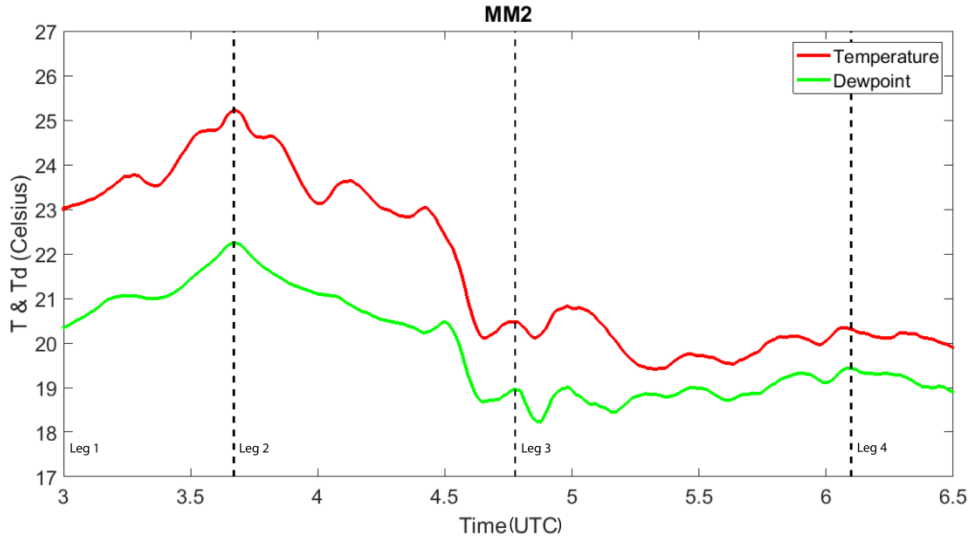

Figure 42. Temperature (red line) and dewpoint (green line) in Celsius recorded by MM2 as it drove around the MCS environment from 0300 to 0630 UTC. Vertical dashed lines indicate that the mesonet changed directions. MM1 drove south for leg 1, north for leg 2, south for leg 3, and southeast for leg 4.

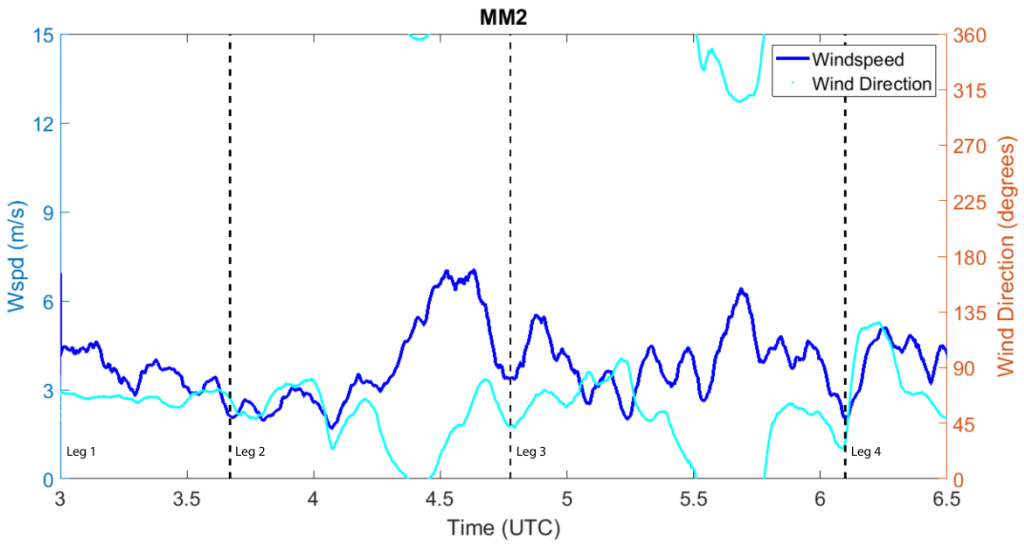

Figure 43. Windspeed (dark blue line) in meters per second and wind direction (light blue dots) in degrees recorded by MM2 as it drove around the MCS environment from 0300 to 0630 UTC. Vertical dashed lines indicate that the mesonet changed directions. MM1 drove south for leg 1, north for leg 2, south for leg 3, and southeast for leg 4.

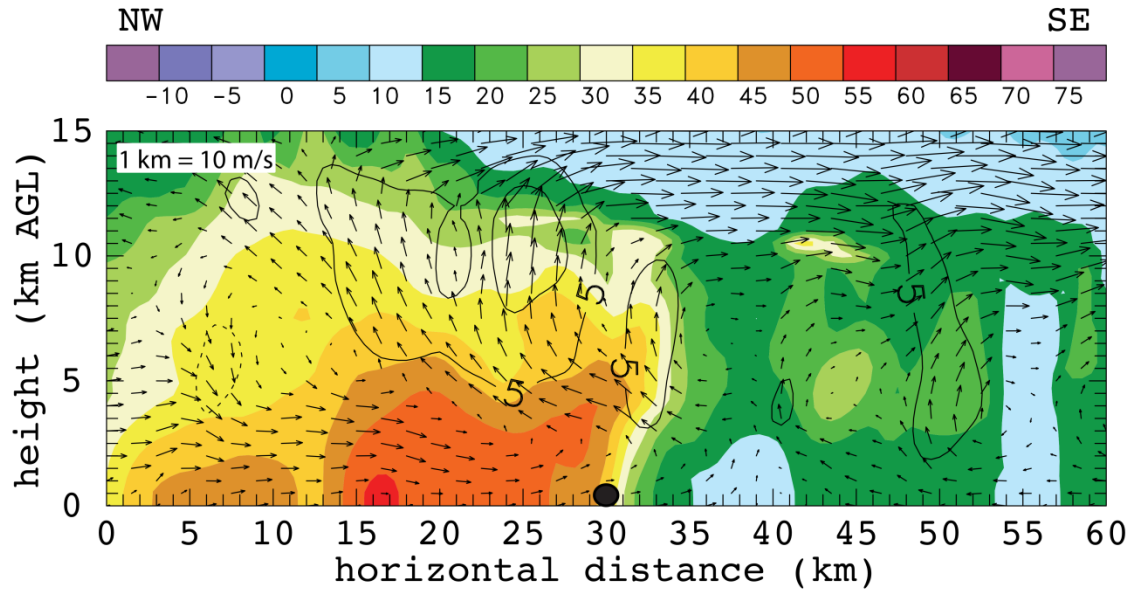

Figure 44. Northwest to southeast vertical cross section of radar analysis at 0430 UTC centered over MM2 (black dot). dBZ values color-filled and wind vectors plotted with black contours every 5 m/s, solid lines indicated positive w and dashed lines indicate negative w. 5 radars contributed to this analysis: SR1, SR2, NOXP, Dow7, and KTWX. Scaling factor for wind vectors is located in the upper left corner.

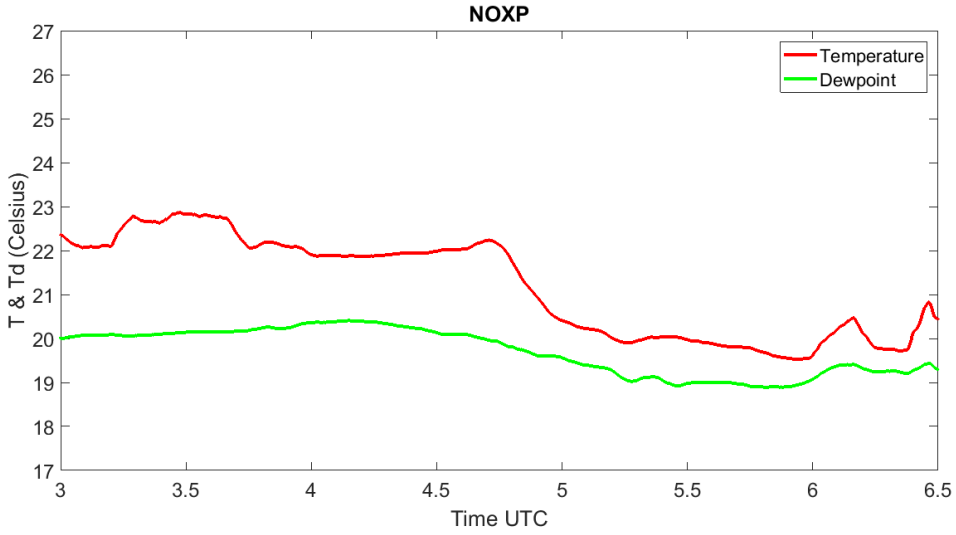

Figure 45. Temperature (red line) and dewpoint (green line) in Celsius recorded by the NOXP scout from 0300 to 0630 UTC. Note that the NOXP scout was mobile between 0300 and 0345 UTC but was stationary after 0345 UTC.

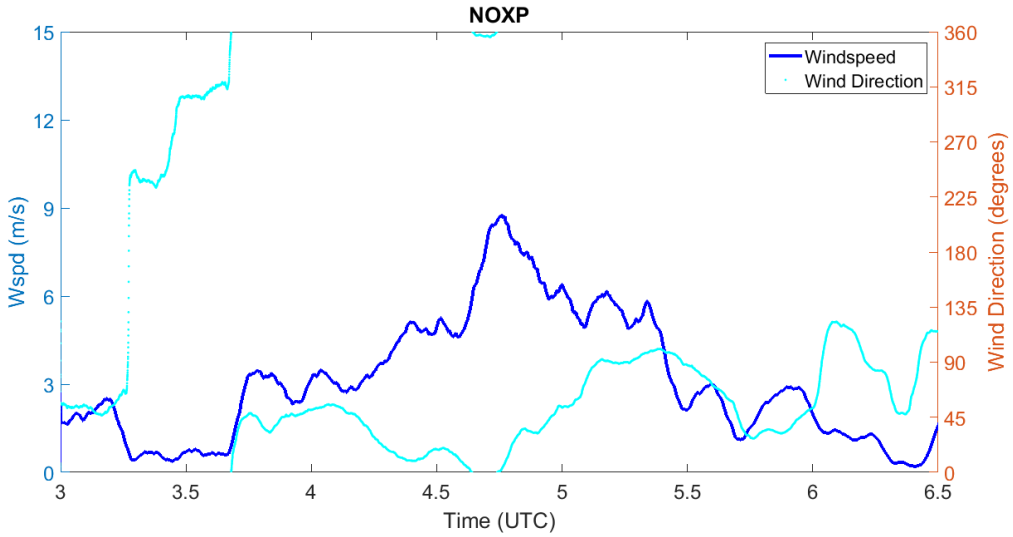

Figure 46. Windspeed (dark blue line) in meters per second and wind direction (light blue dots) in degrees recorded by the NOXP scout from 0300 to 0630 UTC. Note that the NOXP scout was mobile between 0300 and 0345 UTC but was stationary after 0345 UTC.

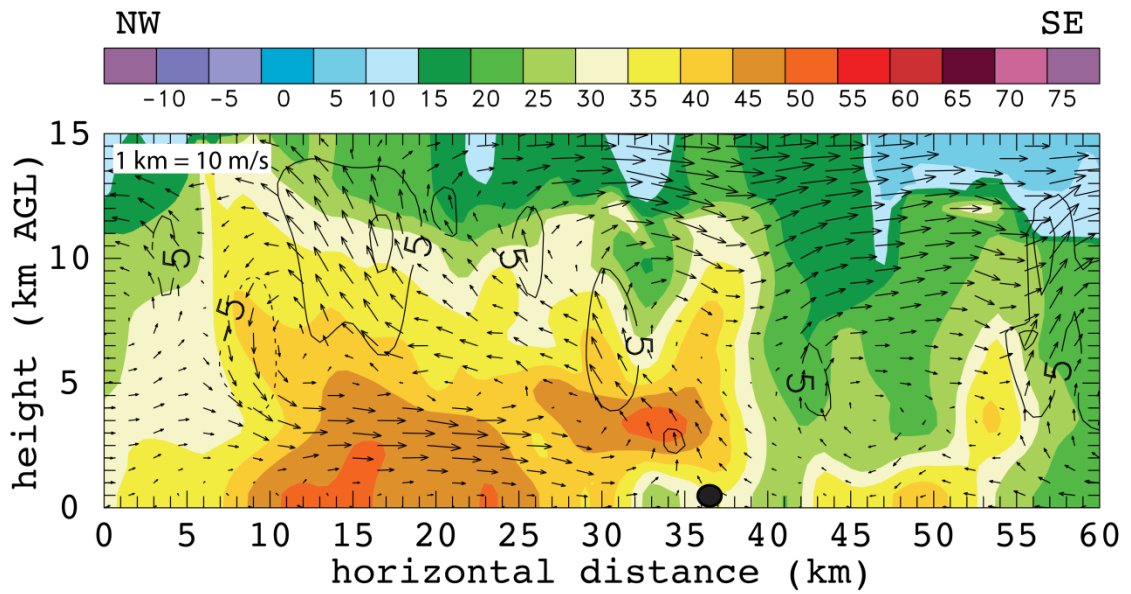

Figure 47. Northwest to southeast vertical cross section of radar analysis at 0440 UTC centered over NOXP (black dot). dBZ values color-filled and wind vectors plotted with black contours every 5 m/s, solid lines indicated positive w and dashed lines indicate negative w. 5 radars contributed to this analysis: SR1, SR2, NOXP, Dow7, and KTWX. Scaling factor for wind vectors is located in the upper left corner.

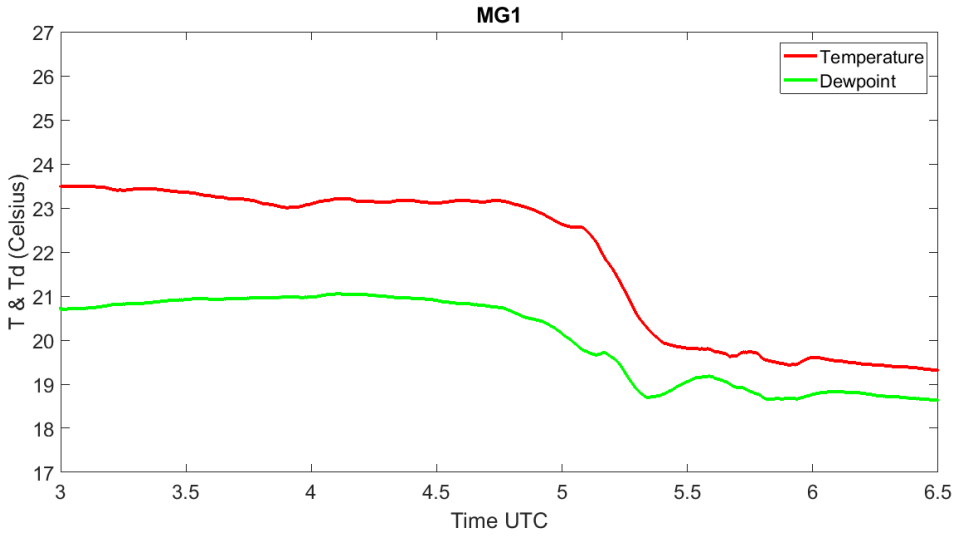

Figure 48. Temperature (red line) and dewpoint (green line) in Celsius recorded by MG1 from 0300 to 0630 UTC. Note that MG1 was co-located with Dow7.

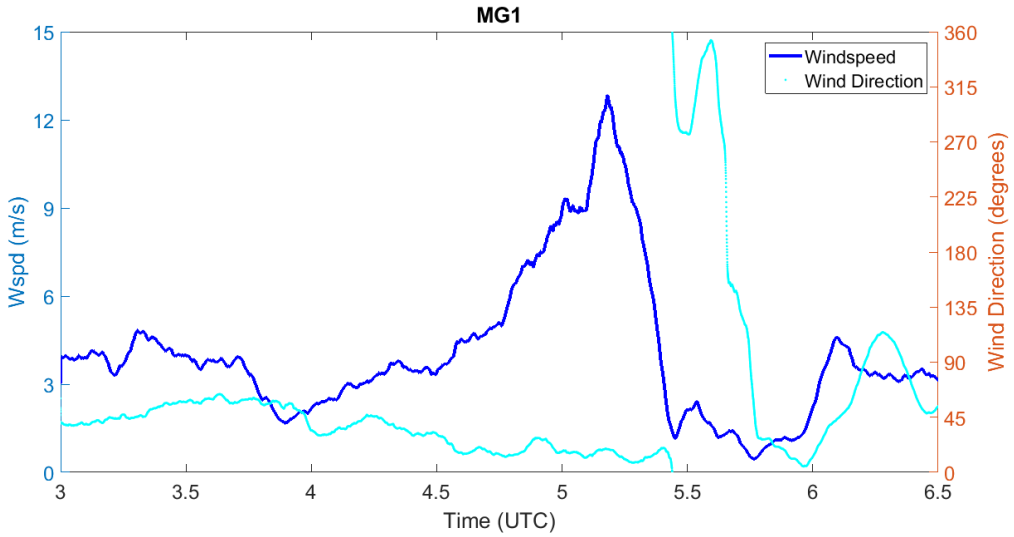

Figure 49. Windspeed (dark blue line) in meters per second and wind direction (light blue dots) in degrees recorded by MG1 from 0300 to 0630 UTC. Note that MG1 was co-located with Dow7.

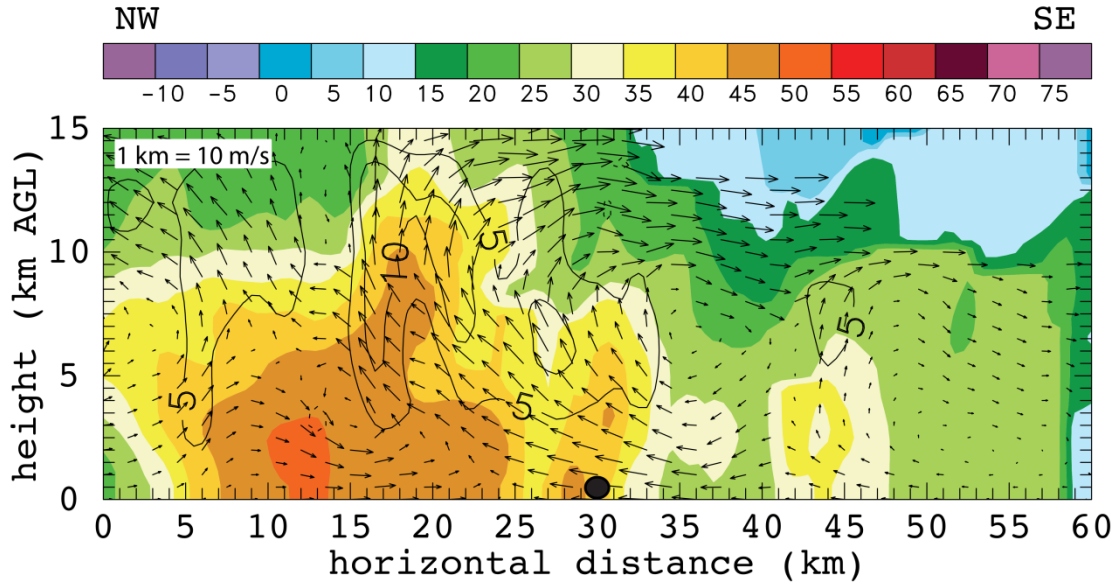

Figure 50. Northwest to southeast vertical cross section of radar analysis at 0510 UTC centered over MG1 (black dot). dBZ values color-filled and wind vectors plotted with black contours every 5 m/s, solid lines indicated positive w and dashed lines indicate negative w. 7 radars contributed to this analysis: SR1, SR2, NOXP, Dow7, Dow6, Dow8, and KTWX. Scaling factor for wind vectors is located in the upper left corner.

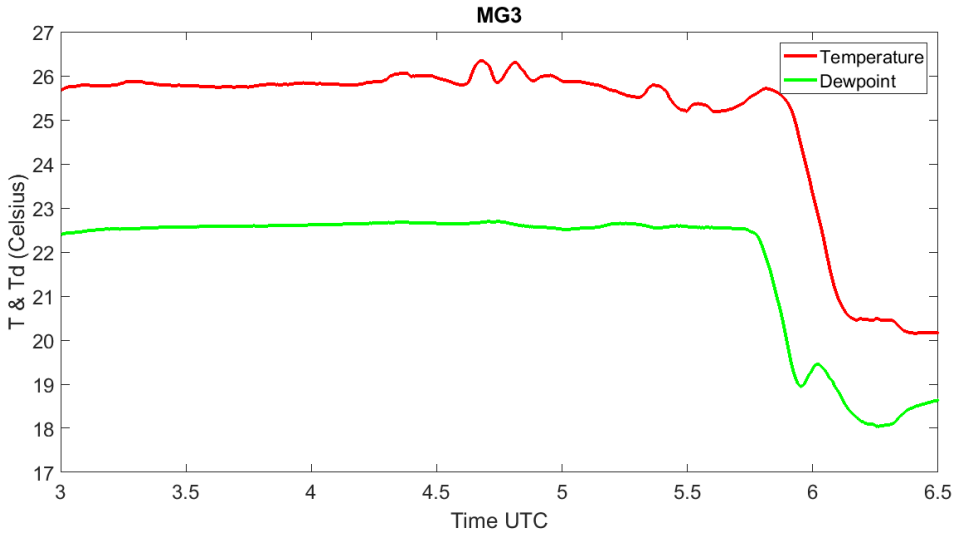

Figure 51. Temperature (red line) and dewpoint (green line) in Celsius recorded by MG3 from 0300 to 0630 UTC. Note that MG3 was located south of the radar analysis domain.

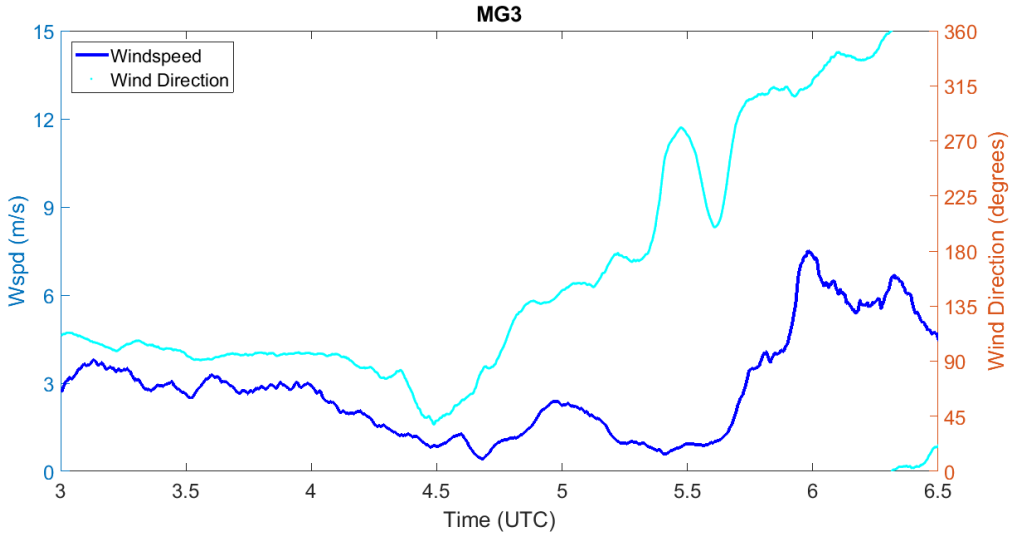

Figure 52. Windspeed (dark blue line) in meters per second and wind direction (light blue dots) in degrees recorded by MG3 from 0300 to 0630 UTC. Note that MG3 was located south of the radar analysis domain.

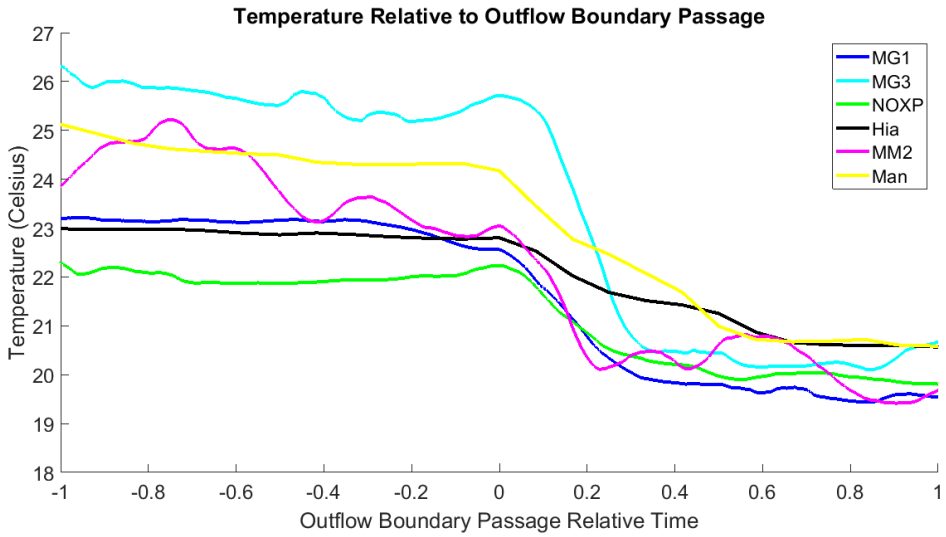

Figure 53. Temperature (Celsius) one hour before outflow boundary passage and one hour after outflow boundary passage with 0 being the time of outflow boundary passage for each platform that experienced a temperature drop. Lines are plotted for MG1 (dark blue), MG3 (light blue), NOXP (green), Hiawatha (black), MM2 (magenta), and Manhattan (yellow).

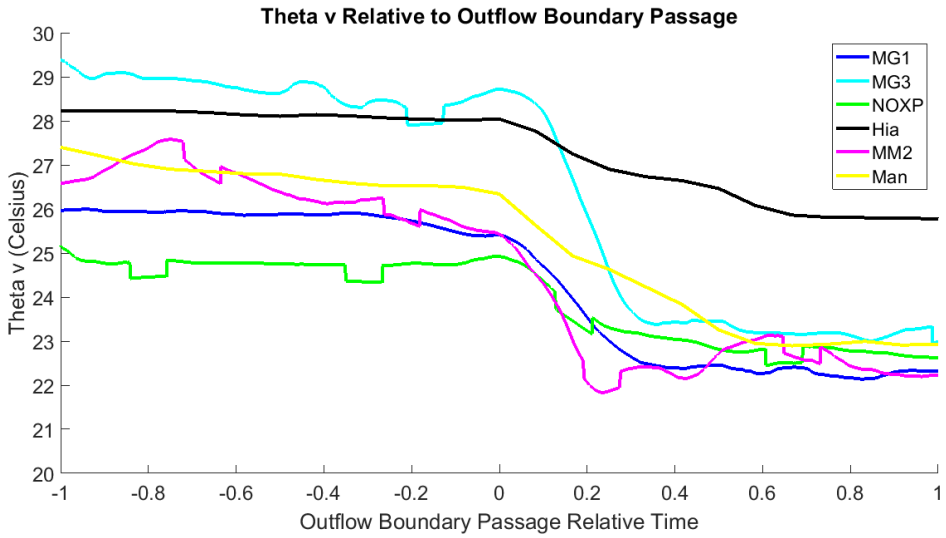

Figure 54. Theta-v (Celsius) one hour before outflow boundary passage and one hour after outflow boundary passage with 0 being the time of outflow boundary passage for each platform that experienced a temperature drop. Lines are plotted for MG1 (dark blue), MG3 (light blue), NOXP (green), Hiawatha (black), MM2 (magenta), and Manhattan (yellow).

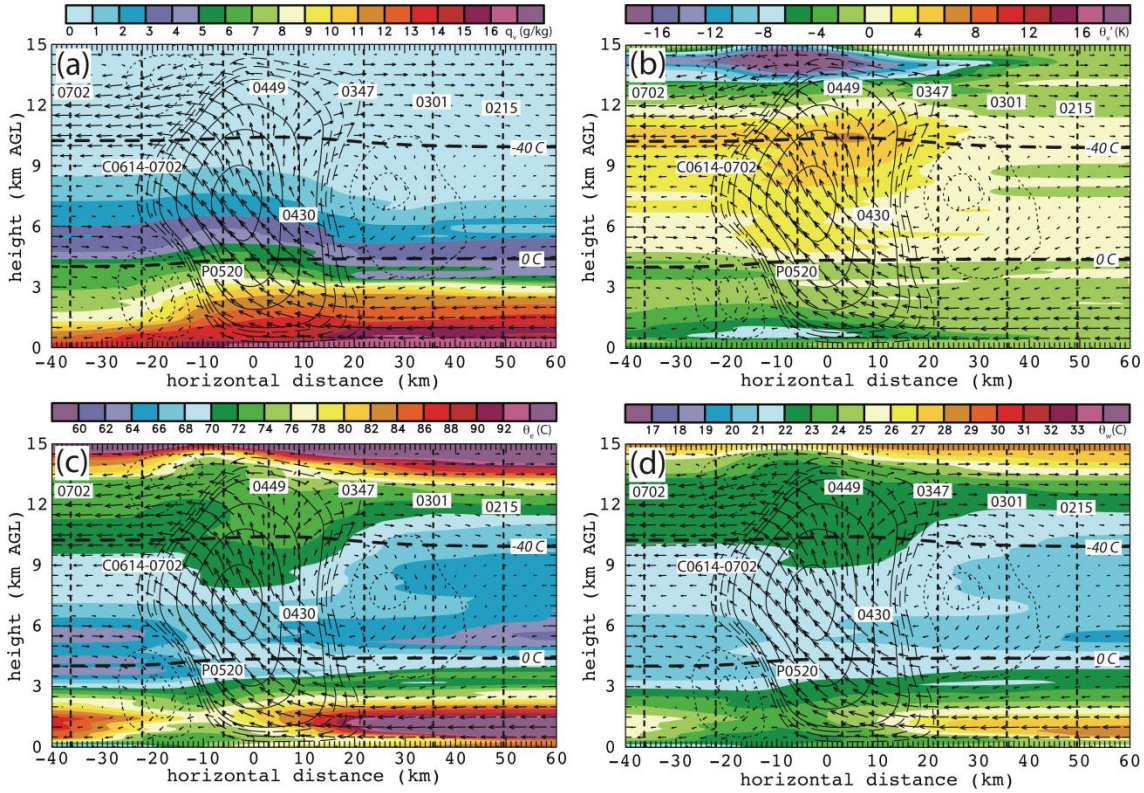

Figure 55. Sounding analysis through MG1 and MG2 location to see changes in environment due to MCS passage. Contours are as follows: solid line is for 1 and above with 1 m/s intervals, the long dash is from 0.25 to 0.75 m/s with 0.25 m/s intervals, and the dotted line is from -2 to -.5 m/s at 0.5 m/s intervals,. The four panels show a) water vapor mixing ratio b) theta-v' c) theta e d) theta w. X=0 km indicates the location of the outflow boundary passage with distance calculated by assuming an MCS speed of 5 m/s. Individual soundings are indicated by vertical dashed lines and are labeled with the time of launch. P0520 is a sounding generated by the DLA since there was no sounding launched in the convective line. C0614-0702 is the sounding launched at 0614 UTC that terminated early so the upper levels of 0702 UTC were added to the top to make a full sounding.

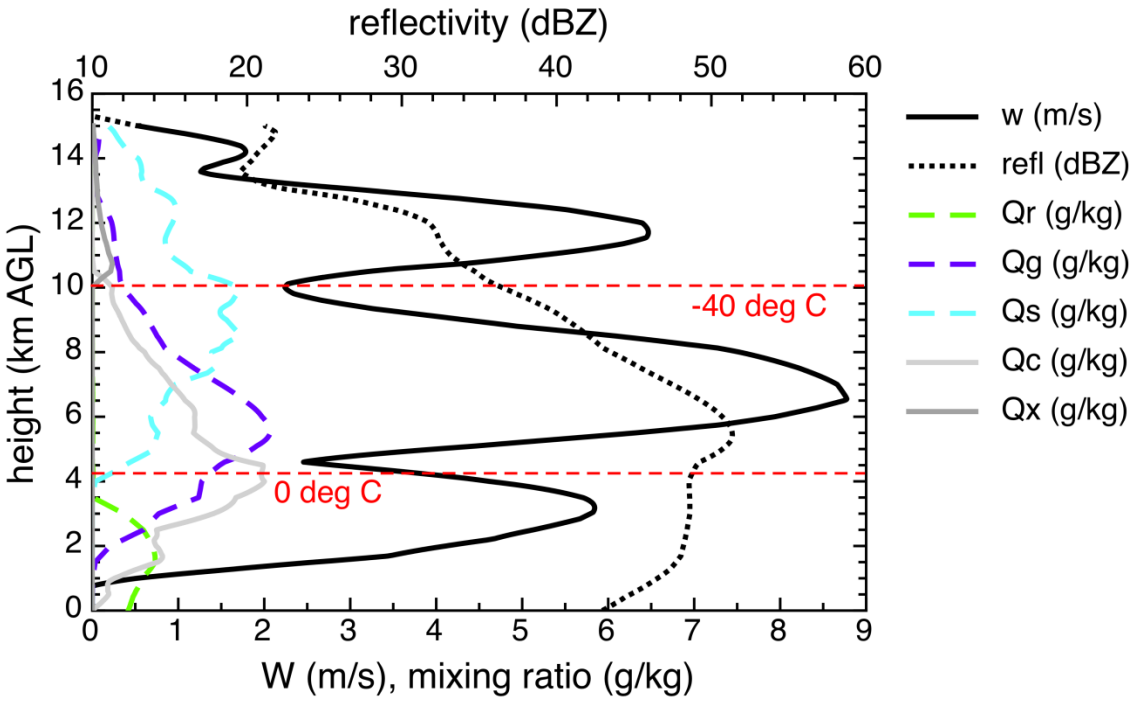

Figure 56. 0520 sounding generated from DLA output in convective line of MCS which was used to generate figure 54. W (black line), reflectivity (dotted black line), rain mixing ratio (green dashed line), graupel mixing ratio (purple dashed line), snow mixing ratio (blue dashed line), cloud water mixing ratio (light gray line), and cloud ice mixing ratio (dark gray line) are plotted along with dashed red lines to indicate the 0° C and -40° C isotherms.

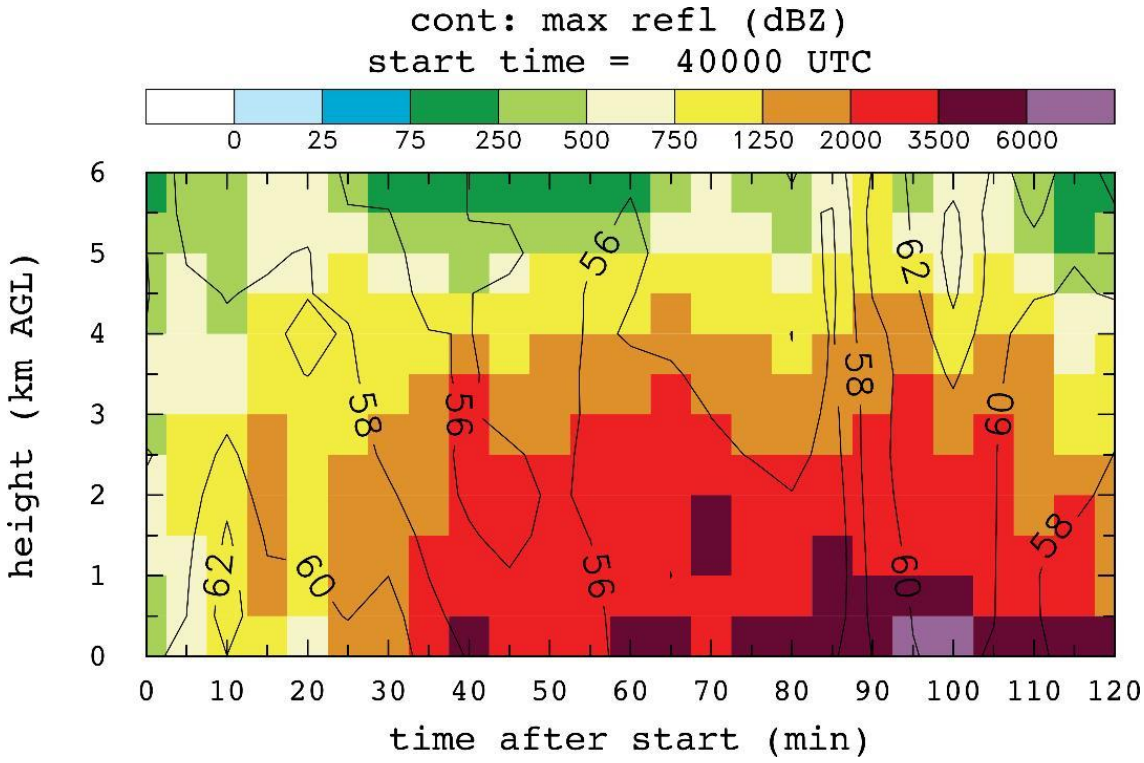

Figure 57. Updraft trajectory origins from 0400 to 0600 UTC. Trajectories were counted as an updraft trajectory if it entered an updraft that was from 2.5-6 km in height, greater than or equal to 5 m/s, and had a reflectivity value greater than 35 dBZ. These thresholds ensured that the updraft would be located in a convective core and that the trajectories would be representative of updrafts in the leading line.

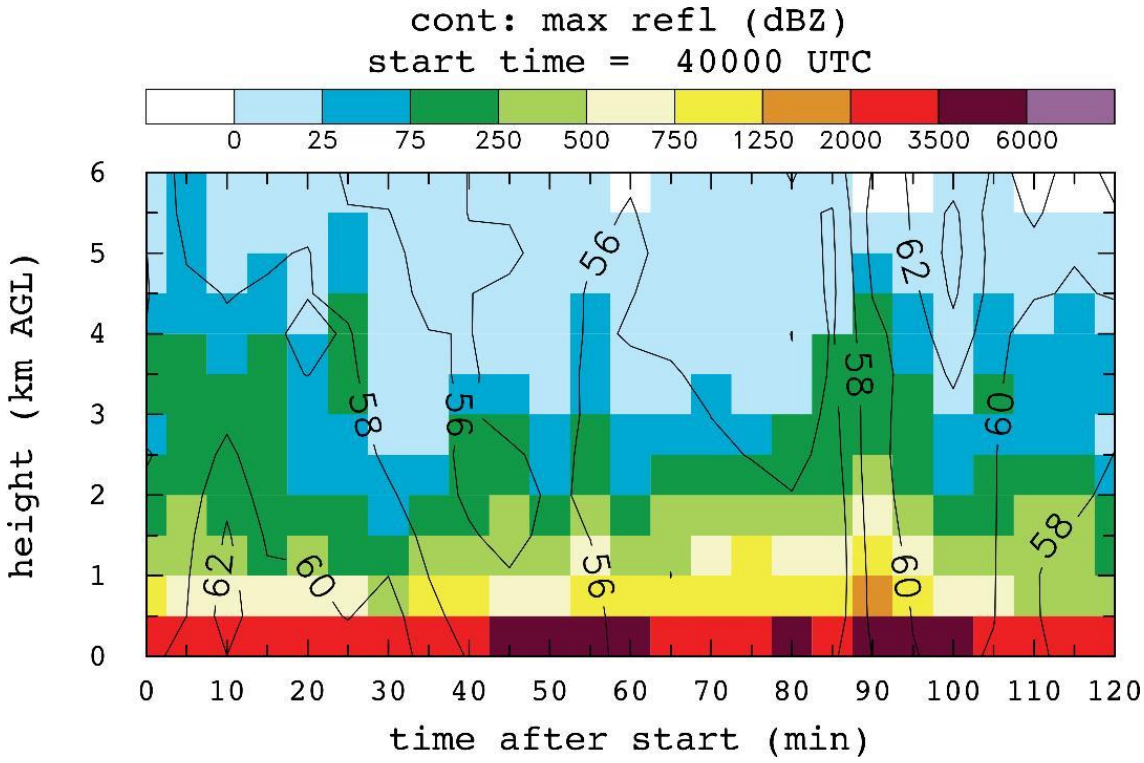

Figure 58. Downdraft trajectory origin from 0400 to 0600 UTC. In order for a trajectory to be counted, the downdraft it entered had to have a final height at or below 500 m, be less than or equal to -0.5 m/s at 0.5 km, be less than -0.1 m/s at 0 km, and the reflectivity value at the downdraft point had to be greater than 20 dBZ.

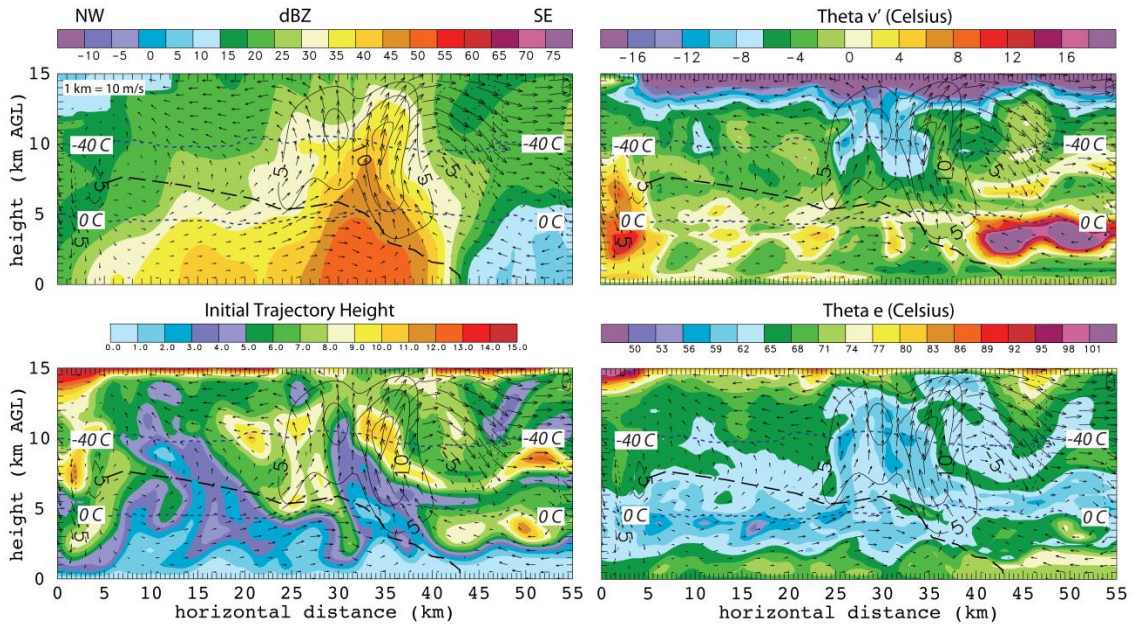

Figure 59. DLA output for the same vertical cross section as shown in figure 13 at 0400 UTC. The four panels show a) reflectivity b) theta-v' c) initial trajectory height d) theta e. Dashed blue lines indicate the 0° and -40° C isotherm. The dashed black line shows the interface between the RTF and FTR flow and the black contours indicate w like in figure 13.

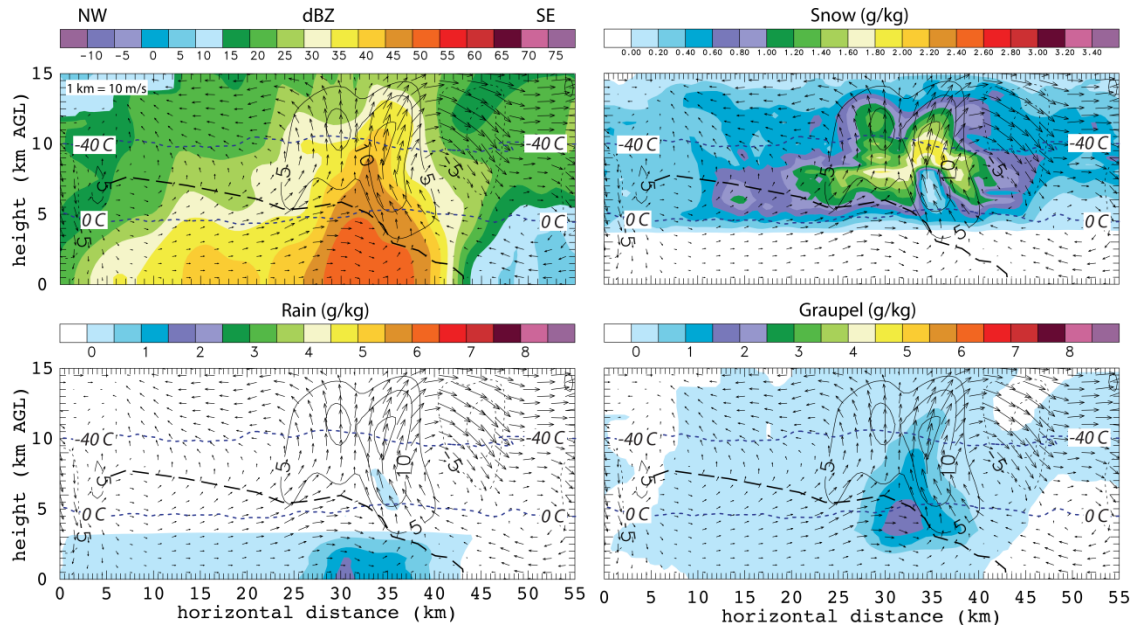

Figure 60. DLA output for the same vertical cross section as shown in figure 13 at 0400 UTC. The four panels show a) reflectivity b) snow mixing ratio c) rain mixing ratio d) graupel mixing ratio. Dashed blue lines indicate the 0° and -40° C

isotherm. The dashed black line shows the interface between the RTF and FTR flow and the black contours indicate w like in figure 13.

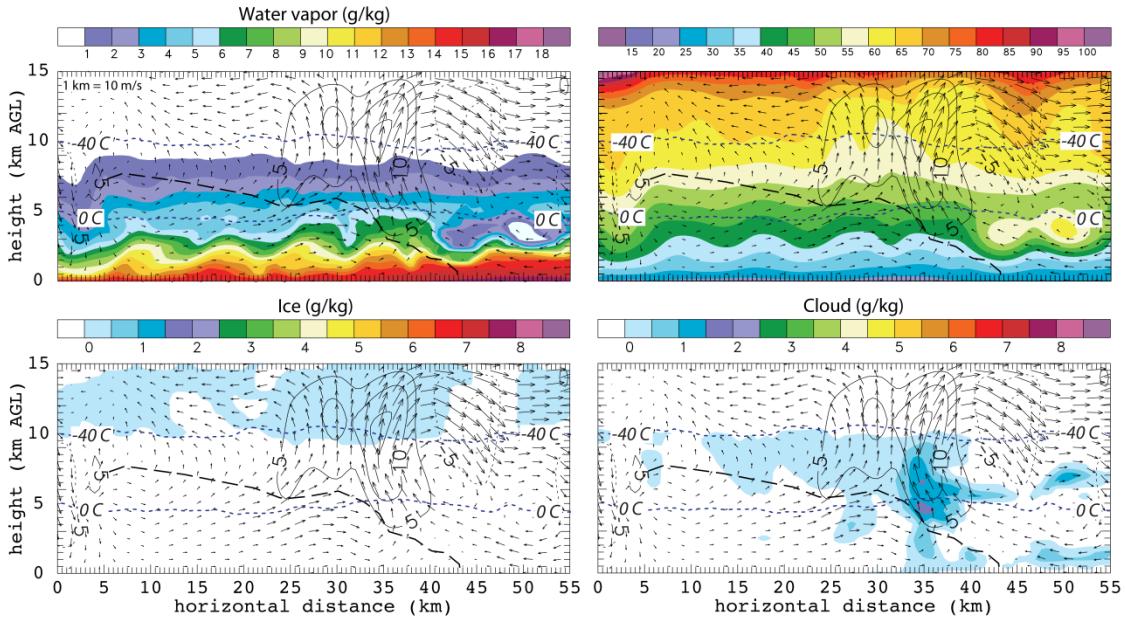

Figure 61. DLA output for the same vertical cross section as shown in figure 13 at 0400 UTC. The four panels show a) water vapor b) theta c) cloud ice mixing ratio d) cloud water mixing ratio. Dashed blue lines indicate the 0° and -40° C isotherm. The dashed black line shows the interface between the RTF and FTR flow and the black contours indicate w like in figure 13.

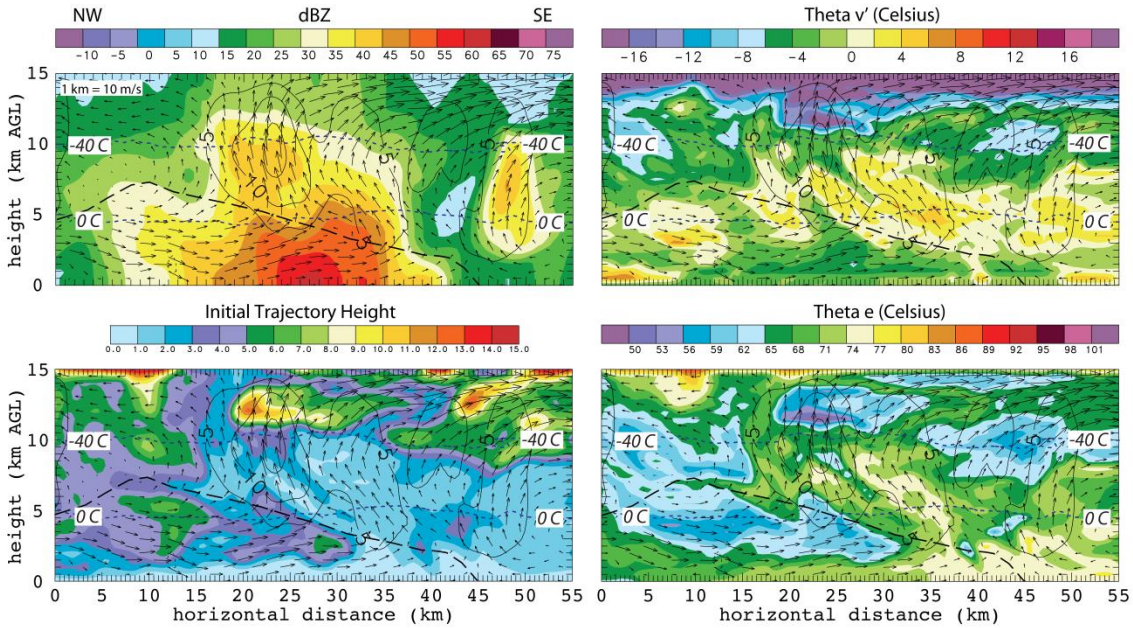

Figure 62. DLA output for the same vertical cross section as shown in figure 16 at 0430 UTC. The four panels show a) reflectivity b) theta-v' c) initial trajectory height d) theta e. Dashed blue lines indicate the 0° and -40° C isotherm. The dashed black line shows the interface between the RTF and FTR flow and the black contours indicate w like in figure 16.

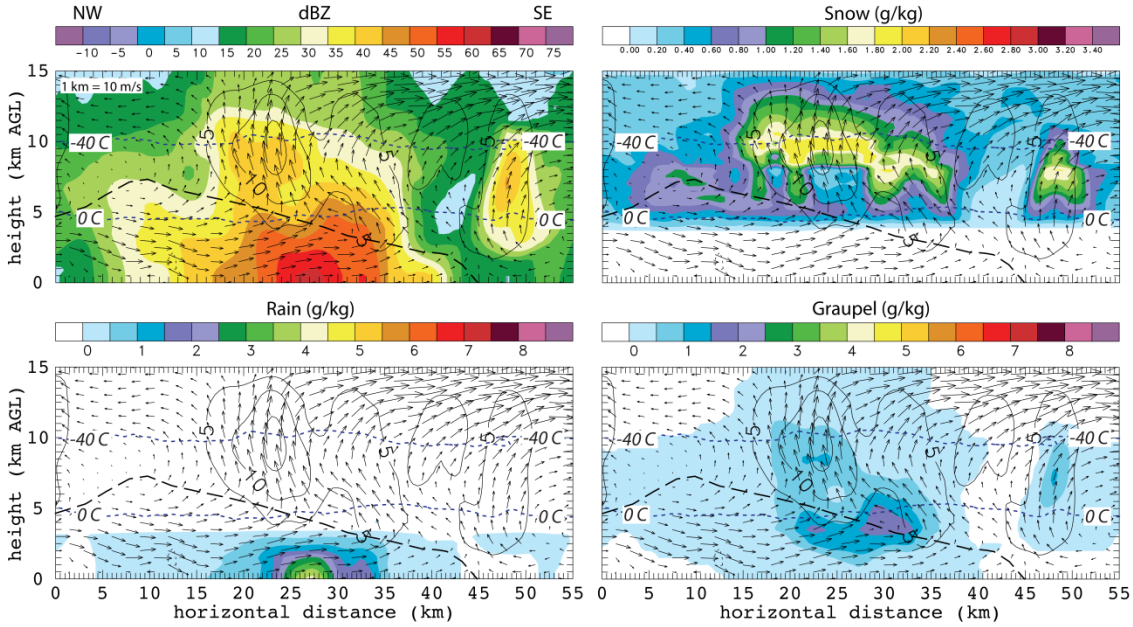

Figure 63. DLA output for the same vertical cross section as shown in figure 16 at 0430 UTC. The four panels show a) reflectivity b) snow mixing ratio c) rain mixing ratio d) graupel mixing ratio. Dashed blue lines indicate the 0° and -40° C

isotherm. The dashed black line shows the interface between the RTF and FTR flow and the black contours indicate w like in figure 16.

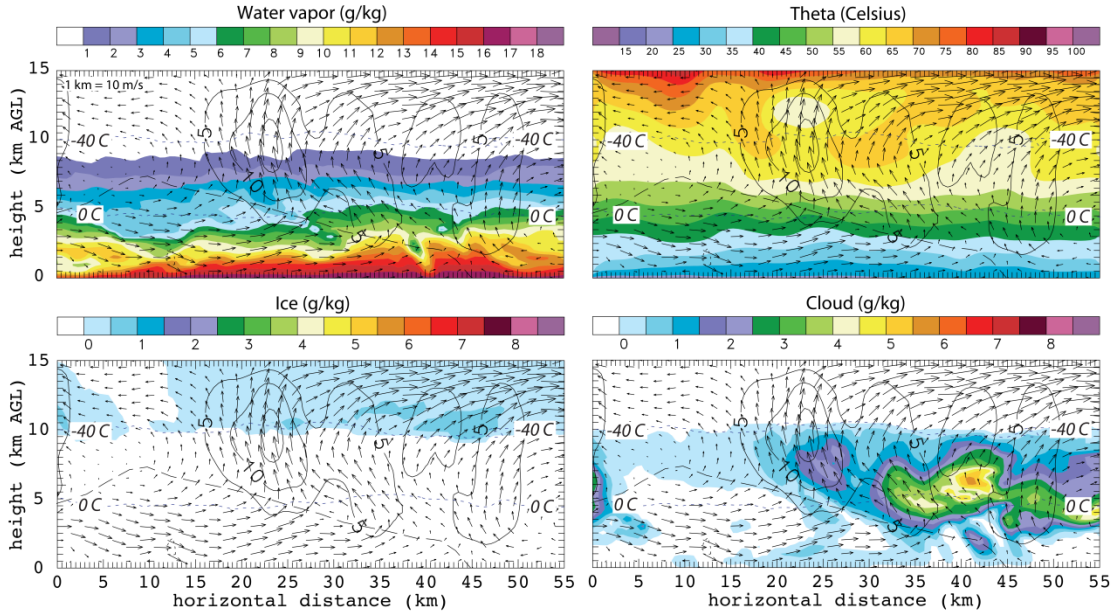

Figure 64. DLA output for the same vertical cross section as shown in figure 16 at 0430 UTC. The four panels show a) water vapor b) theta c) cloud ice mixing ratio d) cloud water mixing ratio. Dashed blue lines indicate the 0° and -40° C isotherm. The dashed black line shows the interface between the RTF and FTR flow and the black contours indicate w like in figure 16.

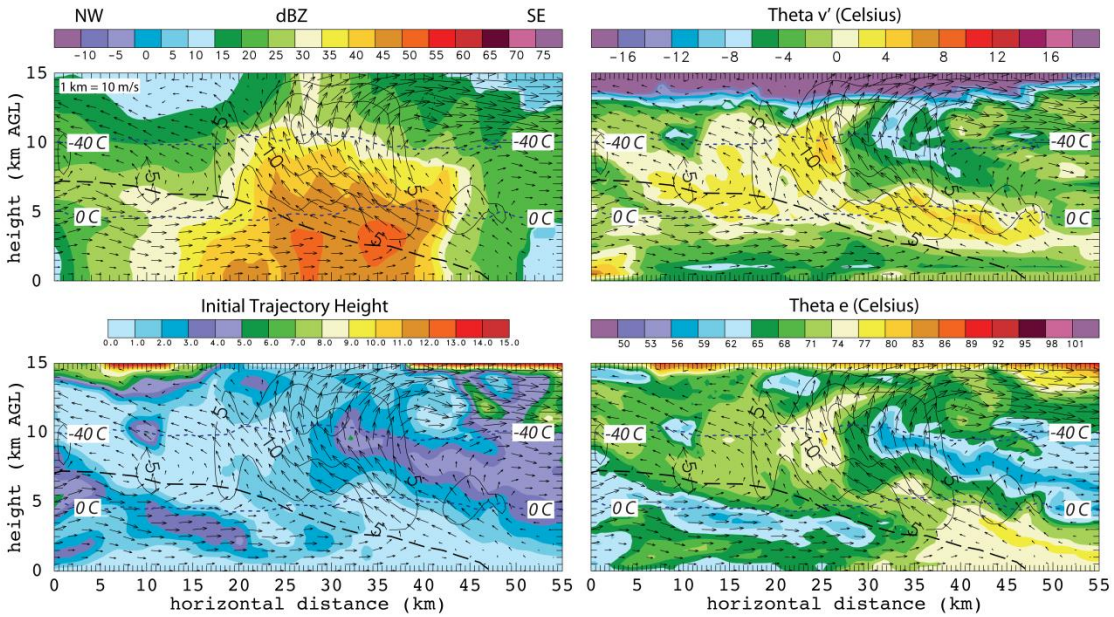

Figure 65. DLA output for the same vertical cross section as shown in figure 19 at 0500 UTC. The four panels show a) reflectivity b) theta-v' c) initial trajectory height d) theta e. Dashed blue lines indicate the 0° and -40° C isotherm. The dashed black line shows the interface between the RTF and FTR flow and the black contours indicate w like in figure 19.

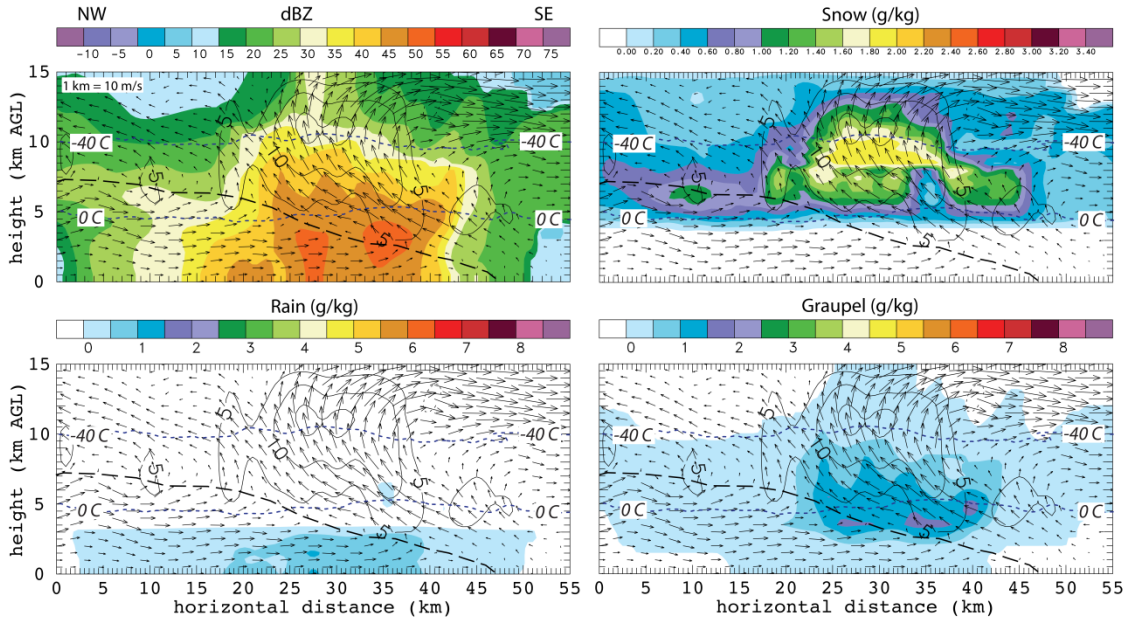

Figure 66. DLA output for the same vertical cross section as shown in figure 19 at 0500 UTC. The four panels show a) reflectivity b) snow mixing ratio c) rain mixing ratio d) graupel mixing ratio. Dashed blue lines indicate the 0° and -40° C

isotherm. The dashed black line shows the interface between the RTF and FTR flow and the black contours indicate w like in figure 19.

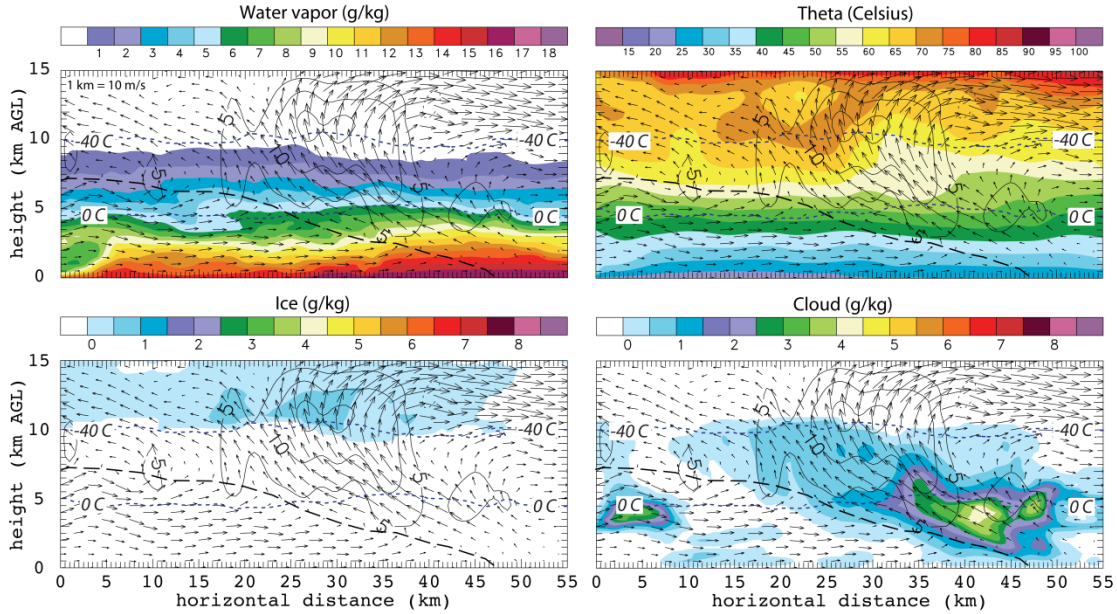

Figure 67. DLA output for the same vertical cross section as shown in figure 19 at 0500 UTC. The four panels show a) water vapor b) theta c) cloud ice mixing ratio d) cloud water mixing ratio. Dashed blue lines indicate the 0° and -40° C isotherm. The dashed black line shows the interface between the RTF and FTR flow and the black contours indicate w like in figure 19.

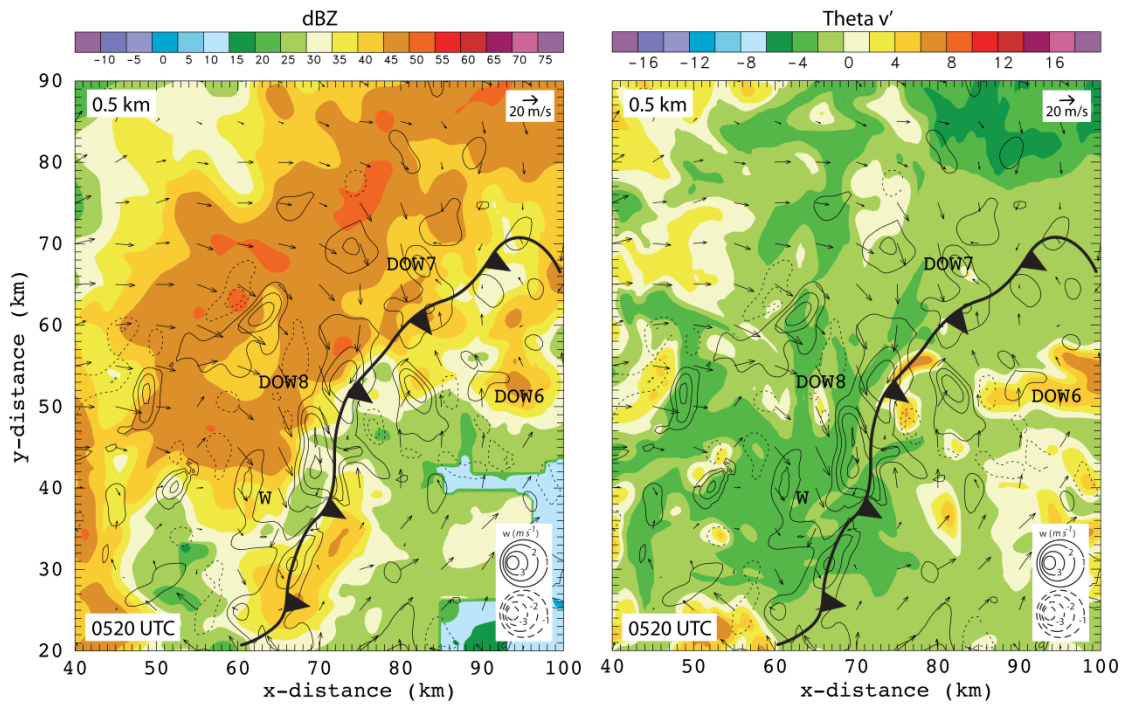

Figure 68. Reflectivity from the 0520 UTC radar analysis with the DLA output of theta v' at 0.5 km. Scaling for wind vectors and w contour legend are located in the upper right corner and lower right corner respectively. The wind report is located at the "W". The black line indicates the leading edge of the outflow boundary.

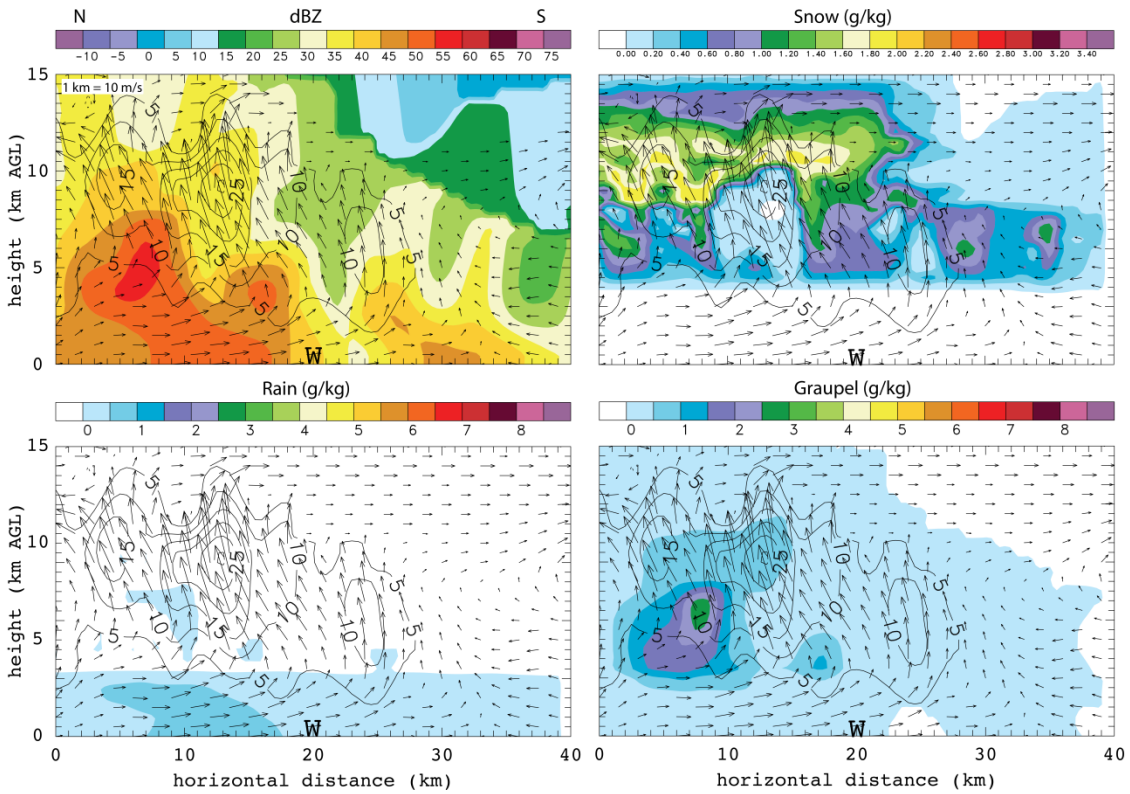

Figure 69. DLA output for the same vertical cross section as shown in figure 22 at 0520 UTC. The four panels show a) reflectivity b) snow mixing ratio c) rain mixing ratio d) graupel mixing ratio. Dashed blue lines indicate the 0° and -40° C isotherm. The dashed black line shows the interface between the RTF and FTR flow and the black contours indicate w like in figure 22. The wind report is denoted by the "W" at 20 km.

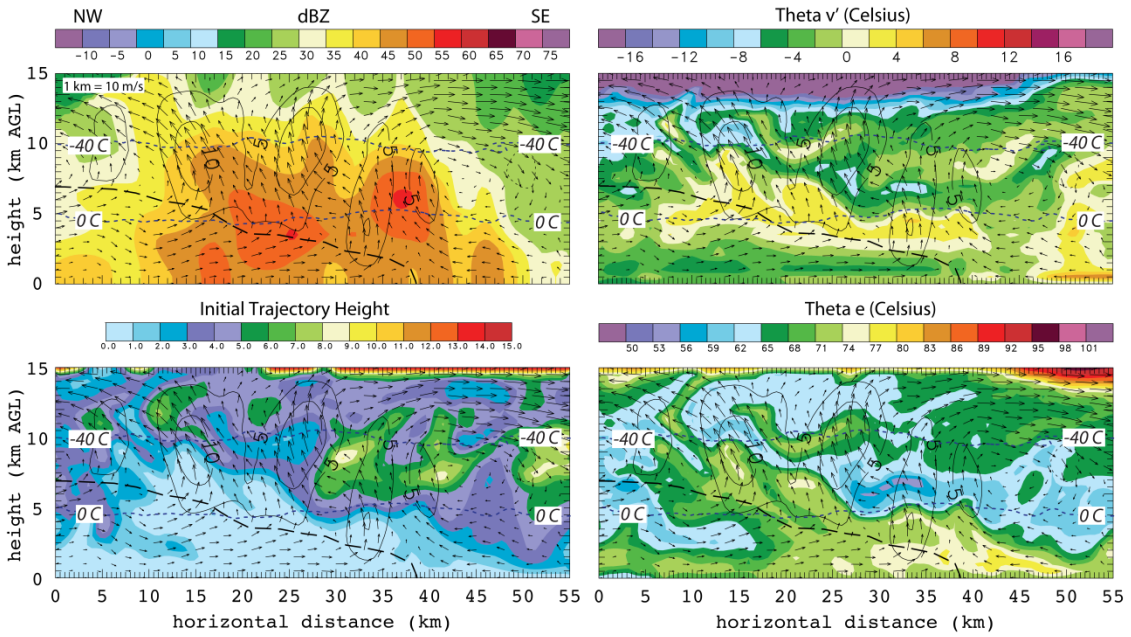

Figure 70. DLA output for the same vertical cross section as shown in figure 26 at 0530 UTC. The four panels show a) reflectivity b) theta-v' c) initial trajectory height d) theta e. Dashed blue lines indicate the 0° and -40° C isotherm. The dashed black line shows the interface between the RTF and FTR flow and the black contours indicate w like in figure 26.

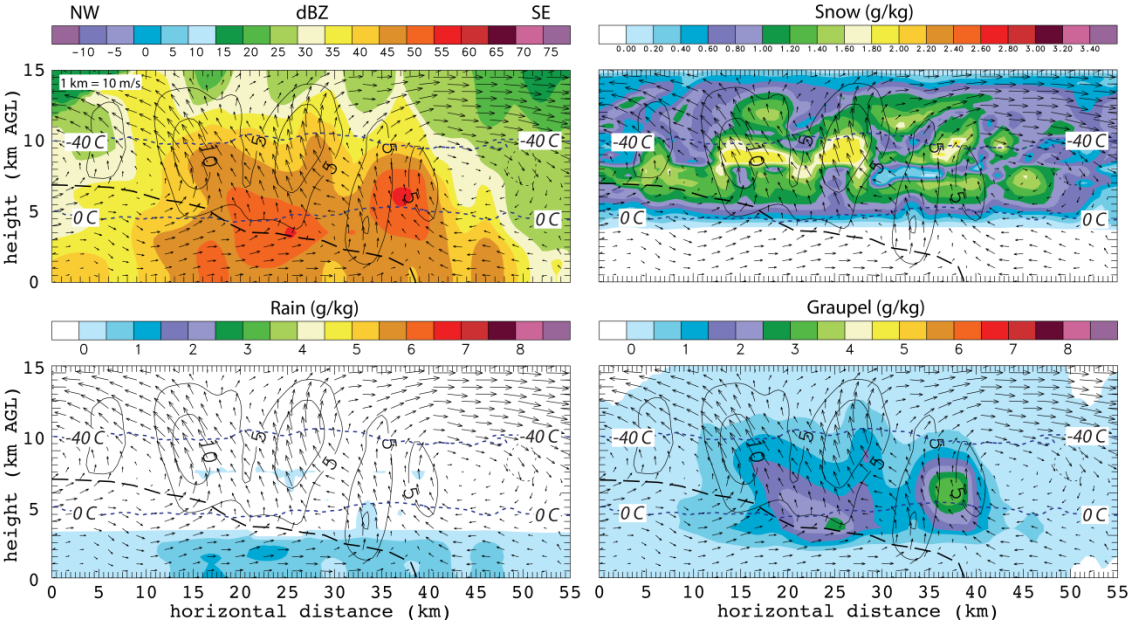

Figure 71. DLA output for the same vertical cross section as shown in figure 26 at 0530 UTC. The four panels show a) reflectivity b) snow mixing ratio c) rain mixing ratio d) graupel mixing ratio. Dashed blue lines indicate the 0° and -40° C

isotherm. The dashed black line shows the interface between the RTF and FTR flow and the black contours indicate w like in figure 26.

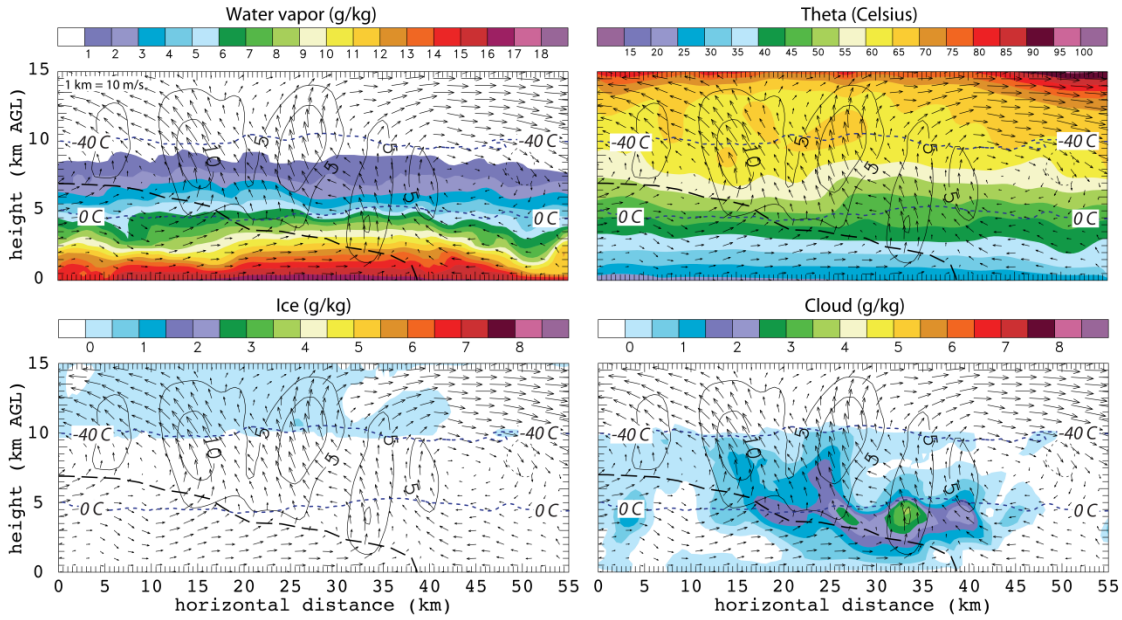

Figure 72. DLA output for the same vertical cross section as shown in figure 26 at 0530 UTC. The four panels show a) water vapor b) theta c) cloud ice mixing ratio d) cloud water mixing ratio. Dashed blue lines indicate the 0° and -40° C isotherm. The dashed black line shows the interface between the RTF and FTR flow and the black contours indicate w like in figure 26.

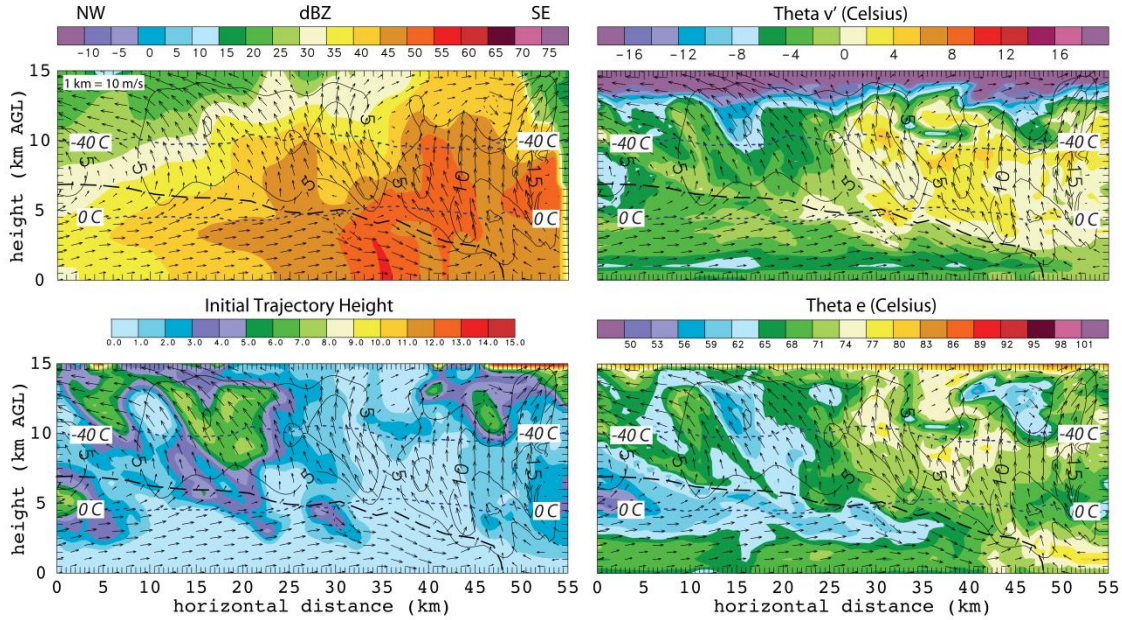

Figure 73. DLA output for the same vertical cross section as shown in figure 29 at 0600 UTC. The four panels show a) reflectivity b) theta-v' c) initial trajectory

height d) theta e. Dashed blue lines indicate the 0° and -40° C isotherm. The dashed black line shows the interface between the RTF and FTR flow and the black contours indicate w like in figure 29.

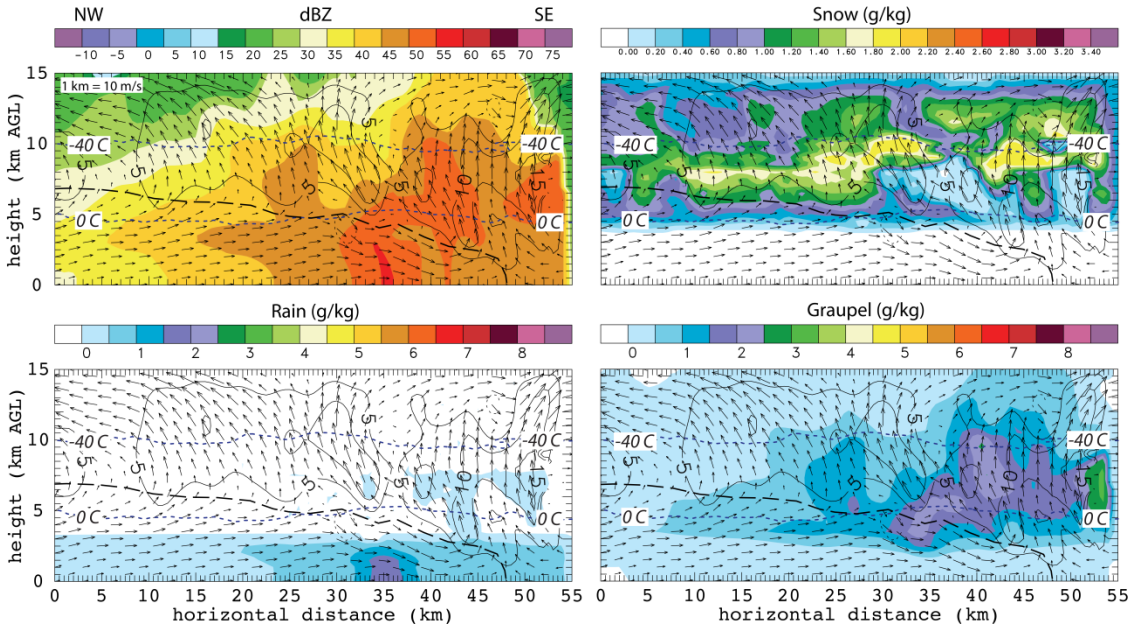

Figure 74. DLA output for the same vertical cross section as shown in figure 29 at 0600 UTC. The four panels show a) reflectivity b) snow mixing ratio c) rain mixing ratio d) graupel mixing ratio. Dashed blue lines indicate the 0° and -40° C isotherm. The dashed black line shows the interface between the RTF and FTR flow and the black contours indicate w like in figure 29.

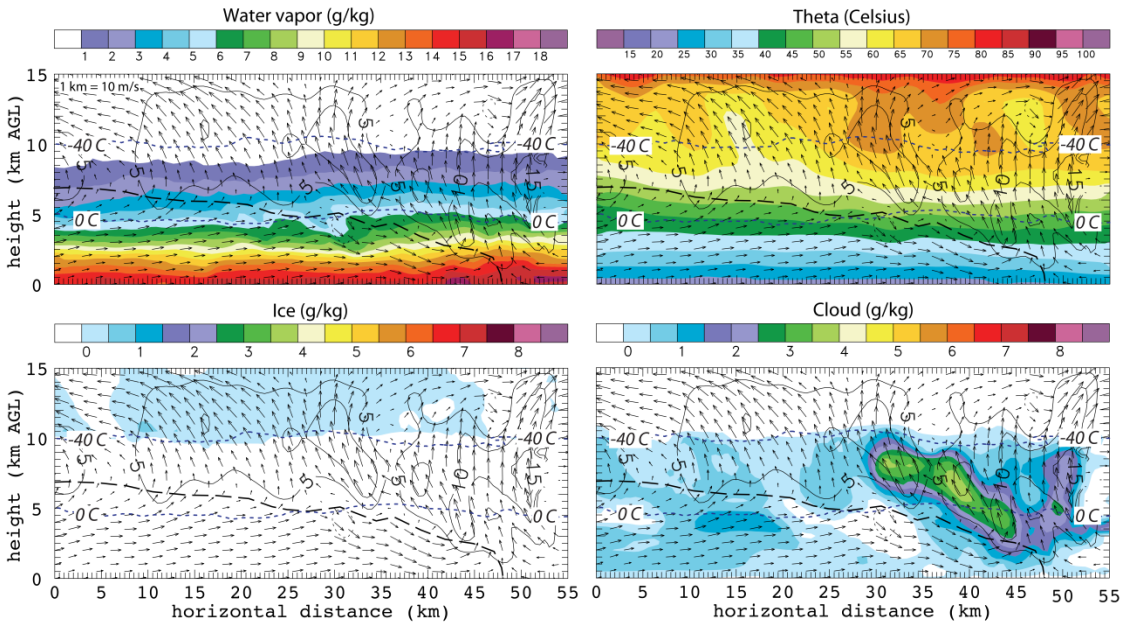

Figure 75. DLA output for the same vertical cross section as shown in figure 29 at 0600 UTC. The four panels show a) water vapor b) theta c) cloud ice mixing ratio d) cloud water mixing ratio. Dashed blue lines indicate the 0° and -40° C isotherm. The dashed black line shows the interface between the RTF and FTR flow and the black contours indicate w like in figure 29.

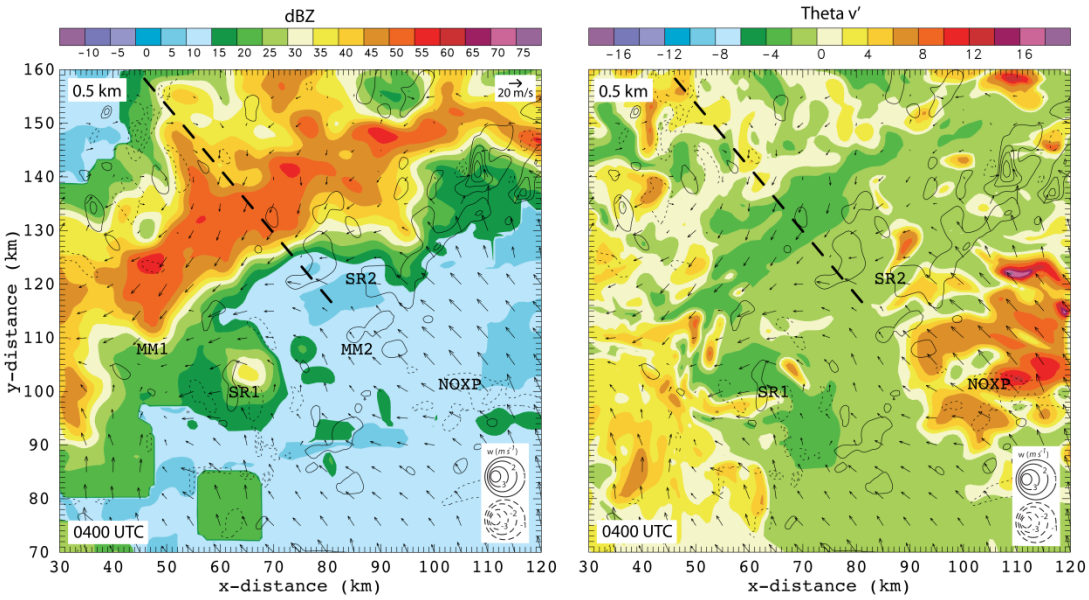

Figure 76. Reflectivity from the 0400 UTC radar analysis with the DLA output of theta v' at 0.5 km. Scaling for wind vectors and w contour legend are located in the upper right corner and lower right corner respectively. Dashed black line indiatces the location of the vertical cross section from figure 13.

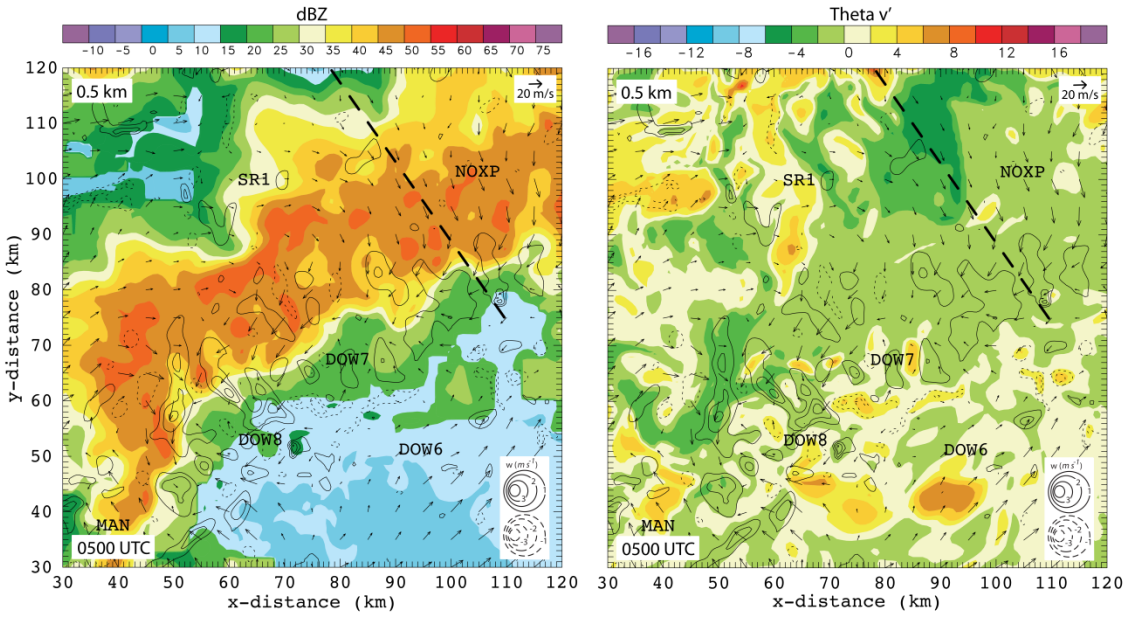

Figure 77. Reflectivity from the 0500 UTC radar analysis with the DLA output of theta v' at 0.5 km. Scaling for wind vectors and w contour legend are located in the upper right corner and lower right corner respectively. Dashed black line indiatces the location of the vertical cross section from figure 19.

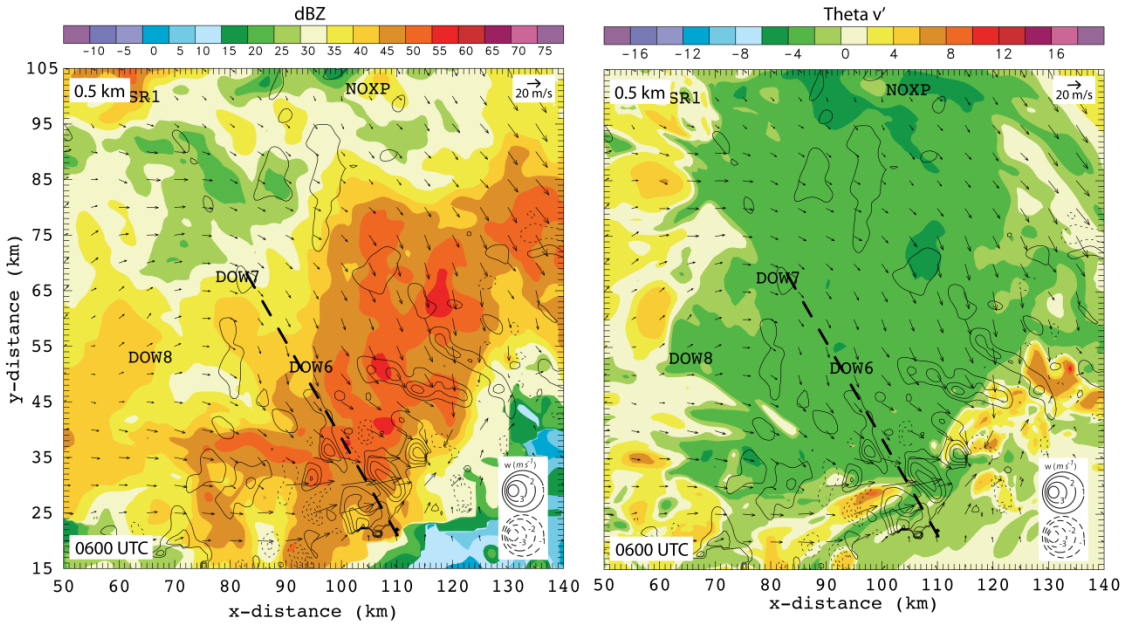

Figure 78. Reflectivity from the 0600 UTC radar analysis with the DLA output of theta v' at 0.5 km. Scaling for wind vectors and w contour legend are located in the

upper right corner and lower right corner respectively. Dashed black line indiatces the location of the vertical cross section from figure 29.

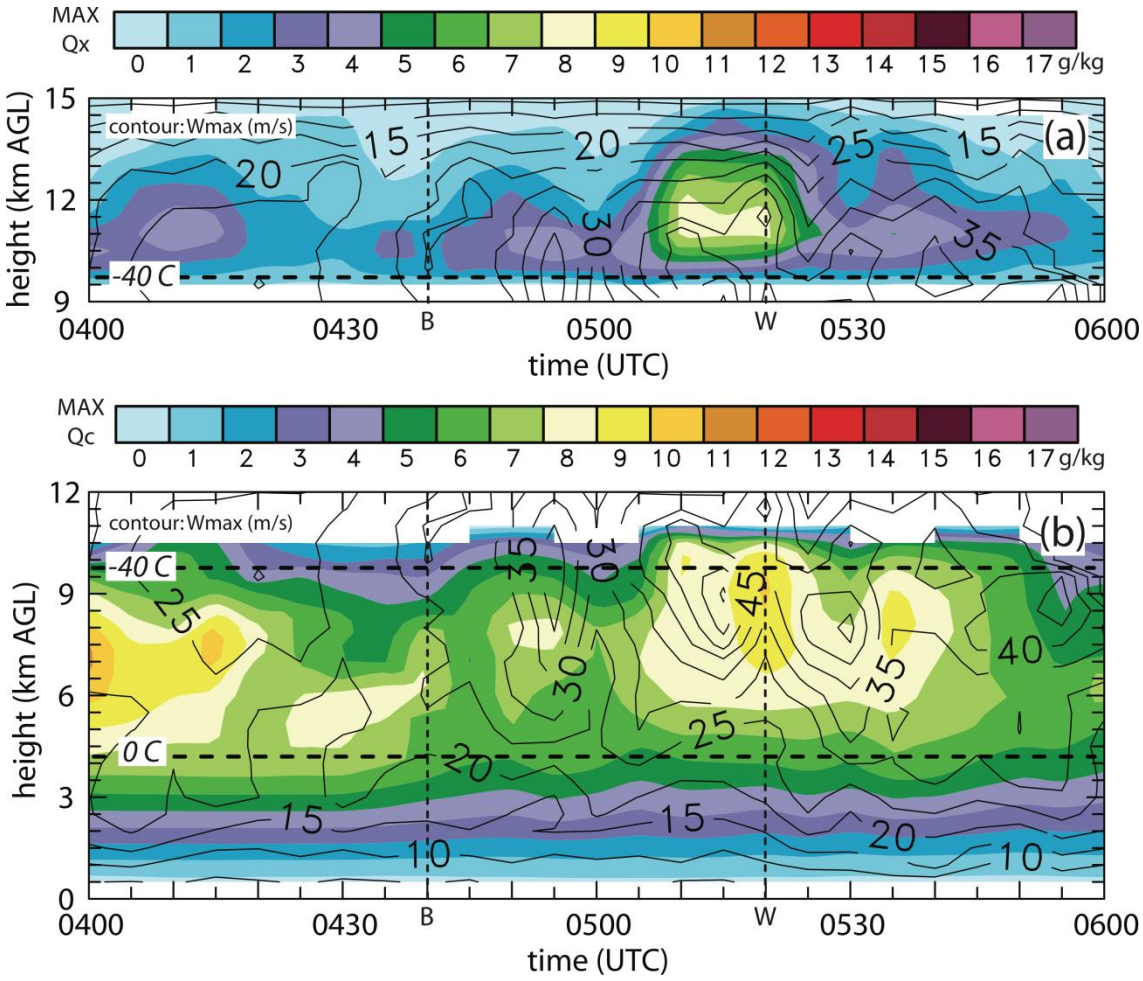

Figure 79. The two panels show color-filled integrated values of a) maximum cloud ice mixing ratio and b) maximum cloud water mixing ratio at each level and time for the entire DLA domain from 0400 to 0600 UTC. The contours overlaid in both figures are maximum w value. Similar to figure 35 the dashed line labeled "B" indicates the beginning of the outflow surge and the dashed line labeled "W" indicates the time of the wind report.

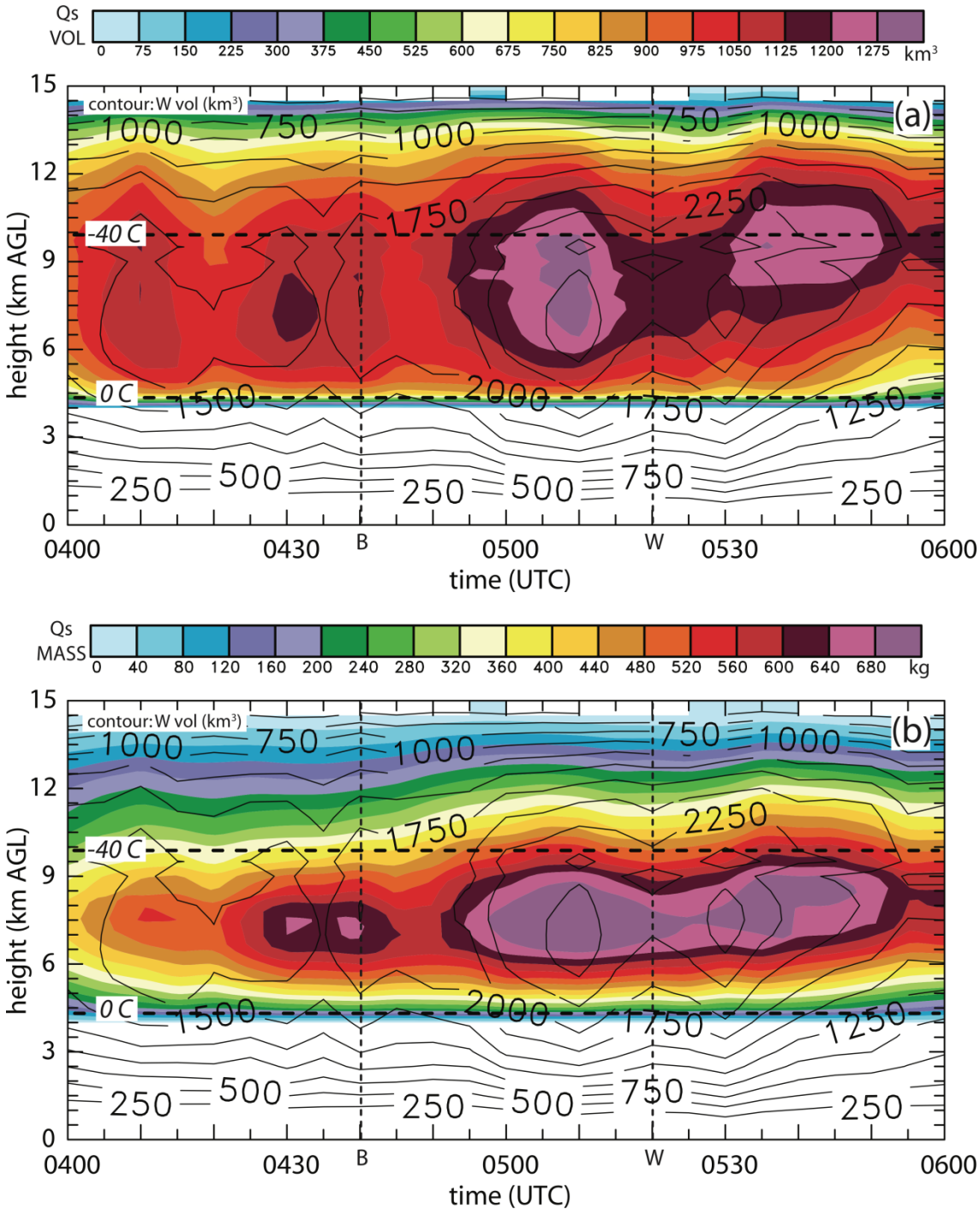

Figure 80. The two panels show color-filled integrated values of a) maximum snow volume and b) maximum snow mass based on horizontal layer integrals for the entire DLA domain from 0400 to 0600 UTC. The contours overlaid in both figures are maximum w value. Similar to figure 35 the dashed line labeled "B" indicates the beginning of the outflow surge and the dashed line labeled "W" indicates the time of the wind report.

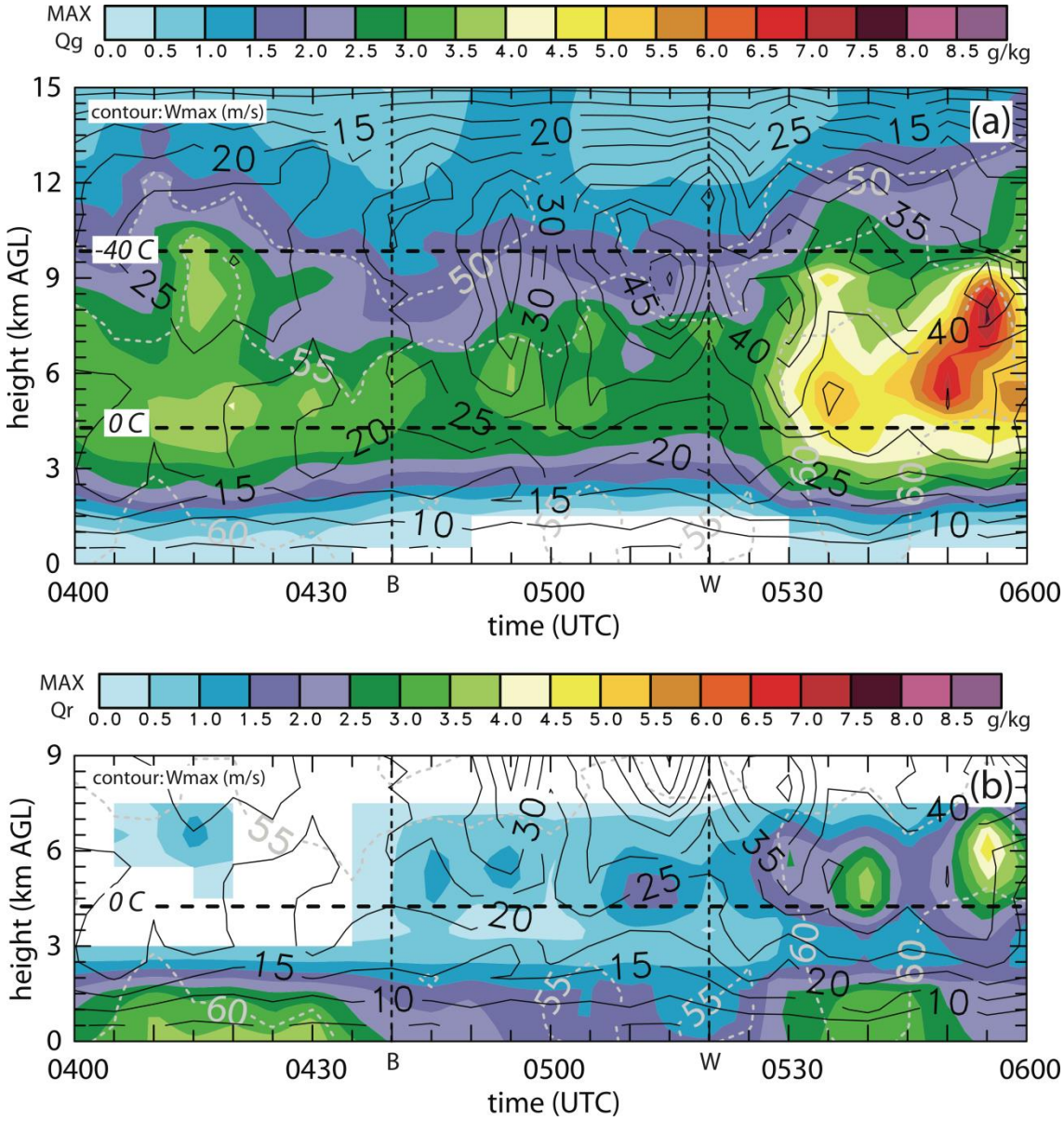

Figure 81. The two panels show color-filled integrated values of a) maximum graupel mixing ratio and b) maximum rain mixing ratio at each level and time for the entire DLA domain from 0400 to 0600 UTC. The contours overlaid in both figures are maximum w value. Similar to figure 35 the dashed line labeled "B" indicates the beginning of the outflow surge and the dashed line labeled "W" indicates the time of the wind report.

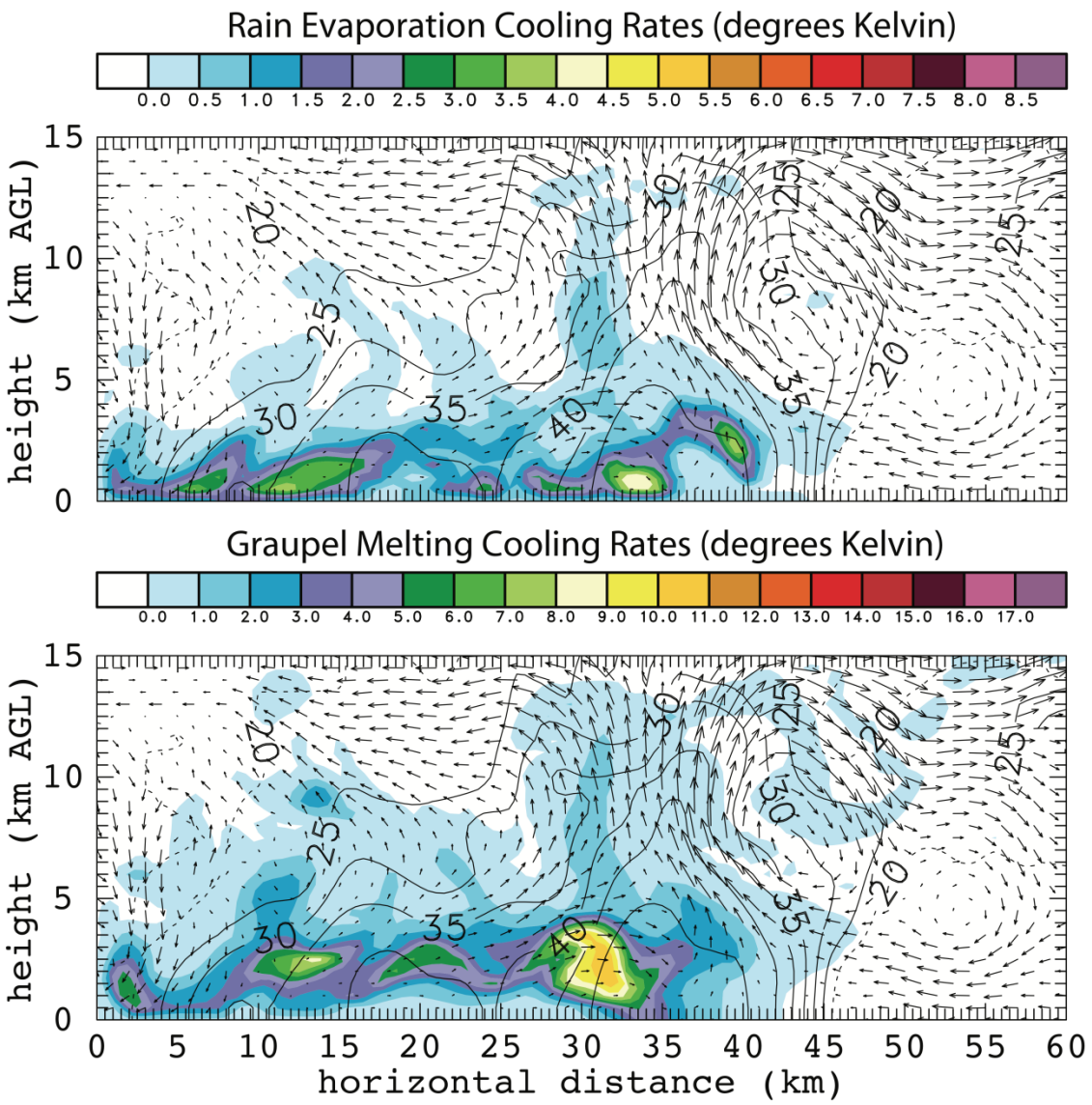

Figure 82. The two panels show color-filled integrated values of a) rain evaporation cooling rates and b) graupel melting cooling rates for the vertical cross section in figure 13 at 0400 UTC. The contours overlaid in both figures are w, the same as in figure 13. These cooling rates are in degrees Kelvin and represent the total cooling along the trajectory up until 0400 UTC.

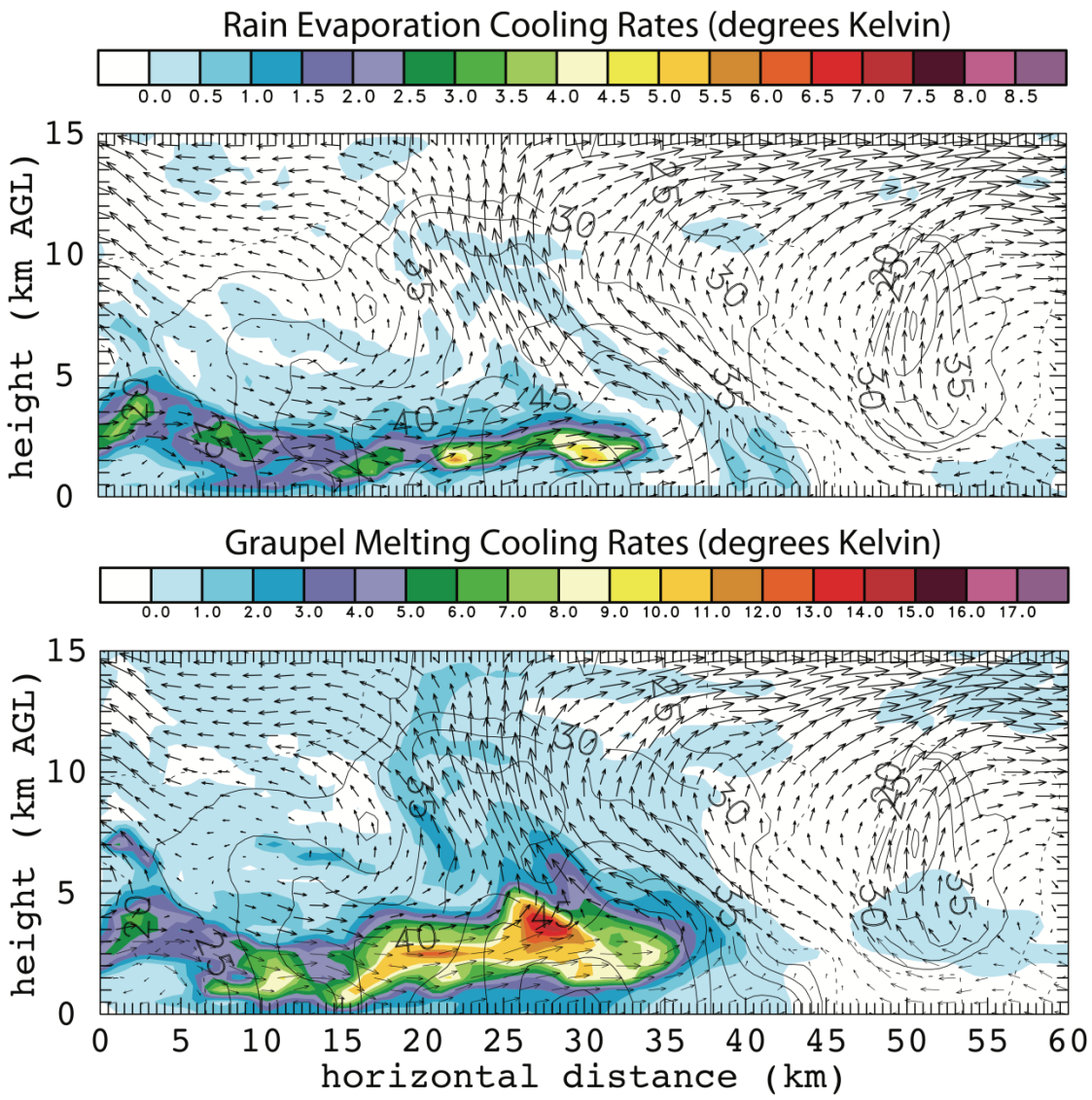

Figure 83. The two panels show color-filled integrated values of a) rain evaporation cooling rates and b) graupel melting cooling rates for the vertical cross section in figure 16 at 0430 UTC. The contours overlaid in both figures are w, the same as in figure 16. These cooling rates are in degrees Kelvin and represent the total cooling along the trajectory up until 0430 UTC.

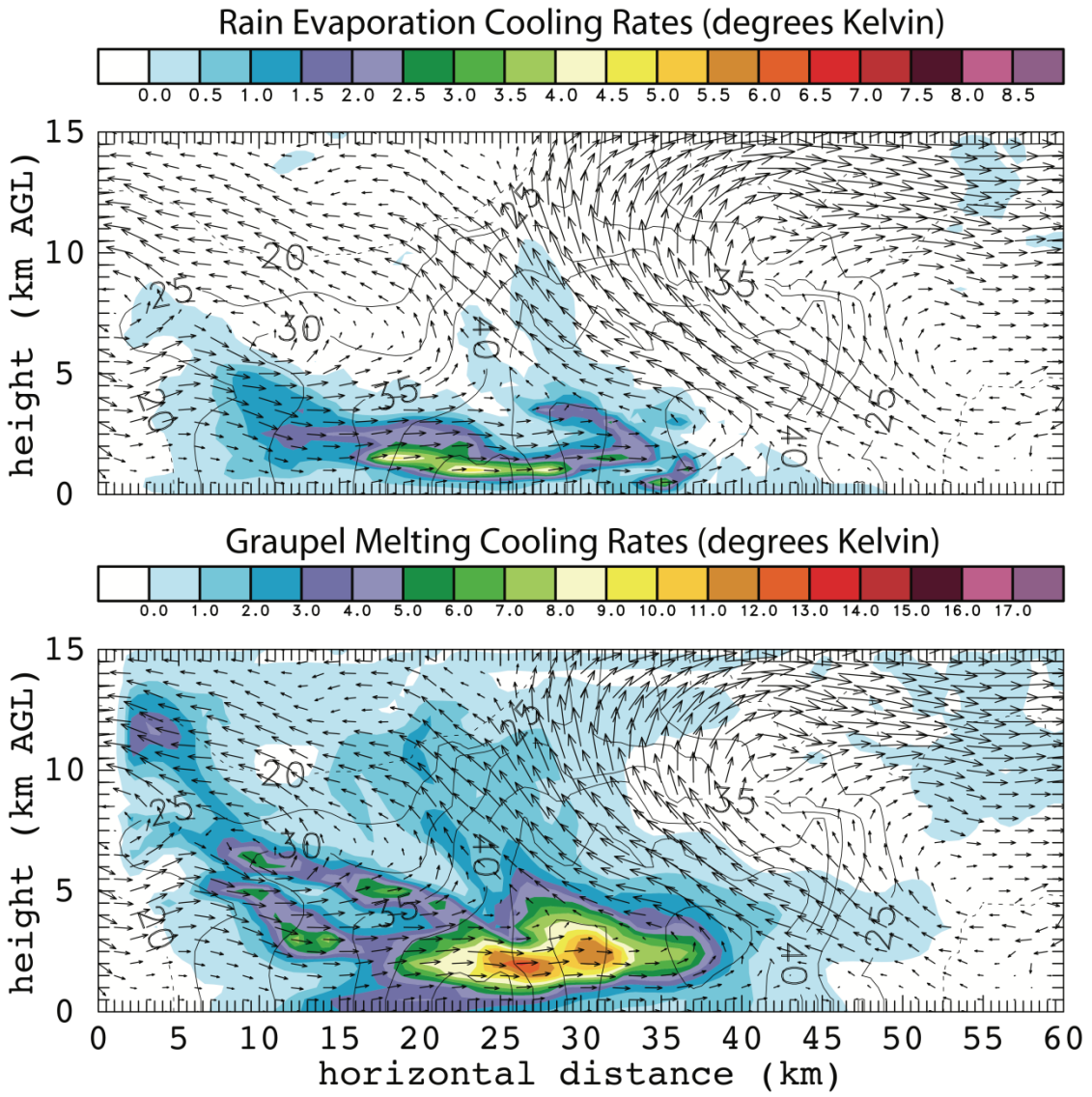

Figure 84. The two panels show color-filled integrated values of a) rain evaporation cooling rates and b) graupel melting cooling rates for the vertical cross section in figure 19 at 0500 UTC. The contours overlaid in both figures are w, the same as in figure 19. These cooling rates are in degrees Kelvin and represent the total cooling along the trajectory up until 0500 UTC.

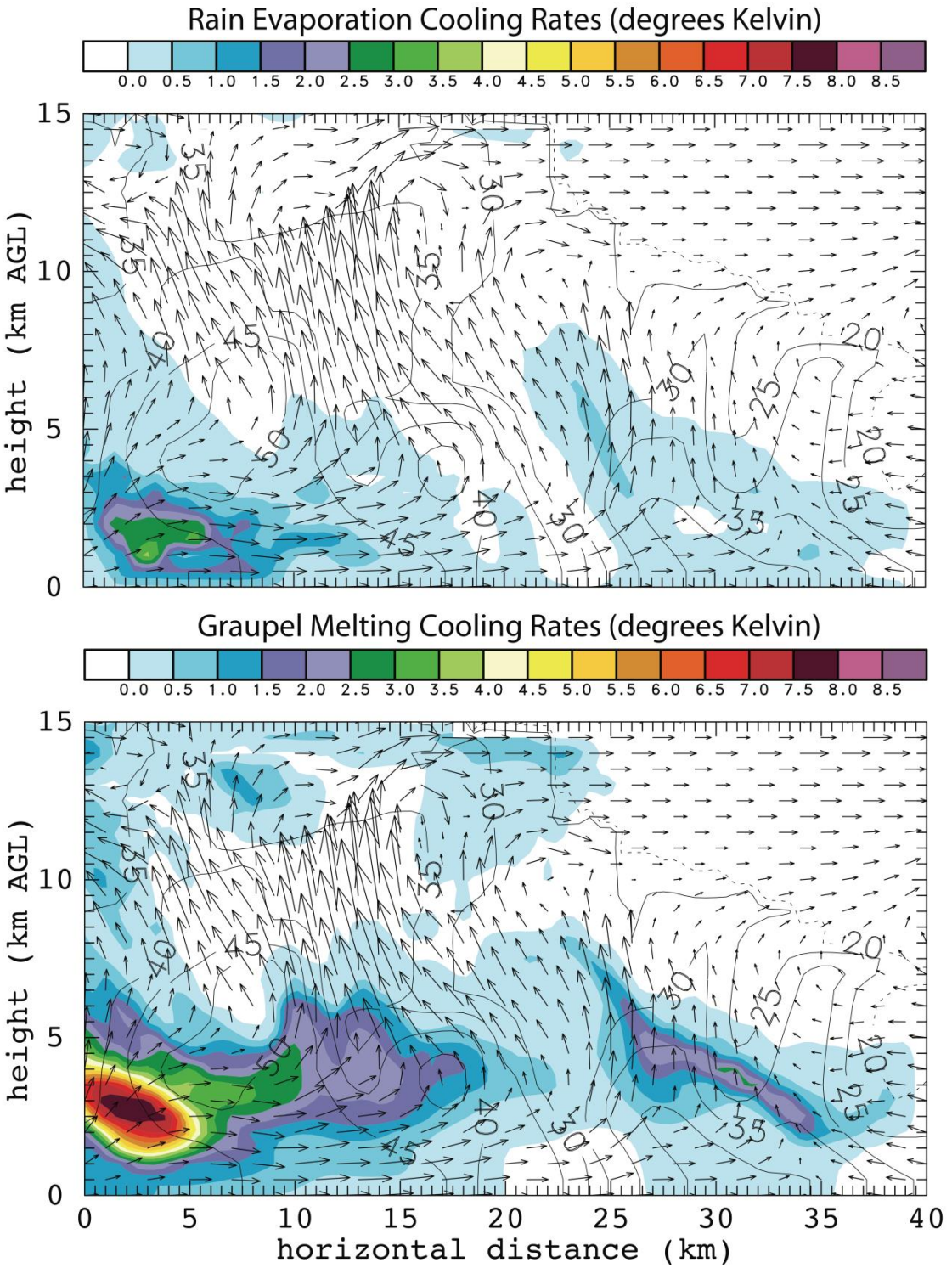

Figure 85. The two panels show color-filled integrated values of a) rain evaporation cooling rates and b) graupel melting cooling rates for the vertical cross section in figure 22 at 0520 UTC. The contours overlaid in both figures are w, the same as in figure 22. These cooling rates are in degrees Kelvin and represent the total cooling along the trajectory up until 0520 UTC.

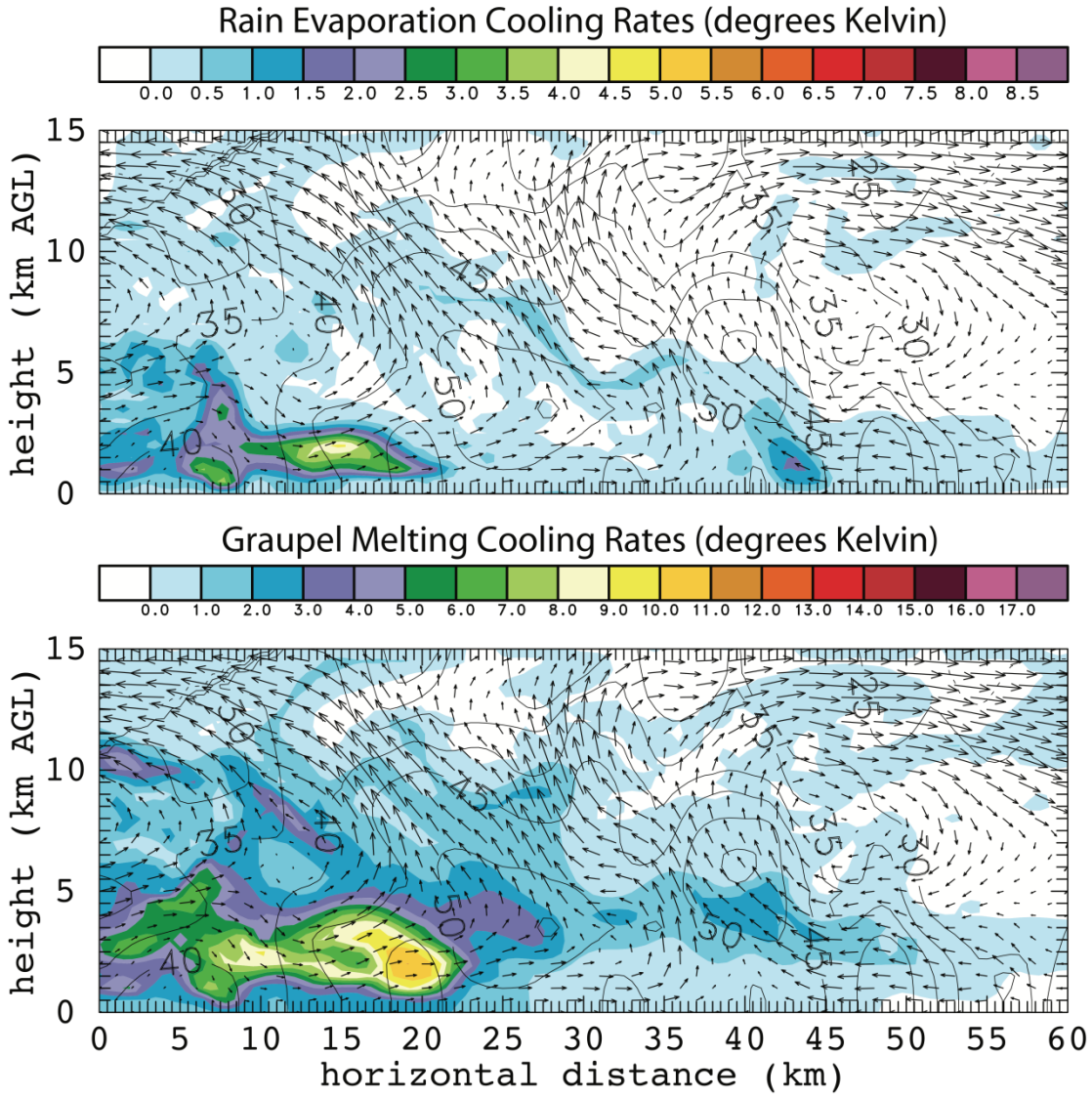

Figure 86. The two panels show color-filled integrated values of a) rain evaporation cooling rates and b) graupel melting cooling rates for the vertical cross section in figure 26 at 0530 UTC. The contours overlaid in both figures are w, the same as in figure 26. These cooling rates are in degrees Kelvin and represent the total cooling along the trajectory up until 0530 UTC.

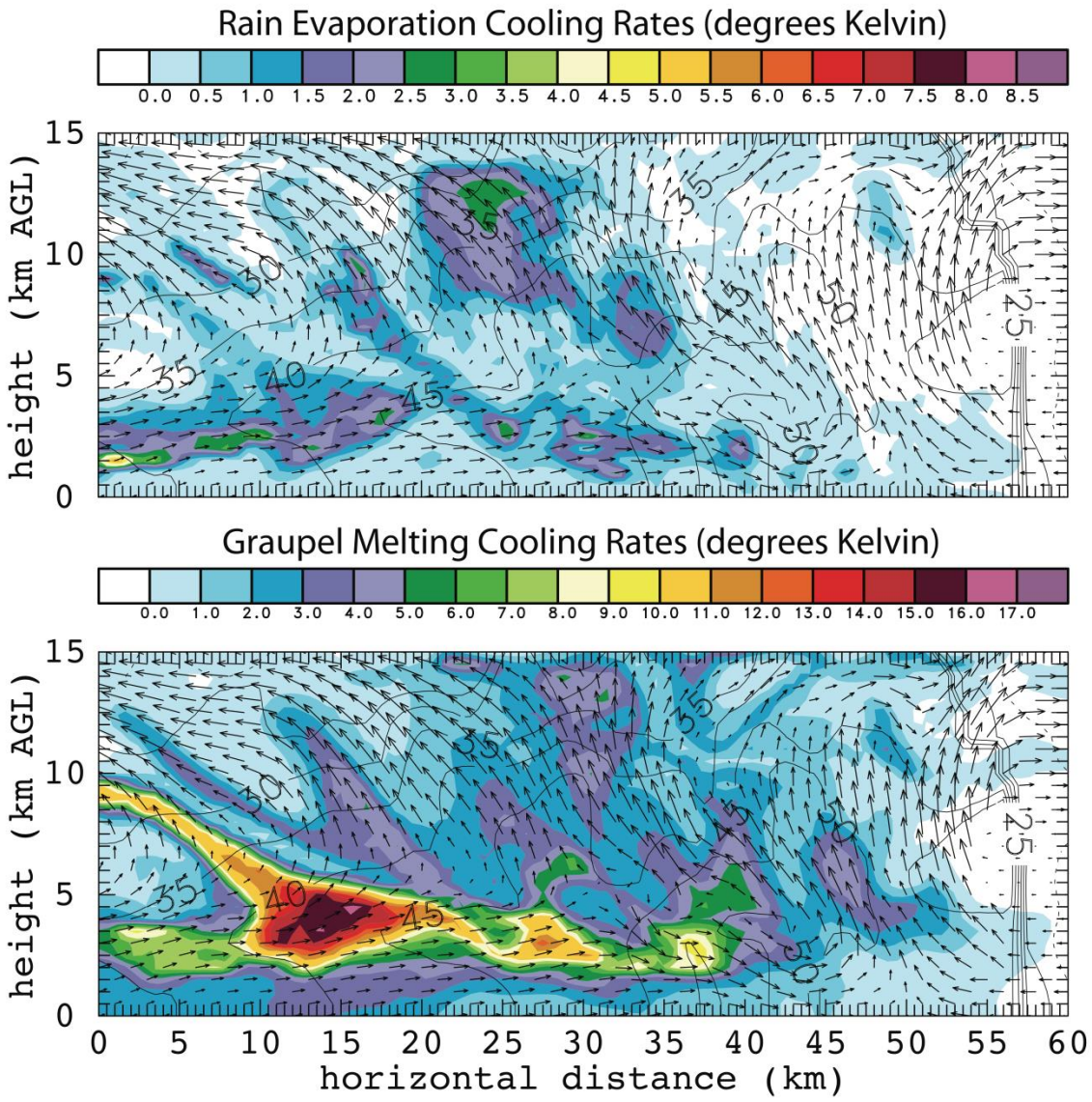

Figure 87. The two panels show color-filled integrated values of a) rain evaporation cooling rates and b) graupel melting cooling rates for the vertical cross section in figure 29 at 0600 UTC. The contours overlaid in both figures are w, the same as in figure 29. These cooling rates are in degrees Kelvin and represent the total cooling along the trajectory up until 0600 UTC.